Synthesis and structure characterization of one-dimensional van der Waals heterostructures

(一次元ファンデルワールスヘテロ構造の合成と構造評価)

Yongjia ZHENG

鄭 永嘉

A dissertation presented in partial fulfillment of

the requirements for the degree of

Doctor of Philosophy

東京大学大学院工学系研究科機械工学専攻

Department of Mechanical Engineering

The University of Tokyo

August 2020

ABSTRACT

Low dimensional materials have been intensively studied recently. More and more researchers have been focusing on acquiring new properties by manipulation materials in nanoscale level. The term “heterostructure” usually refers to the combination of two or more materials along with interesting properties. Such structures play an important role in modern nanotechnologies, which requires advanced material growth techniques.

Compared to traditional heterostructures in which different materials are epitaxially grown, 2D layered materials that weakly bonded by van der Waals (vdW) forces have attracted scientists’ attention as they provide a new perspective to manipulate materials into heterostructures with no lattice matching. However, such vdW heterostructures are realized mostly in planar-based structure, while 1D vdW heterostructures have not yet been deeply studied. In this dissertation, we will start with some of the most investigated 1D and 2D materials, such as metallic graphene, insulating hexagonal boron nitride (h-BN) and semiconducting molybdenum disulfide (MoS_2), followed by a discussion of vdW heterostructures with their combination. This will provide the foundation of the true 1D vdW heterostructures we proposed in this dissertation.

High quality of 1D vdW heterostructures were evaluated and confirmed by different method, such as absorbance, Raman spectrum, SEM, TEM, EELS, ED pattern, etc. Binary structure in SWCNT-BNNT and SWCNT-MoS_2 order were characterized, and ternary structure in SWCNT-BNNT-MoS_2 was further demonstrated. Formation mechanism of 1D vdW heterostructures was deeply discussed with the open-end-chiral growth, the effect of nucleation sites, and three kinds of growth models. The high quality of 1D heterostructure structures allows for further experimental exploration of properties. Some preliminary experiments for new phenomena were also given in terms of thermal, optical, and electronic characteristics. We believe there is a great prospect for these new structures as they extended the concept of vdW heterostructures to 1D materials.

TABLE OF CONTENTS

LIST OF ABBREVIATIONS

0D: zero-dimensional

1D: one-dimensional

2D: two-dimensional

SWCNT: single-walled carbon nanotube

CNT: carbon nanotube

BNNT: boron nitride nanotube

QW: quantum well

QWR: quantum wires

QD: quantum dot

eDOS: electronic density of states

EELS: electron energy loss spectroscopy

FET: field effect transistor

HAADF-STEM: high-angle annular dark-field scanning transmission electron microscopy

PL: photoluminescence

RBM: radial breathing mode

ED: electron diffraction

sccm: standard cubic centimeters per minute

SEM: scanning electron microscopy

TEM: transmission electron microscopy

TMDC: transition metal dichalcogenide

UV-Vis-NIR: ultraviolet-visible-near infrared

CBM: conduction band minimum

VBM: valence band maximum

STATEMENT OF ORIGINAL AUTHORSHIP

The work contained in this thesis has not been previously submitted to meet requirements for an award at this or any other higher education institution. To the best of my knowledge and belief, the thesis contains no material previously published or written by another person except where due reference is made.

Signature: 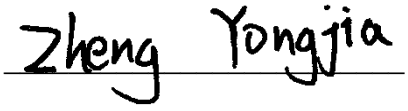

Date: 2020/08/19 .

Chapter 1: Introduction

1.1 Low-dimensional materials

Since mankind begins to be able to manipulate materials at the nanoscale, nanotechnology is no longer just a social topic and is beginning to affect people's live. The advances in nanotechnology have rapidly broadened the scope and application of nanomaterials in chemistry, physics, biology, and engineering. It has been pointed out that nanomaterials in varying nanometer size and dimensions results in different nanostructure with unique properties, which has been a motivation for keeping researchers trying to figure out how materials behave when sample size get close to the atomic scale.

"Low-dimensional materials" is a term used to describe a new class of nanomaterials in reduced dimensionality. Generally, there are three categories considered when it comes to low dimensional materials: the so-called 0D materials including clusters and colloids; the 1D materials such as nanotubes and nanowires in chain-like structure; the 2D materials such as layered structure and thin film. Compared to 3D bulk substances, low-dimensional materials are expected to exhibit unusual properties due to quantum size effect or interfacial effects.

Depending on the dimensionality and size, low-dimensional materials show significantly different density of states in electronic behaviors. In general, when a material is small enough in one or more dimensions, it is possible to cause obvious change in electronic density of state as shown in Fig. 1.1. Consequently, we can have 2D quantum wells, 1D quantum wires, and 0D quantum dots, respectively. In semiconductors materials, the density of states $Z(E)$ in bulk, QW, QWR and QD structures can be expressed as:

$$Z(E)_{3D} = \frac{1}{2\pi^2}\left(\frac{2m^*}{\hbar^2}\right)^{\frac{3}{2}}\sqrt{E}$$

$$Z(E)_{2D} = \frac{m^*}{\pi\hbar^2}\sum_n \sigma(E - E_n)$$

$$Z(E)_{1D} = \frac{1}{\pi\hbar}\sum_{n}\sqrt{\frac{m^*}{2(E-E_n)}}\sigma(E-E_n)$$

$$Z(E)_{0D} = \sum_{n} 2\delta(E-E_n)$$

Here m^* is the effective mass of the electron in a band, $\hbar$ is reduced Planck's constant, E is the energy as the zero of energy is taken at the bottom of the conduction band, E_n is the nth energy level, $\sigma(E-E_n)$ is the Heaviside step function and $\delta(E-E_n)$ is the Dirac delta function. Bulk semiconductor materials are example of 3D system where density of states is relative to $\sqrt{E}$. In 2D QW, electrons are confined in one dimension and therefore possess step-like density of states. Similarly, electrons in 1D QWR are confined in two dimensions and therefore have density of states proportional to $(E-E_n)^{-\frac{1}{2}}$. For a quantum dot as a 0D system, electron motion is confined in three spatial directions, and the expression for density of states follows a Dirac delta function $\sigma(E-E_n)$.

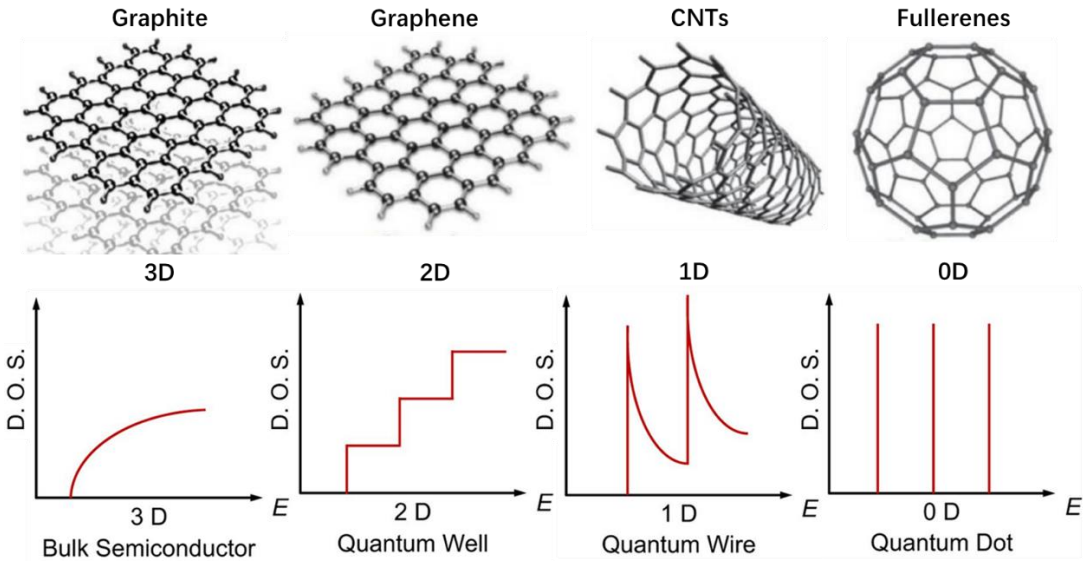

Figure 1.1 Schematic of low-dimensional semiconductor structures and the corresponding electronic density of states. Reprinted from [1, 2].

These strongly confined electrons show a fascinating variety of unusual and exciting effect, which makes low-dimensional nanomaterials a promising platform to develop the next-generation cutting-edge-technologies. In the following chapters, the

representatives in family of low-dimensional nanomaterials focusing on one and two dimensions will be given.

1.2 One-dimensional materials

Development of new types of nanomaterials have been attracting researchers' interests. The booming of low-dimensional materials started in 1985 when the first low-dimensional carbon allotrope, C_{60} fullerene molecule, was discovered [3]. As a quasi-0D material, synthesis of fullerene opened a new field of carbon chemistry and physics. Soon after this, in 1991, the 1D CNTs were discovered by Iijima et al [4], which possess unique structure dependent electronic, mechanical, and optical properties. Since then, the observation of CNTs quickly revolutionized the view of nanoscience and nanotechnology during the past several decades. Meanwhile, 1D materials were then widely researched as they exhibited novel electronic and transport properties with the effect of reduced dimensionality and quantum confinement. This chapter will give a brief introduction for some of the 1D materials.

1.2.1 SWCNT

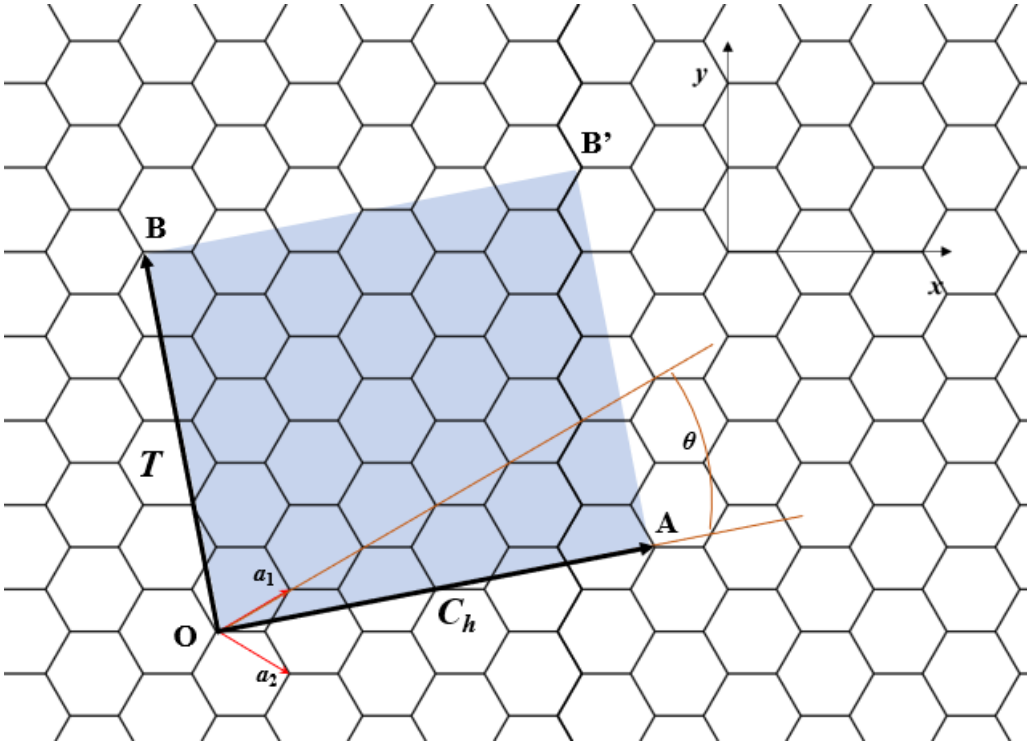

Figure 1.2 Unrolled hexagonal lattice of a SWNCT. The chiral vector C_h and translational vector T are presented for the case of C_h = $4a_1$ + $2a_2$ SWCNT. Rectangle OBB'A is regarded as a unit cell in the atomic structure of an SWCNT. The angle between a_1 and C_h gives the chiral angle ($0 \leq \theta \leq 30°$).

A SWCNT can be considered as a rolled-up sheet of single-layer carbon atoms, so-called graphene, which has 2D hexagonal lattice structure with sp^2 carbon network, as shown in Fig. 1.2. Depending on the rolling-up direction of the graphene layer, SWCNTs form different chiral structures along with various electrical properties.

Fig. 1.2 also shows how a chiral SWCNT is determined. We choose 2 points, O as a starting point and A as an ending point, in an unfolding graphene layer. After O and A connecting to each other, the graphene will change into a tube-like SWCNT as expected. The chiral structure of SWCNT varies as the relative position between O and A changes. To begin with, two basic vectors are given below as

$$\boldsymbol{a}_1 = \left(\frac{\sqrt{3}}{2}a, \frac{a}{2}\right), \boldsymbol{a}_2 = \left(\frac{\sqrt{3}}{2}a, -\frac{a}{2}\right) \tag{1.1}$$

They are defined as the basic vectors in such honeycomb 2D surface. Then, we consider O as the ordinate origin and denote vector $\overrightarrow{OA}$ as $\boldsymbol{C}_h$. With fixed basic vector $\boldsymbol{a}_1$ and $\boldsymbol{a}_2$, $\boldsymbol{C}_h$ is determined by just two integers n and m ($n \geq m \geq 0$ due to the hexagonal symmetry), which is described as

$$\boldsymbol{C}_h = n\boldsymbol{a}_1 + m\boldsymbol{a}_2 \equiv (n, m) \tag{1.2}$$

In Eq. (1.2), we learn that the pair of integers n and m denotes the number of unit vector in $\boldsymbol{C}_h$. In another word, the chiral structure of SWCNT can also be completely specified by the corresponding indices (n, m).

The distance between each neighbouring carbon atoms in SWCNTs is known as $a_{c-c} = 1.44\,\text{Å}$, then the lattice constant of SWCNTs can be further calculated as $a \equiv |a_1| = |a_2| = \sqrt{3}a_{c-c} = 2.49\,\text{Å}$. Obviously, vector $\boldsymbol{C}_h$ can be interpreted as circumference of SWCNT, so the nanotube diameter can be written in terms of n and m as

$$d = \frac{|\boldsymbol{C}_h|}{\pi} = \frac{\sqrt{\boldsymbol{C}_h \cdot \boldsymbol{C}_h}}{\pi} = \frac{a\sqrt{n^2 + m^2 + nm}}{\pi} \tag{1.3}$$

The chiral angel θ defined between $\boldsymbol{C}_h$ and $\boldsymbol{a}_1$, of which value should be $0 \leq \theta \leq 30°$ due to hexagonal symmetry as well, is given by

$$cos\theta = \frac{\boldsymbol{C}_h \cdot \boldsymbol{a}_1}{|\boldsymbol{C}_h||\boldsymbol{a}_1|} = \frac{(2n + m)}{2\sqrt{n^2 + m^2 + nm}} \tag{1.4}$$

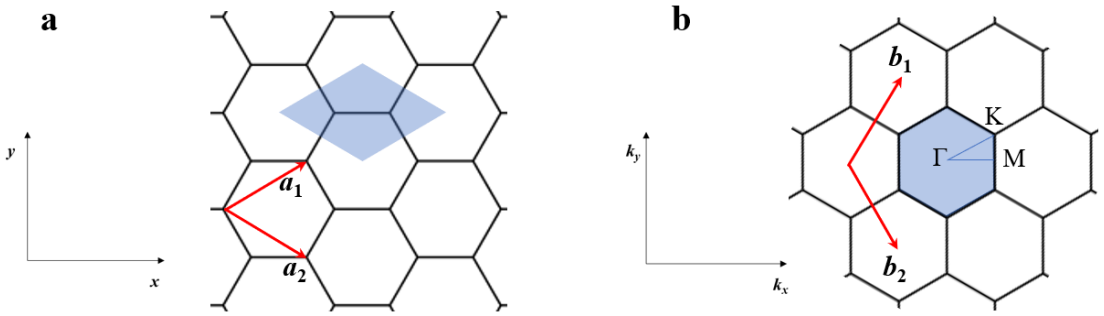

Figure. 1.3 (a) Unit cell and (b) Brillouin zone of 2D graphite represented as the coloured rhombus and hexagon, respectively. a_1 and a_2 are unit vectors, and b_1 and b_2 are reciprocal lattice vectors. Three high-symmetric points were denoted as Γ, K and M.

Rectangle OBB'A is regarded as a unit cell in the atomic structure of an SWCNT. Here, we labelled $\overrightarrow{OB}$ as translational vector $\boldsymbol{T}$, which is defined as the shortest distance along the SWCNT axis in repetition. $\boldsymbol{T}$ is written as

$$\boldsymbol{T} = t_1\boldsymbol{a_1} + t_2\boldsymbol{a_2} \equiv (t_1, t_2) \tag{1.5}$$

and it should follow the relationship $\boldsymbol{C}_h \cdot \boldsymbol{T} = 0$. Then t_1 and t_1 can be described as

$$t_1 = \frac{2m+n}{d_R}, t_2 = \frac{2n+m}{d_R} \tag{1.6}$$

where d_R is the greatest common divisor of $(2m+n)$ and $(2n+m)$. The number of the hexagon then can be given by

$$N = \frac{|\boldsymbol{C}_h \times \boldsymbol{T}|}{|\boldsymbol{a}_1 \times \boldsymbol{a}_2|} = \frac{2(n^2+nm+m^2)}{d_R} \tag{1.7}$$

As a result, the number of carbon atoms in each unit cell is 2N.

On the other hand, the reciprocal lattice of SWCNT in reciprocal space should also be considered, which plays a fundamental role in analysing periodic structures. With given basic vectors $\boldsymbol{a}_1$ and $\boldsymbol{a}_2$, the corresponding reciprocal vectors $\boldsymbol{b}_1$ and $\boldsymbol{b}_2$ are expressed as

$$\boldsymbol{b}_1 = \left(\frac{2\pi}{\sqrt{3}a}, \frac{2\pi}{\mathrm{a}}\right), \boldsymbol{b}_2 = \left(\frac{2\pi}{\sqrt{3}a}, -\frac{2\pi}{\mathrm{a}}\right) \tag{1.8}$$

shown in Fig. 1.3. The coloured area is the first Brillouin zone, in which three high symmetry points, Γ, K and M, exits as centre, corner, and centre of the edge. $\boldsymbol{C}_h$ and

$\boldsymbol{T}$ is regarded as a pair of orthogonal unit vectors to describe a unit cell. Similarly, we define their corresponding reciprocal vector as $\boldsymbol{K}_c$ and $\boldsymbol{K}_a$ in circumferential and axial direction, respectively. With the following relationship,

$$\boldsymbol{C}_h \cdot \boldsymbol{K}_c = 2\pi \,, \boldsymbol{T} \cdot \boldsymbol{K}_c = 0 \,, \boldsymbol{C}_h \cdot \boldsymbol{K}_a = 0 \,, \boldsymbol{T} \cdot \boldsymbol{K}_a = 2\pi \tag{1.9}$$

$\boldsymbol{K}_c$ and $\boldsymbol{K}_a$ can be obtained as,

$$\boldsymbol{K}_c = \frac{1}{N}(t_2\boldsymbol{b}_1 + t_1\boldsymbol{b}_2) \,, \boldsymbol{K}_a = \frac{1}{N}(m\boldsymbol{b}_1 - n\boldsymbol{b}_2) \tag{1.10}$$

We denote the energy dispersion relation of unfolding graphene as $E_{2D}^{\pm}(\boldsymbol{k})$, which can be calculated by the tight-binding approximation of the two neighbouring carbon atoms with their $2p_z$ orbital. The result is

$$E_{2D}^{\pm}(\boldsymbol{k}) = \frac{\varepsilon_{2p} \pm t\omega(\boldsymbol{k})}{1 \pm s\omega(\boldsymbol{k})}$$

$$\omega(\boldsymbol{k}) = \sqrt{1 + 4cos\frac{\sqrt{3}\boldsymbol{k}_x a}{2} cos\frac{\boldsymbol{k}_y a}{2} + 4cos^2\frac{\boldsymbol{k}_y a}{2}}$$

In the case of 1D SWCNT, the rolling action in nanotube creates quantum confinement in circumferential direction. We apply periodic boundary conditions on the circumference, then the energy dispersion of SWCNT can be given by

$$E_\mu(k) = E_{2D}^{\pm}\left(k\frac{\boldsymbol{K}_2}{|\boldsymbol{K}_2|} + \mu\boldsymbol{K}_1\right), \left(\mu = 0, 1, \dots, N-1, and -\frac{\pi}{|\boldsymbol{T}|} < k < \frac{\pi}{|\boldsymbol{T}|}\right) \tag{1.11}$$

This expression means that the possible wave vectors can be obtained from the energy dispersion of graphene, but they are confined within limited lines due to the periodic boundary conditions. These parallel lines represent the cutting lines, labelled by the cutting line index μ, which values from 0 to N-1. In Eq. (1.11), wave vectors $\mu\boldsymbol{K}_1$ are the N quantized states in the $\boldsymbol{K}_1$ direction, while $|\boldsymbol{K}_2|$ is the length of line segment along the direction $\boldsymbol{K}_2$, as shown in Fig. 1.4.

When any of these cutting lines pass through K point, SWCNT is metallic. Mathematically, the corresponding indices (n, m) should satisfied $mod(n-m, 3) = 0$, while, on the other hand, SWCNT is semiconducting if $mod(n-m, 3) \neq 0$. This is also one of the most important characteristics that electronical properties of SWCNT is determined by its chirality. For example, (10, 1) and (8, 3) SWCNTs have almost the same diameter, but different electronic properties: the former is a metal, but the

latter is a semiconductor. Fig. 1.5 is a chiral map that summarize the chirality of SWCNT with related electronic property. Among all these indices (n, m), SWCNTs can be classified into zigzag ($m = 0\ or\ \theta = 0°$), armchair ($n = m\ or\ \theta = 30°$), and chiral type ($\theta = 0°$), respectively.

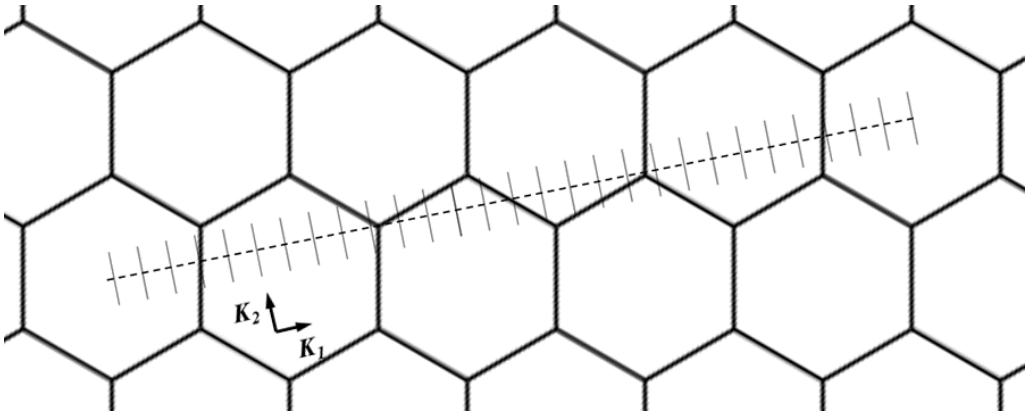

Figure 1.4 Brillouin zone of a SWCNT represented by the line segment for the case of (*n*, *m*) = (4,2) SWCNT.

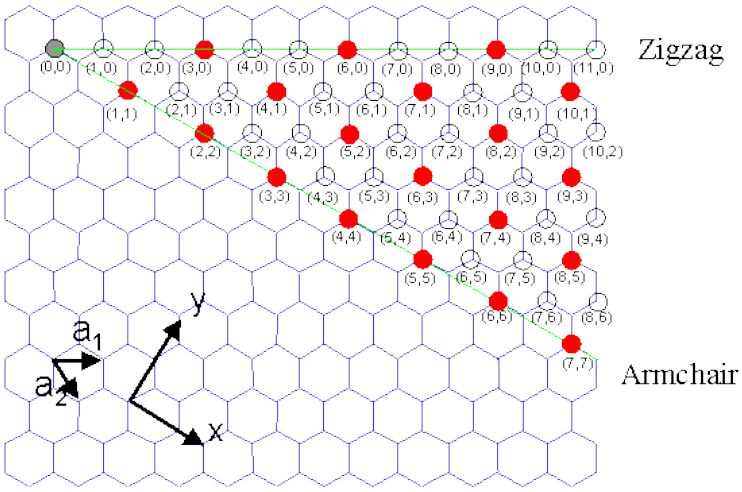

Figure 1.5 Chiral map of SWCNT (*n*, *m*) in which red solid points represent metallic nanotube and black open circles represent semiconductor nanotubes, respectively. Reproduced from http://www.photon.t.u-tokyo.ac.jp/.

Quantized wave vectors described by Eq. (1.11) cause an inconsecutive function of energy in their eDOS, which is one of the characteristic features for 1D materials. The sharp peaks are called “Van Hove singularities”. The energy separation between ith valence band and conduction band is labelled as $E_{ii}^{S\ or\ M}$. S for semiconducting and

M for metallic. An eDOS of (4, 2) SWCNT shown in Fig. 1.6 is obtained by tight-binding approximation with parameters γ_0 =2.9 eV, s =0, and a_{c-c} =0.144 nm. The theoretical bandgap is about E_{11}^{S} =2 eV.

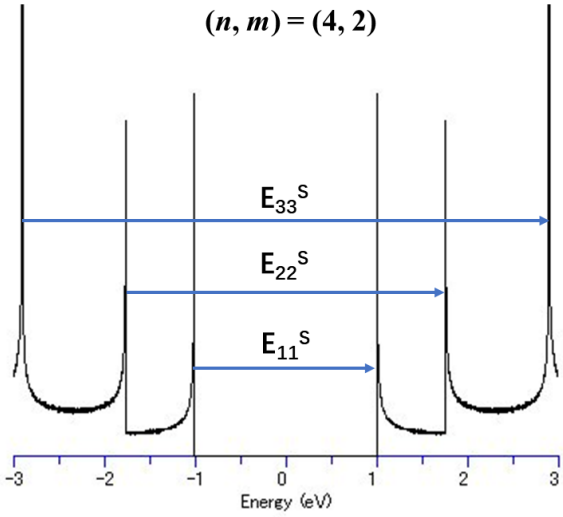

Figure 1.6 eDOS of (4, 2) SWCNT calculated by tight-binding method with γ_0 =2.9 eV, s =0, and a_{c-c} =0.144 nm.

1.2.2 BNNT

BN-based materials in low dimension are one of the most promising inorganic nano systems studied up to now. As unnatural chemical compounds, they should be produced synthetically. BN-based materials exit in different crystalline forms that have similar structure to some of the carbon materials. For example, h-BN has layered structure and is isostructural to graphite. Moreover, BNNTs, which will be discussed hereafter in detail, are analogous to CNTs as 1D materials.

The similarities between carbon and BN-based materials are usually of great benefit to theoretical investigations of the structure of BNNTs. Four years after the discovery of CNTs, BNNTs are subsequently synthesized in 1995 by Zett's group at University of California, Berkeley [5]. Ideal BNNTs are regarded as replacing all the carbon atoms of CNTs alternately into boron and nitrogen atoms. They both have hexagonal structure, and the spacing between tubes is close to each other. On the other hand, BNNTs can also be considered as rolling up h-BN sheets into nanosized cylinders. In fact, there is still a debate whether BNNTs are curled up from a planar hexagonal network [6]. Based on the theoretical calculation result of zigzag BN tube with a B/N ratio of 1, boron and nitrogen atoms are not on the same cylindrical surface. Instead, they form coaxial cylinders with different diameter. Cylinders of boron atoms, specifically, has smaller diameter compared to ones of nitrogen atoms. However, this calculation result has not yet been experimentally demonstrated due to limitation of experiment conditions.

Even though CNTs and BNNTs owns similarities in structure, they are widely different in electronic behavior. Unlike CNTs, BNNTs present partially ionic B–N bonds. Theoretical studies suggest that they possess a band-gap larger than 5.5 eV, and thus show insulating or semiconducting behavior in electrical conductance measurements no matter what diameter or chirality of nanotubes are [7]. This property shows great prospect and high application value in both nanoelectronics and optoelectronics, such as blue-light emitters and excitonic lasers.

Some research revealed that BNNTs have high thermal conductivity as CNTs, some of which can reach to 6000 W/mK [8-10]. Chang et al. found that BNNTs of diameter 30 to 40 nm with more than 99.5% ^{11}B can have a thermal isotope effect resulting in a better thermal conductivity than CNTs [11]. So far, the observations and

experiments were not able to support such theory as the real thermal conductivity from experimental result, 350 W/mK, is far below the ideal theoretical calculations.

BNNTs also exhibit higher thermal stability compared to CNTs. For example, some BNNTs with perfect nanocrystalline structures still remain stable at elevated temperature up to 900°C in the air [12], while CNTs start to be oxidized at 400°C. Golberg et al. conducted a thermogravimetric analysis on BNNTs and CNTs. The result reveals a much stronger resistance to oxidation of BNNTs when temperature is over 600°C [13].

To sum up, BNNTs not only have excellent thermal conductivity and unique electronic behavior, but also owns better chemical stability compared to these of CNTs. In consequence, BNNTs can be applied as insulating layer or protective shields for other nanomaterials.

Laser ablation is one way to prepare few-walled BNNTs. With the help of Ni and Co powder as metal catalysts, the excimer laser can be used to ablate a BN target to form BNNTs of only 1-3 walls with flat or polyhedral caps at the tube end [14, 15]. BNNTs can be synthesized by using Low-energy electron-cyclotron resonance plasma and deposited on tungsten substrate [16]. In addition, CO_2 laser ablation was also used to prepared BNNTs in gram quantities without the benefit of metal catalysts [17]. Furthermore, Arenal et al. improved this synthesis by observing the boron particles at the tube ends and proposing a root-growth model, increasing the yield of single-walled BNNTs up to 80% [18]. However, Laude et al. brought up with a controversial result that no single-walled BNNTs were attained by similar experiments [19]. It should be noted that this synthesis was the only route for large-scale production of single-walled BNNTs. In despite of the difficulty in preparation of single-walled BNNTs, more attention was paid to the multiwalled BNNTs. Wang et al. received a high yield of multiwalled BNNTs by using laser ablation on oxidized silicon substrate coated with Fe films as catalysts [20]. In general, researchers have demonstrated the feasibility of laser ablation of large-scale BNNTs preparation, whereas the problems of these complex apparatus were due to the high cost.

Later in 1999, Chen et al. proposed a facile synthesis called ball milling and annealing method, which can produce BN nanomaterials in large scale [21]. They used h-BN powder as the starting materials for ball milling and then annealed under N_2. More than one product was formed, consisting of both cylindrical and bamboo-like

BNNTs. Subsequently, if boron powder was used instead of h-BN powder, the yields of BNNTs would increase to 85% [22-24]. In a similar way, ^{10}BNNTs could be prepared by substituting with isotopic ^{10}B powder as the boron source [25]. As for the annealing process, an ammonia atmosphere could result in pure cylindrical BNNTs while other conditions kept unchanged [26]. Also, B_2O_3 powder can also be used as the boron source to synthesize bamboo-like BNNTs in large scale [27]. Overall, this ball milling method was considered as an effective way to prepare high-yield BNNTs from solid phase.

1.2.3 MoS_2 nanotube

Researches on properties of graphene have given scientists lots of hints to study about TMDCs materials which have the chemical formula MX_2. M represents a transition metal atom and X a chalcogen. MoS_2 is one of TMDCs that consists of transition metal Mo and chalcogen S with a ratio of 1:2, By analogy to different forms of carbon, Tenne et al. suggested that layered TMDCs could form similar structures like fullerene and nanotube [28-30]. MoS_2 nanotube was then indeed synthesized and characterized by Tenne' group [31] (Fig. 1.7), of which procedure involves heating MoO_3 and H_2S as the starting source in the stream of argon.

Compared with CNTs, MoS_2 nanotubes can be classified as inorganic nanotubes. Their tube size is usually very large in multi-walled structure as the diameters can barely be controlled below 20 nm. Some of their properties have already been experimentally confirmed, such as the unusual magnetic state in lithium-doped $MoS_{2-x}I_y$ nanotubes [32], and the storage material for reversible lithium batteries [33]. Till now, the small quantities of preparation as well as dimensions control become crucial problems when it comes to physical experiments and further potential applications.

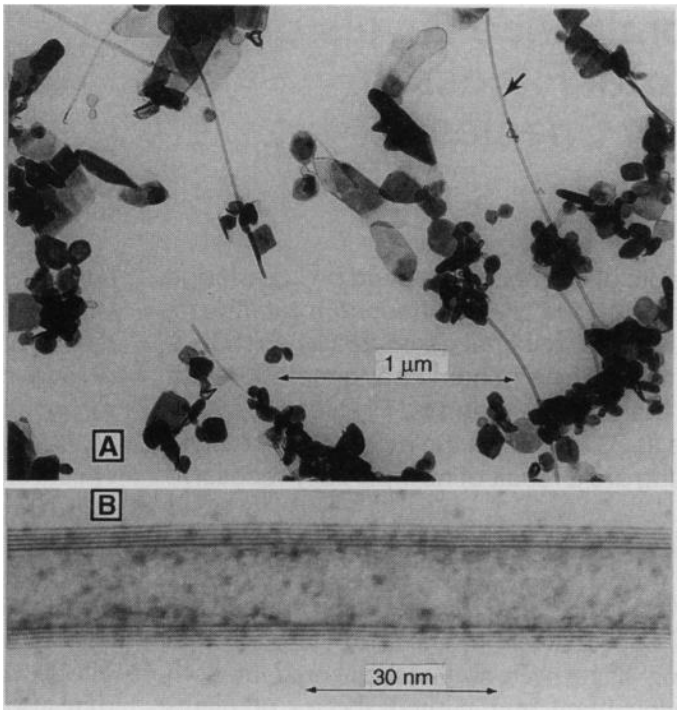

Figure 1.7 (A) Assortment of MoS_2 nanotubes and (B) the high-magnification image. Reprinted from [31], Copyright (1995), with permission from AAAS.

1.3 Two-dimensional materials

In 2004, the 2D carbon allotrope, graphene, were produced and identified by Geim and Novoselov et al. and rapidly became a rising star in the field of 2D nanomaterials [34]. After the discovery of graphene, more and more graphene-like materials have been found and fabricated. These kinds of 2D materials obtained as monolayer form were found to hold even more promise with the variety of properties, such as $NbSe_2$ as metals, semiconductors as MoS_2, and insulators as h-BN. Researchers realized that the properties of such 2D materials with reduced dimension are different from those of their 3D counterparts.

1.3.1 Graphene

In section 1.2.1, we used graphene as a basic structure to discuss about SWCNTs fundamental, while this part gives a brief introduction to the graphene itself. Graphene is not only considered as an allotrope to fullerenes and CNTs, but also served as an important building block toward other materials research. It composes with a sheets of carbon atoms, of which s, p_x, and p_y atomic orbitals on each hybridize to form strong covalent sp^2 bonds to each other with the bond angles of 120°. The remaining p_z orbitals of every three neighbouring carbons atom form π and π^* orbitals, called valence band and conduction band, respectively.

Graphene can be obtained from earth-abundant graphite by exfoliation method. Such layered graphene exhibits extraordinary electrical, optical, mechanical and thermal properties due to its long-range π-conjugation [35]. Here are some examples, Monolayer graphene owns high carrier mobility of about 200,000 $cm^2V^{-1}s^{-1}$ [36] and high optical transparency toward visible light over 98% [37]. What's more, it has excellent mechanical strength with Young's modulus of 1.1 TPa [38] and thermal conductivity of about 5000 WmK^{-1} [39].

Graphene can be easily processed into different forms, such as multi-layer nanosheets [40], nanoribbons [41], and foam [42]. Therefore, it widely serves as basic materials for varied application, including energy storage devices [43], electronic skin [44], field effect transistors [45], and gas sensors [46] etc.

Even though applications have been developed in different areas, the task for a wider use of graphene is hindered by difficulties in high-quality preparation. So far, main strategies for preparation of graphene include mechanical exfoliation [47],

solution-phase exfoliation[48], bottom-up methods [49], and substrate-based growth by CVD [50].

1.3.2 Hexagonal boron nitride

h-BN is known as “white graphene” as it has similar structure to graphene with alternative B atoms and N atoms connected by sp^2 covalent bond (Fig 1.8). As discussed in the previous section, h-BN is one crystalline form of the exited BN-based materials. It is usually used as a sub-layer material for other 2D materials served as an insulator. Moreover, h-BN is also known to be thermally and chemically stable, along with high thermal conductivity and mechanical robustness. Additionally, there is no absorption in visible parts of the spectrum for h-BN which yet has absorption in ultraviolet range.

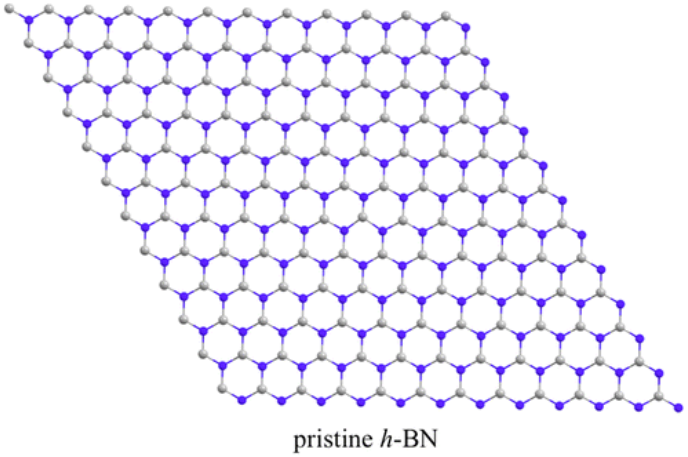

Figure 1.8 Surface models for pristine h-BN in monolayer. Blue and grey spheres represent for boron-atoms and nitrogen-atoms. Reprinted from [51], Copyright (2016), with permission from ACS.

The lattice structure of 2D h-BN is almost the same as graphene in hexagonal pattern with only a lattice mismatch of about 1.8%, whereas the electrical conductivity is totally different from each other. h-BN owns insulating properties while graphene is semiconducting.

Various processing strategies have been applied to synthesis 2D h-BN, including mechanical exfoliation, liquid exfoliation, chemical vapor deposition, and epitaxy. Mechanical exfoliation is one of the feasible ways to obtain crystalline h-BN [52], but the side and position of the as-prepared h-BN layers is usually not controllable with small size in low yield. Liquid exfoliation is a more efficient method to produce h-BN in large scale [53]. Disadvantages such as contamination on film surface, ungovernable

number of layers and limited flake size, however, make this exfoliation method more challenging in application. On the other hand, CVD and the vaper phase epitaxy process are also achievable strategies for growth of 2D-hBN nanosheets [54, 55]. Compared with exfoliation, the number and the scale of layers are relatively controllable, but CVD process requires high temperature that places greater demands on the substrate and apparatus.

2D h-BN has ultra-flat surface without dangling bonds, which can be used as a dielectric substrate for other 2D materials such as graphene and TMDC materials in electronic and optical device [56, 57]. In addition, 2D h-BN can also be a good candidate for passivation and protection for other 2D materials, which acts as protective layers to prevent atoms exposed to the surface from degradation of intrinsic characteristics [58-60].

1.3.3 2D Molybdenum disulfide

MoS_2 as one of the TMDCs belongs to indirect band gap semiconductors in their bulk forms. Thinned to a monolayer, it is reduced to 2D form and become direct band gap materials.

As illustrated in Fig. 1.9a, crystal structure of MoS_2 takes the form of hexagonal plane in a top-down view. In each layer, a plane of Mo atoms sandwiched in two plane of S atoms, in which each Mo atom is bonded to six S atoms while each S atom is bonded to 3 Mo atoms. These triple planes of atoms bond with each other with strong covalent bonds between Mo and S atoms, resulting in no dangling bonds left for S atoms. The absence of dangling bonds indicates that MoS_2 is a layered material with weak van der Waals forces holding layers together, which means a 2D sheets of MoS_2 can be mechanically separated from a bulk material.

Bulk MoS_2 can be found in the natural world as mineral, named 'molybdenite', that can be dated back to over 2.9 billion years ago [61]. In its bulk form, MoS_2 appears shiny grey colour as shown in Fig. 1.9b. It can be used as a lubricant due to the weak interaction of van der Waals forces between layers that allows sheets to easily slide over itself. However, the application of MoS_2 had been confined to lubricant and industrial catalyst for quite some time.

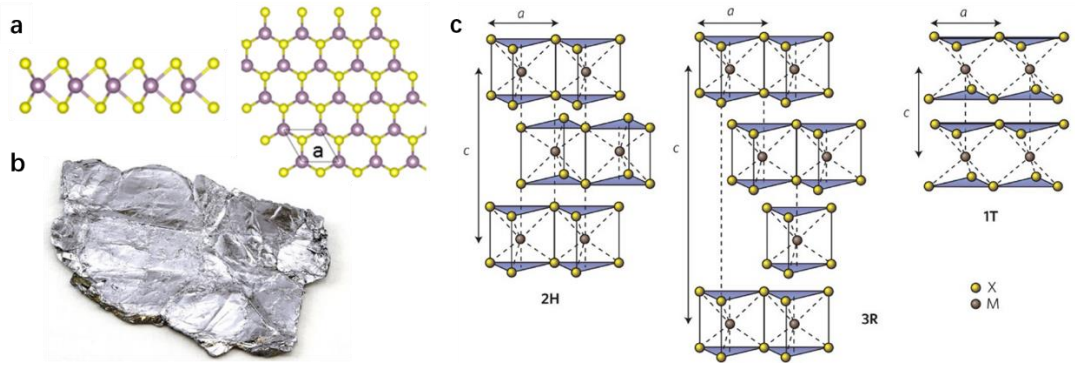

Figure 1.9 (a) Structure of a hexagonal TMD monolayer. Reproduced from [62]. (b) Photograph of bulk MoS_2 crystal, which is approximately 1 cm long. (c) Schematics of the structural polytypes: 2*H*, 3*R*, and 1*T*. Reprinted from [63], Copyright (2012), with permission from Springer Nature.

Fig. 1.9c shows three kinds phases of MoS_2 in different symmetry: 2*H* (hexagonal symmetry with 2 layers per unit-cell), 3*R* (rhombohedral symmetry with 3

layers per unit-cell), and 1*T* (tetragonal symmetry with 1 layer per unit-cell) among which 2*H* is the most desired form for MoS_2 in electronic applications.

The unique physical, optical, and electrical properties of MoS_2 have attracted wide range of attention from researchers. Originally, the bandgap of bulk MoS_2 is 1-1.3 eV. As the number of layers decreases to one as a 2D materials, its properties change radically with an increased bandgap of 1.9 eV. At the same time, the indirect bandgap of bulk MoS_2 will also change into direct one as a 2D monolayer. This 2D MoS_2 has a quantum yield of about 0.4% [64] and a high carrier mobilities approximately 350 $cm^2V^{-1}s^{-1}$ [65]. It can also be fabricated into a field-effect transistor with an ON/OFF ratio of about 10^8 [66], making it a good candidate for high-efficiency switching and logic circuits.

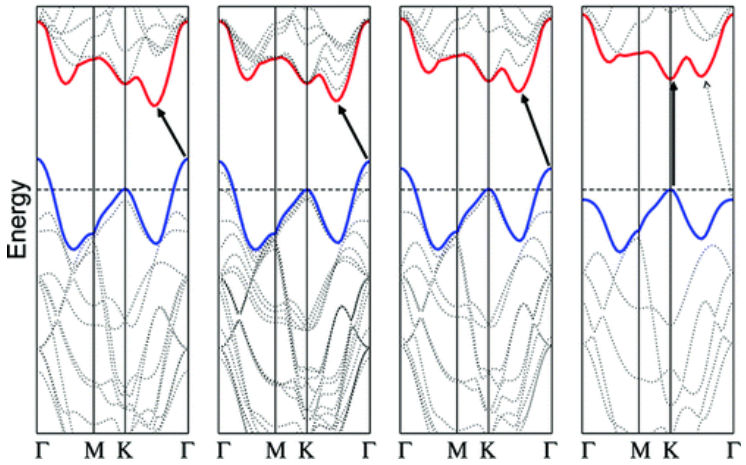

Figure 1.10 Band structure of MoS_2 in different forms, in which from left to right is bulk MoS_2, quadrilayer MoS_2, bilayer MoS_2, and monolayer MoS_2. The solid arrows indicate the lowest energy transitions. Reproduced from [67], Copyright (2010), with permission from ACS.

Fig. 1.10 is the simplified band structure of MoS_2 showing the crossover from indirect to direct bandgap transition. Conduction bands and valence bands at K point are contributed mostly from the *d* orbital of Mo atom. In near Γ point, a lowest conduction band is on the left while the highest split valence bands are at Γ point, which are contributed from both the *d* orbital of Mo atom and p_z orbital of S atom. Since the Mo atoms are sandwiched in the middle of each MoS_2 layer, their electronic states are not influenced by the interlayer coupling effect. The outside S atoms, however, are significantly influenced by the other S atoms from the adjacent layers.

As the number of layers decreases, the interlayer coupling effect between S atoms becomes weaken, resulting in a larger indirect bandgap than the direct bandgap at K point. In another word, 2D MoS_2 in unit cell thickness becomes a direct bandgap semiconductor. This thickness-dependent bandgap structure makes ultrathin MoS_2 sensitive to incident light with different wavelengths in optoelectronic.

1.4 Van der Walls heterostructures

Nanotechnology focusing on designing materials in nanoscale is an appealing idea but not easy to realize. Researchers are making their great efforts to come up with a general solution for materials integration. Still, we need to seek a mixing strategy with selected ingredients and, thus, obtain one ultimate materials with better properties and predetermined functionalities.

One of the major problems to realizing heterostructure at early stage of materials science is the lattice matching at heterojunction interfaces. However, the lattice-matching condition becomes relaxed when the epitaxial growth proceeds with vdW interactions [68]. The relatively weak vdW forces are sufficient to keep the layered materials together even with a large lattice mismatch between the grown and the substrate materials [69].

The constant emergence of varied vdW bonded materials provides new insights into materials design, thereby opening new avenues for the development of nanomaterials. Consequently, combinations of distinct materials have been assembled with different functionalities [70-72].

1.4.1 2D vdW heterostructures

2D materials offer a platform that gives birth to heterostructures with a variety of properties. Held together by vdW forces, a growing number of 2D heterostructures with combinations of 2D materials have been demonstrated. By stacking different 2D materials on top of each other, the synergetic effects between each component become considerable, such as surface reconstruction, charge redistribution and proximity effects between neighbouring layers.

Few years after the graphene boom, researchers have started to pay more attention to some other 2D atomic materials, such as monolayers and few-layer crystals of h-BN, MoS_2, other dichalcogenides and layered oxides. Here are some examples for their synergetic effects. h-BN substrate is considered as one of the stacked materials for 2D devices due to its smooth surface of dangling bonds and charge traps. Therefore, with the help of h-BN, graphene devices owns much higher mobility by assembling graphene with h-BN [56, 73]. Their excitons have longer lifetimes as the photoexcited electrons and holes were accumulated in different layers.

The vdW heterostructure can also be used for photovoltaic application. It has have been demonstrated with more efficiency based on TMDCs and graphene [71]. TMDCs ling-sensitive materials, while graphene is serving as channel materials and a transparent electrode with good ohmic contacts. It is also an option to combine materials with different work functions, which results in indirect excitons, such as MoS_2/WSe_2 [74]and $MoSe_2/WSe_2$ [75].

Light-emitting devices with heterostructure are also starting to emerge. Sine photoemission is a slow process compared to the penetration time between graphene and semiconductor, dwell time of injected electrons and holes should be under good control. Given this, h-BN layers can be introduced as a barrier to increase the dwell time of electron and hole in the TMDC [76]. Furthermore, A WSe_2 based device can reach a high quantum efficiency of 20% with increasing temperature and injection current [77].

1.4.2 Other kinds of vdW heterostructures

The above 2D vdW heterostructures gave birth to a new era of fundamental scientific studies and applied device designs. However, it remains a challenge to synthesize each 2D materials over large areas with high quality.

It should be noticed that vdW interactions are not limited to layered interactions. Any passivated, dangling-bond-free surface interactions are attributed to vdW forces. As a result, it is feasible to combine 2D materials with others of different dimensionality to form vdW heterostructures, so-called mixed vdW heterostructure (as shown in Fig. 1.11). This class of vdW heterostructures mainly focuses on layered 2D material as one of the ingredients, which describes as 2D + nD (n = 0, 1 and 3) in formula. Mixed vdW heterostructures have revealed the potential for device applications [78-80].

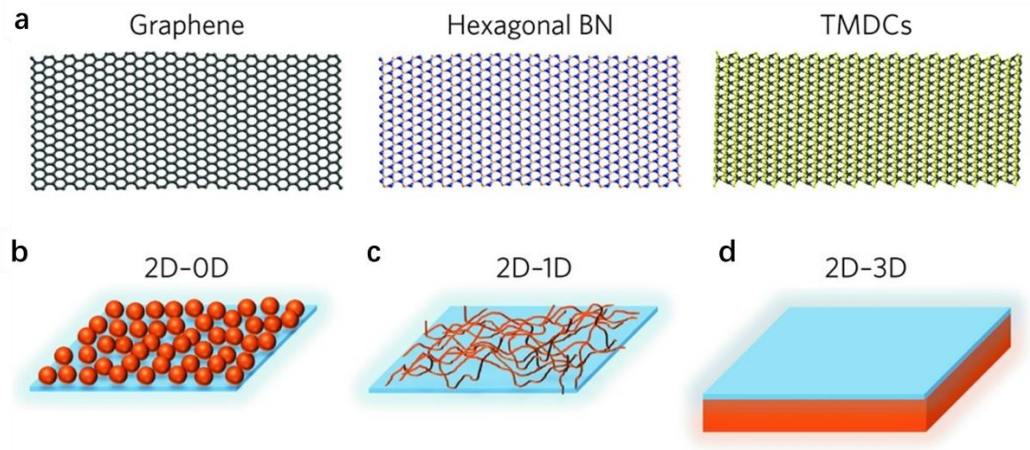

Figure. 1.11 (a) 3D models of the three primary 2D materials: graphene, h-BN, and TMDCs materials. (b) Heterojunction between a 2D material and 0D semiconductors such as quantum dots or small organic molecules. (c) Heterojunction between a 2D material and 1D materials such as nanotubes, nanowires or polymers. (d) Heterojunction between a 2D material and 3D semiconductors such as bulk Si, amorphous oxides or III–V compound semiconductors. Reprinted from [81], Copyright (2017), with permission from Springer Nature.

On the other hand, there have been some attempts at combining distinct 1D materials to form heterostructures as well [82, 83]. Previously in 1997, Suenaga et al.

reported a hybrid structure using arc-discharge synthesis [84], as shown in Fig. 1.12. The dominant products were nanoparticles, and a few nanotube-shaped products were also observed. Recently, Nakanishi et al. report a synthesis of BNNTs inside SWCNTs [85]. They encapsulated BN precursor in SWCNTs by a gas phase process, which was then annealed at 1673K for 3 days in vacuo. The main idea is to use a confined space of SWCNTs as a template to form BNNTs inside due to their structural affinity. Arenal et al. proposed experimental evidence of the formation by in situ electron-irradiation of SWCNTs confined within BNNTs [86]. However, their results were far from satisfaction because the as-prepared coaxial structures were poorly crystallized with lots of amorphous. The ideal 1D heterostructures with highly crystallized structure and continuous surface were only theoretically investigated by computer simulation [87, 88].

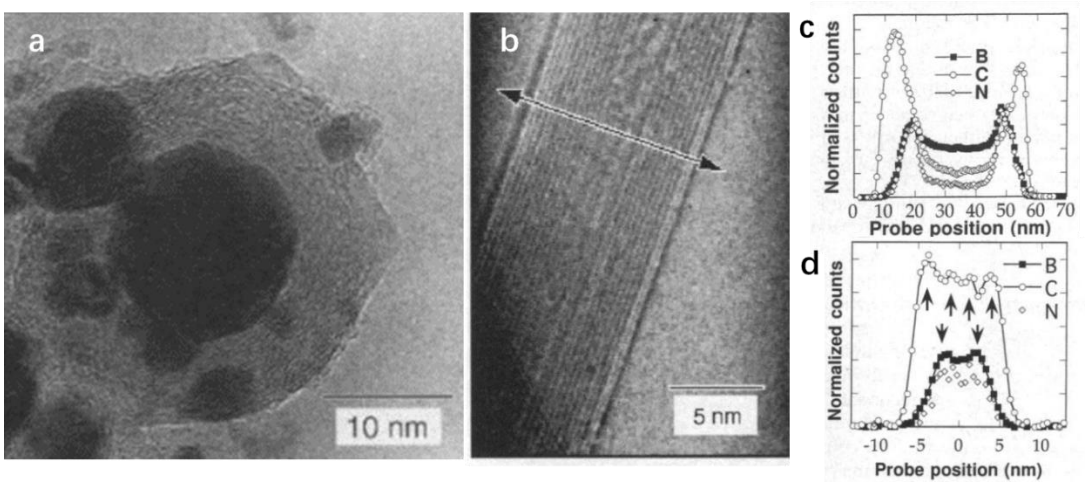

Figure 1.12 (a) TEM image of a polyhedral nanoparticle with a metallic hafnium boride core (darkest contrast) encapsulated by graphitic layers, and (c) its elemental profiles of B, C, and N. (b) TEM image of a composite nanotube with the C-BN-C sandwich structure, and its (d) elemental profiles measured across a tube.

1.5 Motivation and purpose of this dissertation

Researchers have been focusing on nanomaterials over the past several decades. More and more nanomaterials have been reported since they showed unique properties when their size is close to atomic scale. In contrast to 3D bulk materials, "Low-dimensional materials", including 2D, 1D, and 0D, is a term to describe such new class of nanomaterials in a lower dimensionality. It has been reported that low-dimensional materials show unusual properties due to the quantum size effects. For example, their density of states is significantly different from each other according to the calculation results, which makes low-dimensional materials a promising platform to develop next-generation devices.

With the increasing emergence of low-dimensional materials, more and more scientists try to design and manipulate materials in nanoscale in order to obtain new properties. In recent years, vdW bonded materials have attracted scientists' attention as they provide a new perspective to manipulate materials into heterostructures. 2D materials, as one of the low-dimensional materials, are considered as an important integrant for vdW heterostructures. As there is no requirement for symmetry and lattice matching among each layer, they can easily stack on top of each other, and thus form a great number of different kinds of 2D heterostructures. These new 2D have been reported to possess unique properties, such as surface reconstruction, charge redistribution, and proximity effects. With some special integrant, like graphene, h-BN, and TMDC materials, 2D heterostructures can be applied to graphene tunnelling device, photovoltaic applications, light-emitting devices and so on. Therefore, 2D heterostructures have been showing great prospect and application value in the near future.

However, vdW heterostructures are realized mostly in planar-based structure, while other kinds of vdW heterostructures in different dimension have not yet been deeply studied. For example, a 1D vdW heterostructure should be a coaxial structure that combines different kinds of single-crystal materials in the radial direction. Only a few simulations researches for 1D vdW heterostructures were reported [87, 88].

Previously there were some experimental results related to 1D vdW heterostructures. A hybrid structure C-BN-C using arc-discharge synthesis was reported by Suenaga et al, but the ingredients as well as their number of walls were

difficult to control especially under arc-discharge condition. Recently, a few groups also attempted to fabricate a C and BN coaxial structure [85, 86]. They tried to encapsulate the BN source or C source inside the nanotube. After some heating process, BN or C tube-like materials were formed inside. However, the result was not ideal, and the coaxial structure was poorly crystallized with lots of amorphous. Theoretically, we believe a true 1D heterostructure must be highly crystallized with continuous surface.

As we discussed above, little is known about the properties of heterostructures down to one dimension. Therefore, the first purpose of this dissertation is to explore the possible existence of true 1D vdW heterostructures. A further purpose of this research is to explore a stable synthesis strategy for 1D heterostructures with high quality, because an ideal 1D heterostructures with highly crystallized structure should be considered as a precondition for further experiments. Also, we will focus on their new properties and phenomena when heterostructure comes to one dimension, such as SWCNT-BNNT was predicted as a topological insulator [88].

1.6 Organization of this dissertation

This thesis begins with a brief introduction to several kinds of low-dimensional materials especially for 1D and 2D materials. For 1D materials, SWCNT, BNNT, and MoS_2 nanotube are reviewed, while for 2D materials, graphene, h-BN, and layered MoS_2 are generally introduced. Subsequently, the concept of vdW heterostructures and is presented with the purpose of manipulation of nanomaterials, by which we carried out a new research topic about vdW heterostructures in one dimension.

In Chapter 2, some general experimental techniques are introduced, such as CVD apparatus for synthesis, and Raman spectroscopy, SEM, TEM, and UV-Vis-NIR spectroscopy for characterization. The specific experimental details will be presented in the following chapters.

Chapter 3 initially presents the possible existence of binary 1D vdW heterostructures combined with SWCNT and BNNT with a superior quality compared to the previous research. The effects of reaction parameters on BN CVD coating method is discussed. We then give a general characterization of 1D heterostructures which includes SEM. TEM, Raman spectrum, and absorbance spectrum. Methods of tunable thickness of BNNT and patterned growth for BN CVD are also presented.

In chapter 4, we further introduce MoS_2 as a new integrant for the study of MoS_2-based 1D heterostructures. We firstly present a simulation results of bending energy for outer MoS_2 in SWCNT-MoS_2 heterostructure, which gives insights into some basic issues in a more complicated ternary 1D heterostructures of SWCNT-BNNT-MoS_2. The crystallinity of prepared ternary 1D heterostructures will be discussed and evaluated as well.

In chapter 5, a further investigation is proceeded by proposing the growth mechanism and three growth models for the formation of outer BN walls. The effect of isolation and cleanness for high high-quality synthesis is studied based on TEM results.

The relationship between inner and outer layers is revealed in Chapter 6. The discussion will be given on both epitaxial and handedness relationship based on a great number of TEM results.

Some preliminary experiments will be carried out in Chapter 7. We discuss the properties and applicability of 1D heterostructures, based on their thermal, optical, and electronic properties.

Finally, in the last Chapter 8, we present an outlook on the prospects of 1D vdW heterostructures, and the future perspectives with a wider range of 1D library.

Chapter 2: Experimental means

2.1 CVD

Direct growth methods such as CVD are promising techniques for scalable synthesis of vdW heterostructures. As it is widely used for 2D materials, including h-BN, graphene, and TMDC materials, a great number of different combination of heterostructures have been assembled, such as graphene/h-BN [89, 90], MoS_2/graphene [91, 92], GaSe/graphene [93], MoS2/h-BN [94, 95], and WSe_2/$MoSe_2$/ graphene [96].

In view of above successful application is 2D heterostructures, CVD technique may also play a key role in the synthesis of 1D heterostructures by selecting proper precursors and optimizing the reactions parameters.

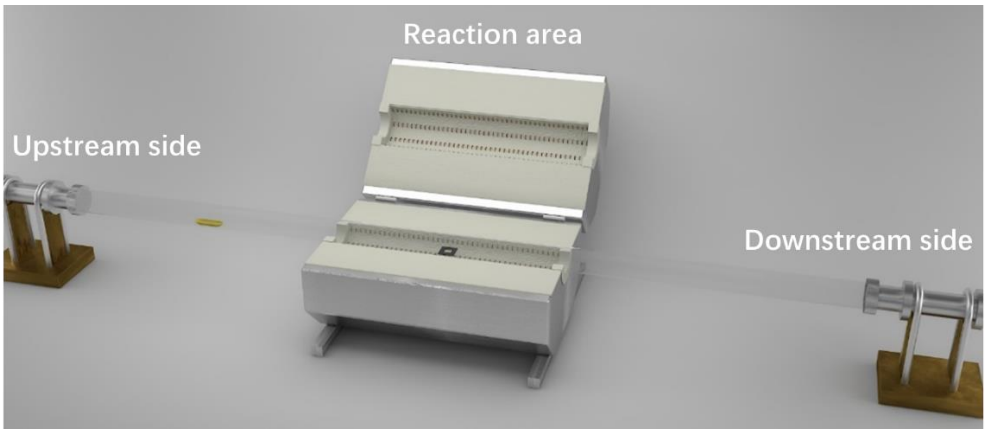

Figure 2.1 Schematics of the CVD systems, especially for BN CVD process.

Fig. 2.1 is the schematics of our CVD system. The CVD system contains three parts: upstream side, reaction area, and downstream side. In upstream side, several mass flow controllers are deployed to control the flow rate of carrier gas (Horiba STEC SEC-E40). A heating belt is also set in the upstream area in order to heat up precursor when needed. The main part of the reaction area is a ceramic furnace with a long quartz tube of 100 cm in length. In the downstream side, a scroll pump is used for high vacuum requirements. What's more, two pressure gauges are deployed for real-time measure of pressure, of which one is for high vacuum (<10 kPa) and one is for low

vacuum (>10 kPa), respectively. To precisely control the pressure, several kinds of valves are deployed as demanded. Specifically, the main valve and sub vale is used for high-pressure control, while the needle valve and butterfly valve high-vacuum adjustment.

2.2 Raman spectroscopy

Raman spectroscopy is a powerful and convenient technique used to study vibrational modes of molecules. When a sample is illuminated with a laser light, most of the scattering are elastic processes (Rayleigh scattering), which means the scattered photons have the same energy as the incident photons. In contrast, some inelastic processes (Raman scattering) happen with a very low probability, of which the scattered photons have a different energy from those of the incident photons. It means that there is an exchange of energy during the scattering process, resulting in the higher or lower energy of laser photons. More specifically, phenomenon of reemitted photons with lower energy than original photon is called Stokes Raman scattering, while scattered photons with higher energy than the original photon lead to a phenomenon called anti-Stokes Raman scattering. The energy of the laser photons being shifted up or down is denoted as Raman shift (in the unit of cm^{-1}).

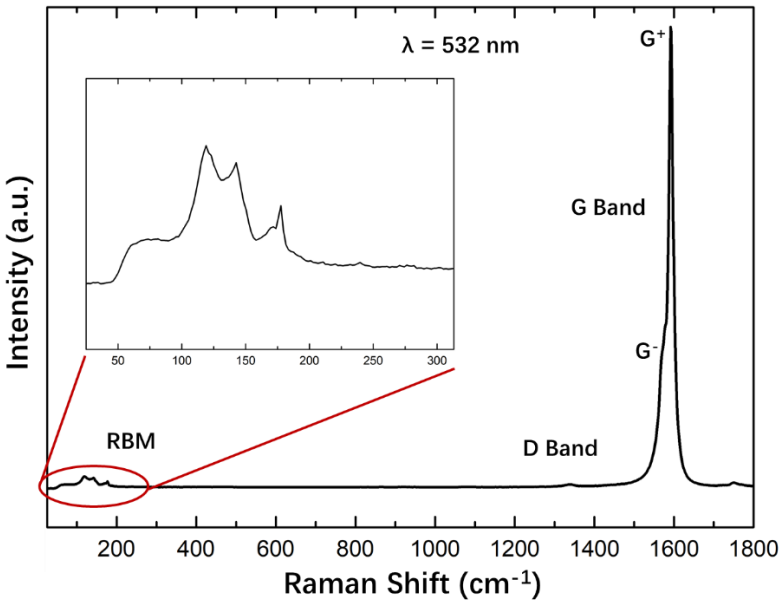

Fig. 2.2 Example Raman spectrum taken from SWCNT films (532 nm excitation laser). The inset is the RBM.

Figure 2.2 is a typical Raman spectrum of SWCNT films. RBM, D band, and G band region are three of the main features of SWCNT. The dominant peak at around 1590 cm^{-1} is the G band, in which G represents for graphite. This peak corresponds to the in-plane vibrational mode of carbon atoms. Moreover, G band peak generally spilt into G^- and G^+ modes due to the energy difference between axial and transverse in-

plane vibrational modes. D band around 1350 cm^{-1} is a disorder-related peak, including defects or inconsistencies in the carbon crystal lattice. Therefore, we could use a G/D ratio to determine the crystallinity of a SWCNTs sample. RBM shown in the inset of Fig 2.2 is a series of peaks below 400 cm^{-1}. These peaks are caused by the coherent movement of all the carbon atoms as in radial direction, like a “breathing” nanotube. Therefore, RBM is short for radial breathing mode. We could get much information by characterizing RBM, such as tube diameter [97], and the chirality of SWCNT [98].

2.3 SEM

With the going deep of the nanomaterials, research of low-dimensional nanomaterials relies more and more on the development of metrological technology, especially for the present invention in electron microscope.

SEM is a type of electron microscope that is indispensable tool for low-dimensional materials characterization in micro or even nano scale. Images are obtained by scanning the sample surface by an electron beam, then the secondary electrons are deal with by secondary electron detector. As for an optical microscopy, the resolution can be described as

$$\sigma = \frac{0.61 \times \lambda}{n \times sin\theta}$$

in which λ is the wavelength of light, n is the RI, and θ is one-half of the objective's opening angle. We can learn from this equation that it is difficult to obtain higher resolution in the visible-light range. However, electron owns a smaller wavelike nature. This is why the electron microscopy can produce an image with much higher resolution than the optical microscopy.

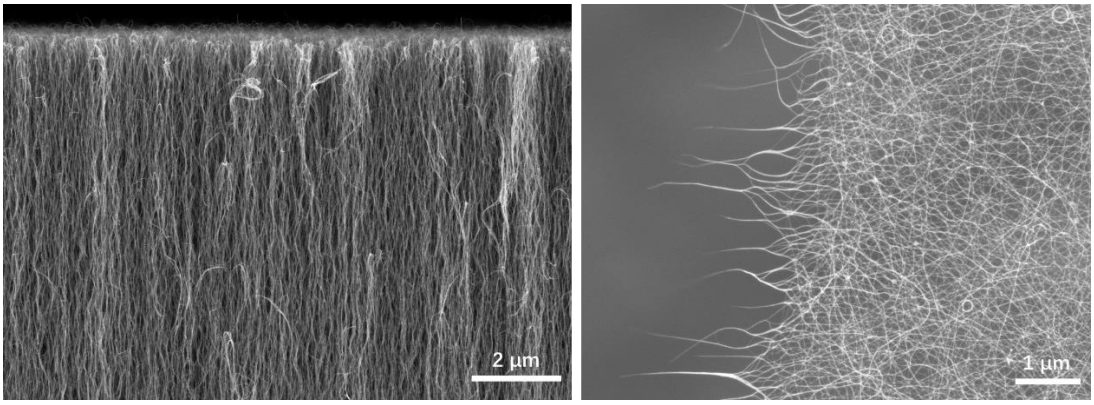

Figure 2.3 Hhigh-resolution SEM image of vertically-aligned SWCNT forest (left), and SWCNT network (right).

Fig. 2.3 shows two SEM images for SWCNTs in different form. Their morphologies can be recognized, and even each nanotube can be readily distinguished from each other. For conductive sample, like SWCNTs, the voltage for accelerating electrons is usually applied in 1.0 kV, so the sample will not be damaged while high-

resolution images can be obtained. A semi-conductive sample, on the other hand, need a higher voltage for a better resolution of SEM image.

2.4 TEM

TEM is another type of electron microscope for nano-scale characterization, with an even higher magnification exceeding 1,000,000 X. A TEM image is obtained not by detecting secondary electrons, but by the transmitted electrons that go through the sample. This requires the sample to be thin enough so that electrons are able to pass through with high energy (>100 keV). A TEM image of SWCNT-BNNTs is shown in Fig. 2.4. Each layer of nanotube can be distinguished from each other at atomic resolution.

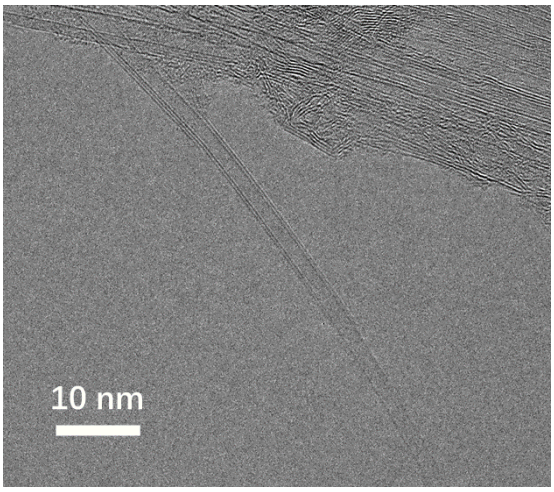

Figure 2.4 Individual nanotube that can be considered as a SWCNT partially coated by BNNT.

In our lab, we also have developed a TEM positioning technique, which is of great benefit to most of our experiment (as shown in Fig. 2.5). The main idea is to label one area before experiment, then observe the same area again. This technique is very useful when you need to compare the difference before and after some chemical experiments.

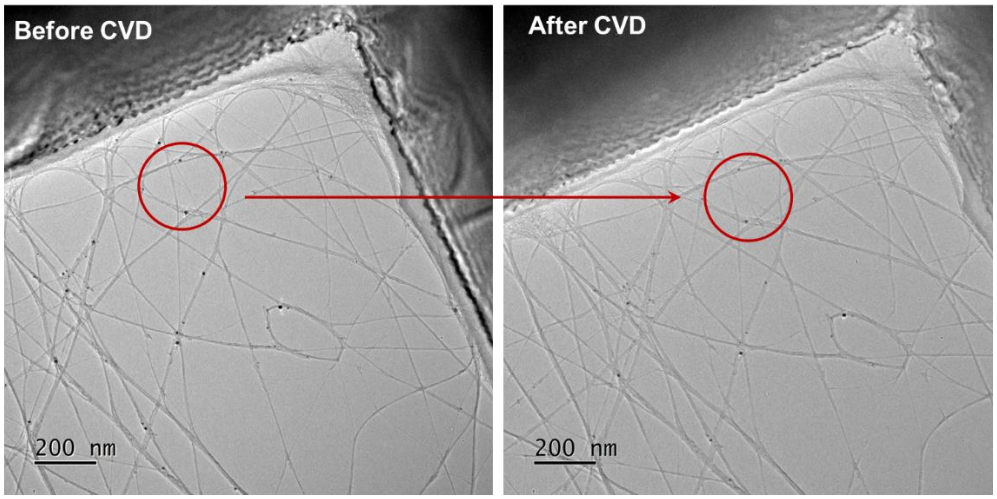

Figure 2.5 A TEM positioning technique for an "in situ" comparison. One area of the pristine SWCNT (left) is labelled by a red circle in the TEM image. After certain CVD process, we can check how this area changes as long as the same area can be located (right).

2.5 UV-Vis-NIR spectroscopy

UV-Vis-NIR spectroscopy refers to absorption spectroscopy or reflectance spectroscopy covering some spectral range like ultraviolet, visible, and near infra-red spectral regions. When light go through a sample, its intensity follows Beer-Lambert Law:

$$I = I_0 e^{-\alpha L c}$$

where I is the received light intensity, I_0 the incident light intensity, α the absorption coefficient, L the optical path length, and c the concentration of an absorbing species. Transmittance T is measured by the ratio of received light intensity to incident light intensity as:

$$T = \frac{I}{I_0}$$

then the absorbance A can be given by the following relationship:

$$A = -\log_{10} T$$

Both transmittance T and absorbance A is deals with the received light in transmission mode. This optical technique is very useful for characterization and analysis.

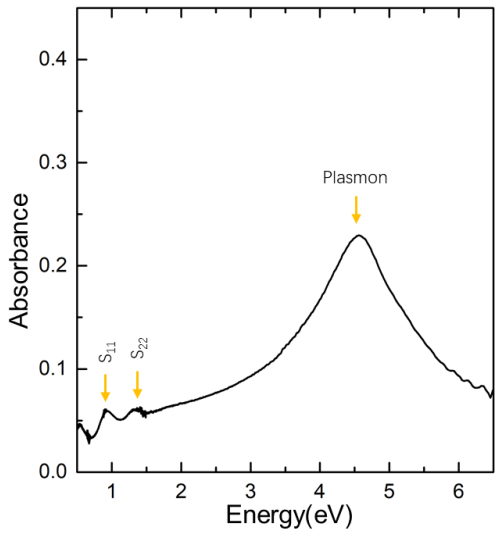

Figure 2.6 Typical optical absorption spectra of SWCNT film. Absorbance band of S_{11}, S_{22}, and Plasmon bands are shown.

Fig 2.6 is an absorbance spectrum of a SWCNT film. if the incident photon energy satisfies the energy separation between *i*th valence band and conduction band, the probability of absorption processes increases dramatically. S_{11} and S_{22} peak represents for E_{11} and E_{22} of semiconducting SWCNTs, respectively. Their position can determine not only diameter but also metallic or semiconducting properties of the SWCNT.

Chapter 3: CVD synthesis of SWCNT-BNNT heterostructures

In this chapter, we will focus on how we synthesize 1D SWCNT-BNNT heterostructures with high quality by CVD method, which is initially developed by our research group. Results of their structure characterization will be reported as well.

3.1 CVD apparatus

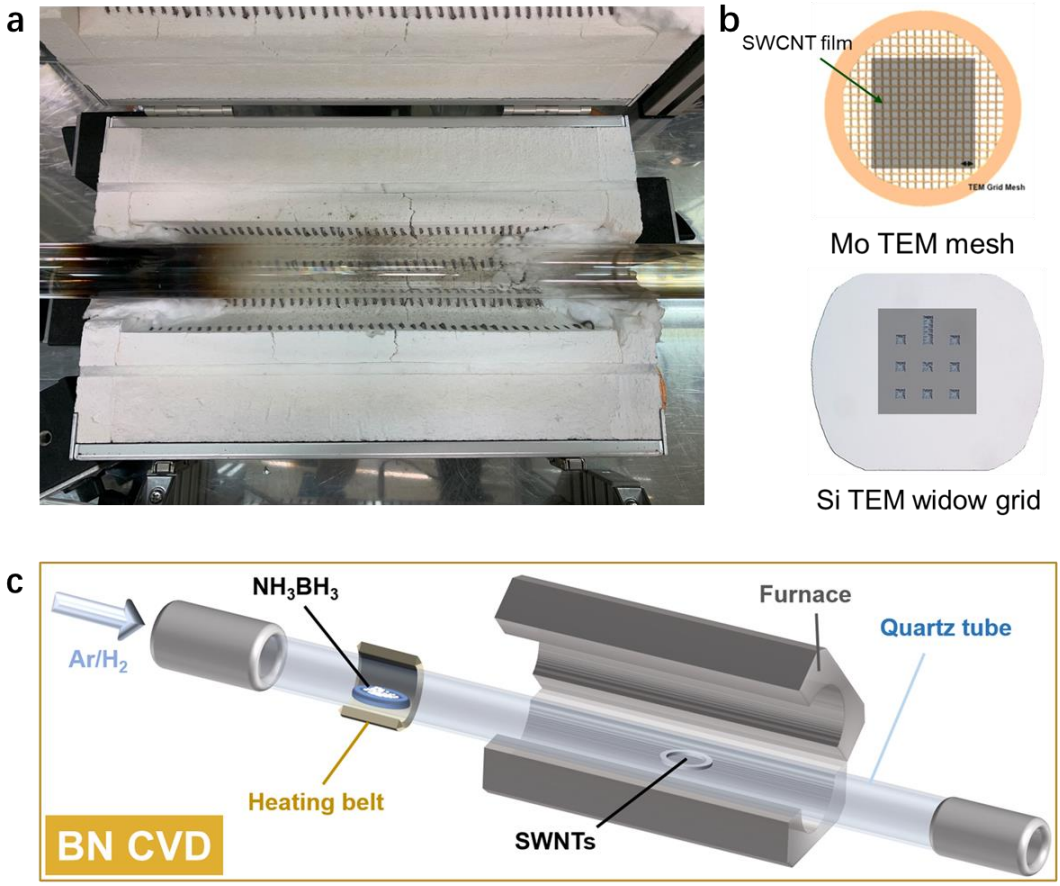

Figure 3.1 (a) Photograph of the BN CVD system. (b) Schematics of two types of TEM micro-grid: Mo-based TEM mesh grid and Si-based TEM window grid. (c) Schematic illustration of BN CVD system.

The main idea for our CVD method is to use SWCNT as the skeleton and choose a BN precursor to coat on SWCNT surface. The SWCNT sample was provided by The

NanoMaterials Group, Aalto University [99]. In order to precisely characterized the coating quality in nanoscale, most of our experiments were conducted on TEM grids, which is convenient for further TEM characterization. Fig. 3.1b shows schematics of two types of TEM micro-grid. A SWCNT film was transferred onto the TEM grid for further experiments.

CVD is one of the main fabrication methods for 2D vdW heterostructures, so we believe CVD should also be a practical option to form 1D vdW heterostructures. Fig. 3.1a is our furnace we used for the CVD process. After experimental trials and characterizations, a facile CVD method was given with high repeatability. Fig. 3.1c is the schematic illustration we used for BN coating process. Ammonia borane complex was used as BN source. 30 mg of BN source were put in a quartz boat and placed upstream from the left. Our SWNTs sample was placed in the middle of the furnace. Ar mixed gas with 3% H_2 was introduced as carrier gas at a flow rate of 300 sccm. The pressure was tuned at a low valued around 300 Pa. During the ramp-up period, CVD furnace was heated to 1075 °C, and then the upstream part was heated at about 70°C by a heating belt. During the CVD growth, these temperatures were kept constant, and BN source vaper was transferred downstream by carrier gas. CVD duration varied from 1 to 3 hours depending on thickness requirement of BNNT.

3.2 Reaction parameters

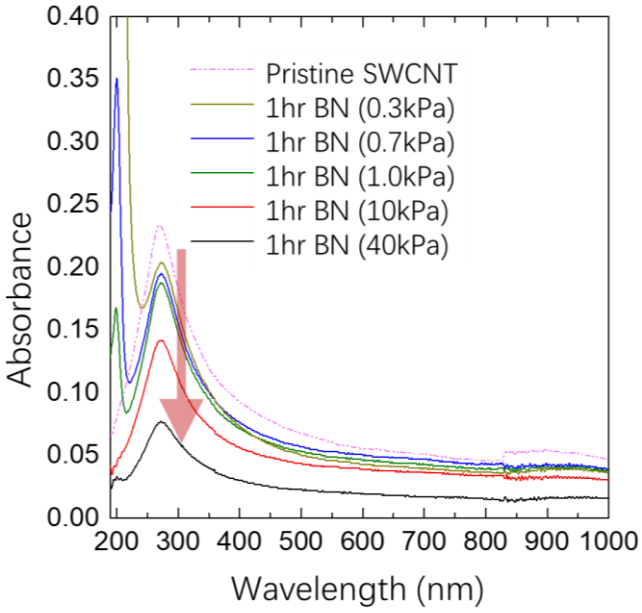

Figure 3.2 Evolution of absorbance spectra of sample after BN CVD at different reaction pressure from 0.3 to 40 kPa.

Firstly, the effect of pressure in BN CVD was investigated. Pressure is one of the crucial parameters for BN CVD. It can be tuned by sub valve at high vacuum, butterfly valve in low vacuum. Fig. 3.2 is the absorption spectra for different samples at different pressure values. In these spectra, a band gap of approximately 200 nm can be observed for BNNTs. These additional peaks are assigned to BNNTs with their transitions [100], and more products of BNNTs result in a stronger intensity of the peak.

Fig. 3.2 is the evolution of absorbance of SWCNT-BNNT samples with different pressure. The peak intensity of BNNTs decreased when pressure went up. When pressure went up to 40k Pa, the peak intensity of BNNTs almost disappeared. We speculate that the decomposition of ammonia borane complex was suppressed at higher concentration of H_2 based on the following chemical equation:

$$H_3N\text{-}BH_3 \rightarrow BN + H_2$$

One more thing we found is that the plasmon peak of SWCNT showed similar tendency. The peak density dramatically dropped down when the pressure is over 1.0k Pa. This is because carbon structure was etched by H_2 with high concentration.

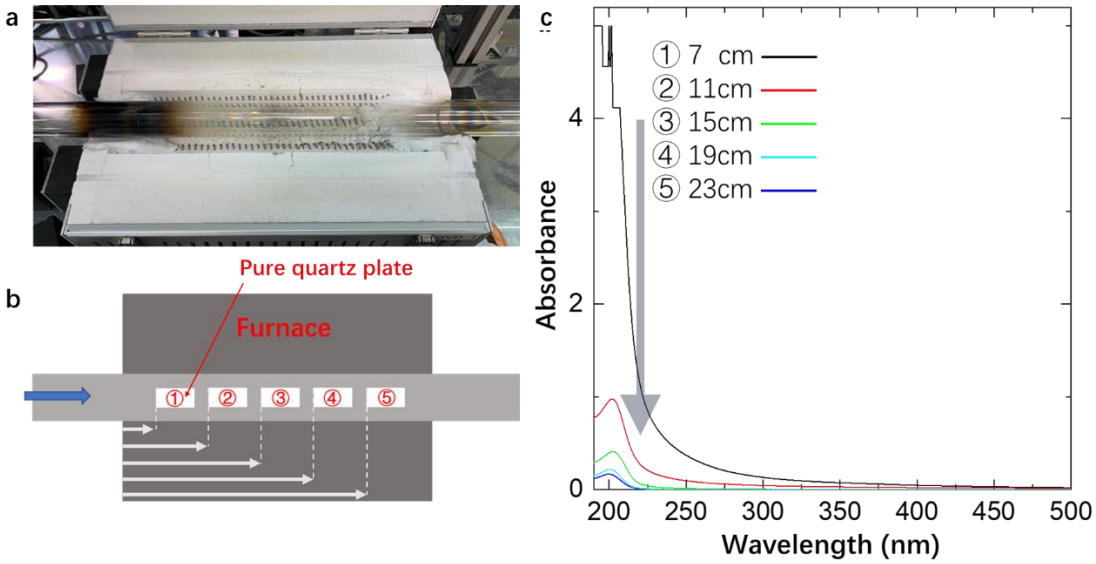

Figure 3.3 (a) Photograph of the BN CVD system after long-term use of BN coating process. (b) Schematic illustration of experimental method with different position of quartz plate. (c) Evolution of absorbance spectra of sample after BN CVD at different position in quartz tube.

The position of sample in furnace is also an important parameter for BN CVD. Figure 3.3a is the furnace we used for synthesis. The BN source comes from the left as the upstream side. 5 samples of SWCNT film were prepared for the experiment. The first sample was placed 7 cm from the left, then the other 4 samples were placed every 4 cm from each other to the right (Fig. 3.3b). Absorbance will be checked for each sample after 1-hour BN CVD process. Fig. 3.3c is the evolution of absorbance of each sample with different position. The spectrum in black line represents the leftmost sample. The peak intensity around 200 nm was too strong that the peak was deformed at its maximum value. The intensities of spectra of other samples were gradually decreased along the rightward position.

As shown in Figure 3.3a, it should be noticed that the upstream part of quartz tube gradually turned dark as more and more BN CVD were performed. At the same time, the closer the sample is to dark deposition is, the stronger intensity its spectra get. Therefore, we assume these dark depositions belongs to by-product of BN decomposition, and they began to deposit at high-temperature region. In position 2 to 5, the quartz tube became cleaner and cleaner, and the peak intensity of corresponding sample also relaxed to a normal level. We also checked TEM for their growth quality.

Fig. 3.4a and b show two TEM images for SWCNT-BNNT samples in position 3 and 4, respectively. A rough tube surface of sample in position 3 was confirmed, but the sample in position 4 showed a much higher crystallinity with continuous tube surface. Consequently, the optimal position for BN CVD is not in the middle, but a little closer to the downstream side. This is one of the most important growth parameters for BN related 1D vdW heterostructure.

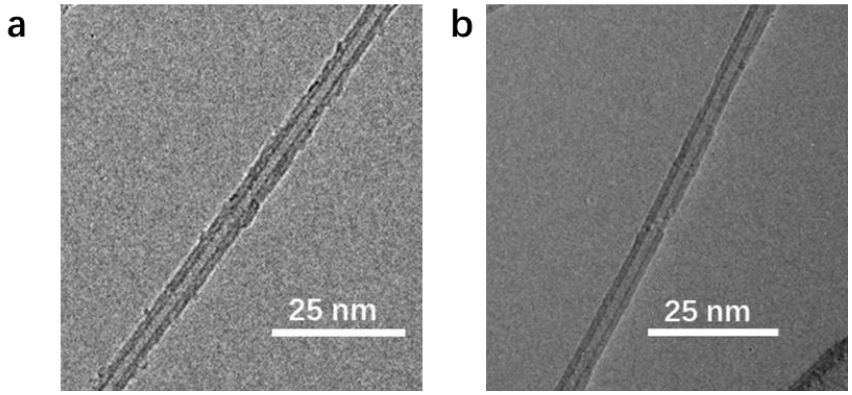

Figure 3.4 Two TEM images for samples after BN CVD in position 3 (a) and 4 (b) of the furnace, respectively

3.3 Structure characterization

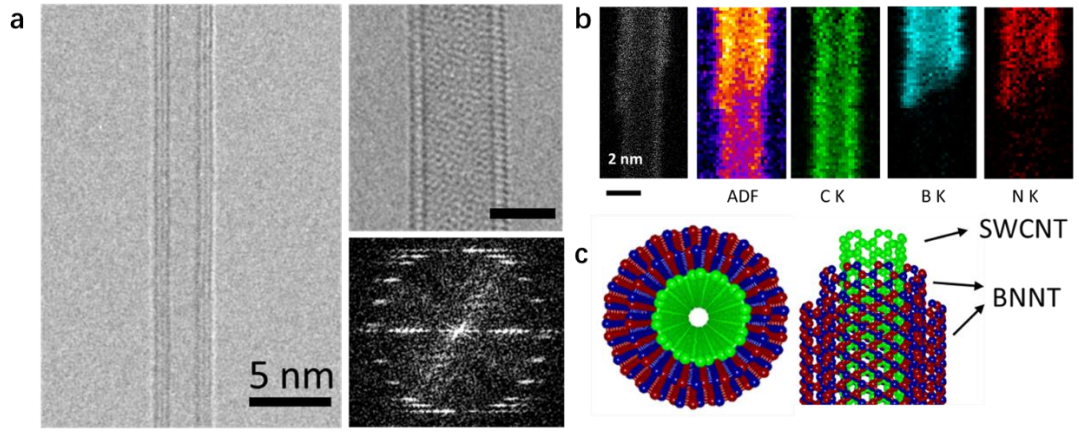

Figure 3.5 (a) Two TEM image of SWCNT sample after BNCVD and its ED pattern. (b) Annular dark-field (ADF) image and EELS mapping of a SWCNT partially coated by BNNT, showing that the inner layer is carbon and the outer layer is BN. C K, K_1 edge of C (green); B K, K_1 edge of B (cyan); N K, K_1 edge of N (red). (c) 3D model for SWCNT-BNNT coaxial structure.

In this section, we will present more experimental results about the structure characterization in nano scale. Fig 3.5a is some of the TEM results after 1hr BN CVD. We can see that the nanotube was nicely formed, and its surface is very clean. Most importantly, the nanotube was not single-walled anymore, and the number of walls increased to 2 or 3. It looks like some other nanotubes nicely wrapped around the pristine SWCNTs. Furthermore, its ED pattern is highly symmetric due to the high-quality structure.

Here is the question: how we can tell that the outer wall is BNNT rather than CNT. As the starting material is purely single-walled before we performed BN CVD, it is quite reasonable to expect that the outer walls are BN, but we still need conclusive scientific evidence.

This assumption was further proved by EELS mapping. Here we checked one nanotube with a distinguishable outer wall (Fig. 3.5b). It turns out that the distribution of boron element and nitrogen element was the same outside (blue and red colour), but the C was uniformly distributed inside (green colour). Based on this result, we proposed a coaxial structure that is composite of SWCNT inside and BNNT outside,

as illustrated in Fig 3.5c with the 3D models. This structure can be considered as 1D heterostructures with two different ingredients in one dimension.

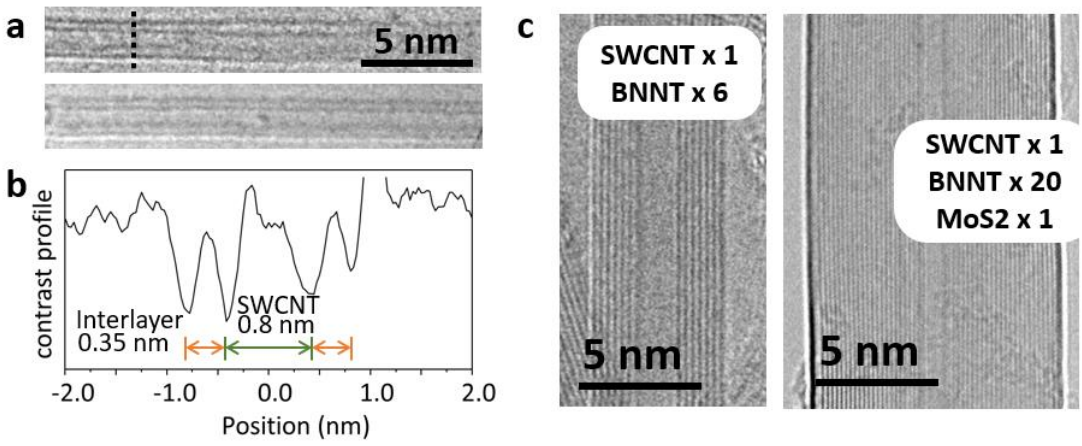

Figure 3.6 (a) Two TEM images of SWCNT-BNNT nanotube with small diameter in different focus, and (b) its fringe intensity depends on perpendicular direction. (c) Two TEM images of 1D heterostructures with large diameter.

The coating process of BN layers can be applied in the same way on individual SWCNT with very small diameter. Figure 3.6a shows two TEM images for as-prepared hetero nanotubes in different focus, of which the innermost SWCNTs have very small diameter. Fringe intensities of these TEM images is shown in Figure 3.6b. Fluctuations in valley depth for particular layer are seen as a function of distance along the long axis of the hetero-nanotube, which clearly shows that the diameter of SWCNT is only about 0.8 nm with a 0.35 nm interlayer spacing of SWCNT-BNNT. This interlayer spacing is almost the same as that of 2D vdW heterostructures. As a result, we concluded that interaction between each layer belongs to van der Waals forces.

Long-time CVD process is feasible if we need a much thicker BNNTs. In Figure 3.6c, the TEM image on the left shows a hetero-nanotube with binary components of SWCNT-BNNT, in which one SWCNT is coated with six walled BNNT. In the right TEM image, even a twenty walled BNNT can be achieved, which is then followed by a single-walled MoS_2 (MoS_2-based heterostructures will be discussed in the next chapter). This neat and orderly structure also means the fabrication of the perfectly single-crystalline hetero nanotubes is achievable during long-duration CVD.

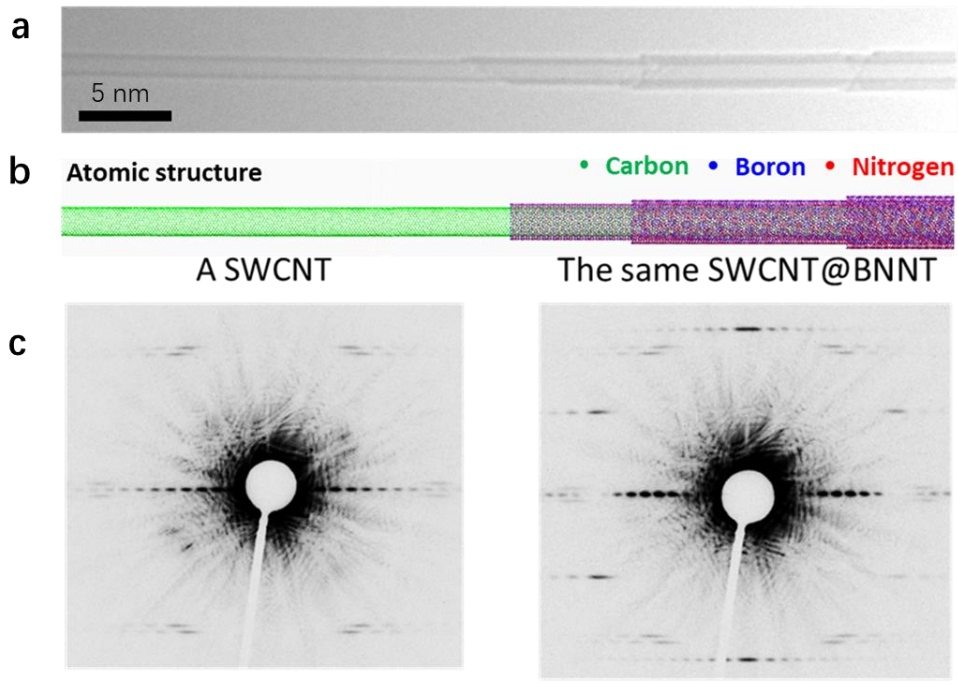

Figure 3.7 (a) TEM image and (b) its corresponding atomic structure of SWCNT-BNNT heterostructure with ladder-shaped surface. (c) ED pattern of bare part of SWCNT (left), and that of BN coated part (right).

What' more. The outer BNNTs were in ladder-shaped structure, as shown in Fig 3.7a&b with a TEM image and an atomic structure. The number of walls gradually changed along one direction. If we checked electron diffraction for the bare part and coated part, different ED pattern appeared. In Fig. 3,7c (left), we can only find one ED pattern, which is belongs to the pristine SWCNT. When one more BN layer is coated, one more pattern appeared (right). This additional ED pattern is highly symmetric in hexagonal shape, which means the outer BNNT has a crystallinity as high as that of the inner SWCNT.

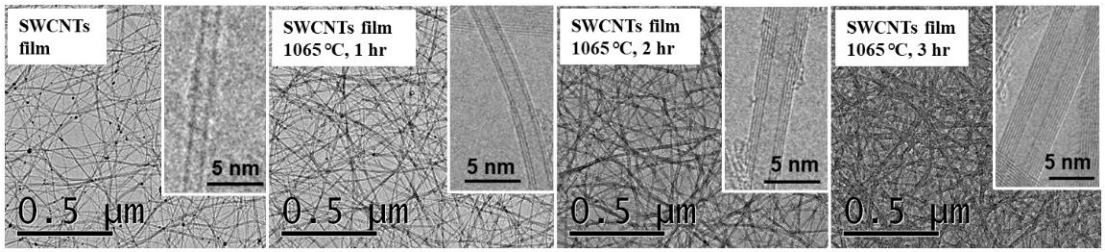

Figure 3.8 Evolution of TEM images of SWCNT sample with different BN CVD duration. Insets are the corresponding nanotubes at higher magnification.

By tuning BN CVD duration, we can control the thickness of outer walls. Fig 3.8 are more TEM results at different magnification. We conducted BN CVD with different duration. When BN CVD duration lasts for 1 hour, the number of walls increased to 2 or 3. Further with 2 hours BN CVD, the number of walls became 4-8. When BN CVD duration time increased to 3 hours, the number of walls can reach over 10. In lower magnification, we can see that the nanotube film was getting denser and denser. This is because the outer BNNTs is getting thicker. This experimental result is considered to be the first-time using CVD method to controllably synthesize few-walled BNNTs in good quality.

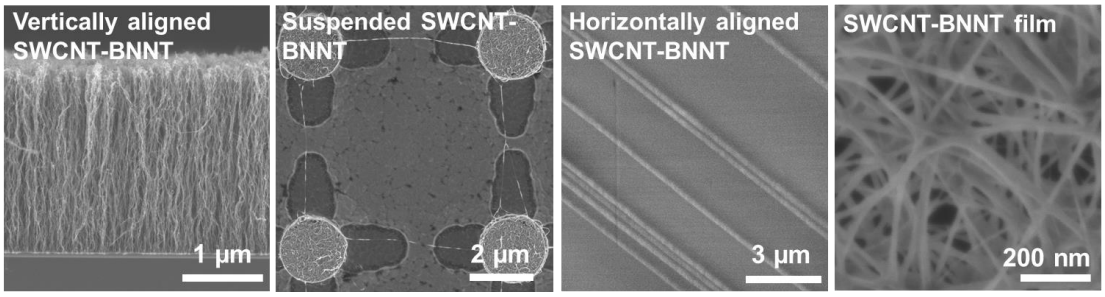

Figure 3.9 Four different forms of SWCNTs sample, which is already coated by BNNTs.

This BN coating method is easy to repeat, and it can be applied in SWNTs with different forms (as shown in Fig. 3.9). Such as vertically aligned SWCNTs, suspended SWCNTs, horizontally aligned SWCNTs, and SWCNT films.

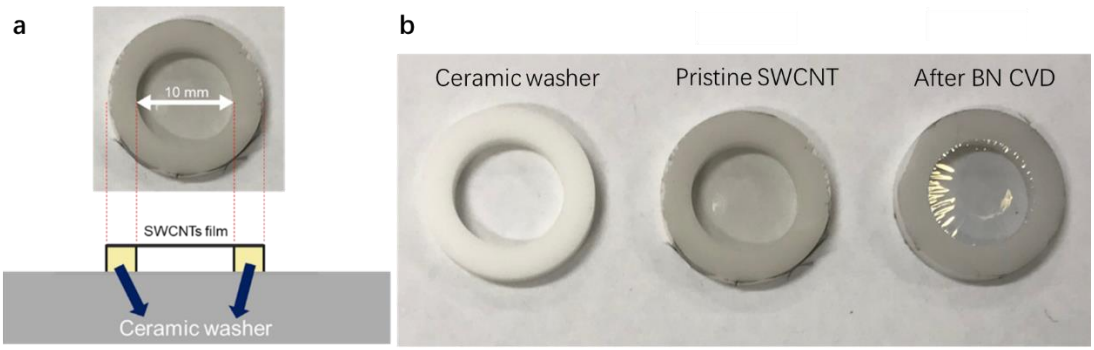

Figure 3.10 (a) Top view and front view of a suspended SWCNT film sample. (b) Evolution of the sample after transfer and BN CVD process.

As I mentioned above, most of our experiments were conducted on TEM grids. However, it is also feasible to do it in macro scale, because a macro scale sample is easier to operate and more achievable for optical and thermal experiments.

Fig 3.10a shows how the sample looks like from top view and front view. The main idea is that we used a ceramic washer as the substrate with its high temperature resistance, then transferred the SWCNT film onto the surface of ceramic washer. With a big hole in the middle, a part of the film will be suspended. Thanks to this structure, both sides of the film can be fully exposed to BN source during CVD so that all the nanotubes can be uniformly coated by BN layers. Fig 3.10b is optical image. We can see that the pristine SWCNT film is almost transparent (90% transparency), and the film becomes shinny with some wrinkles after 3hr BN CVD. The wrinkles may result from the thermal expansion of ceramic washer.

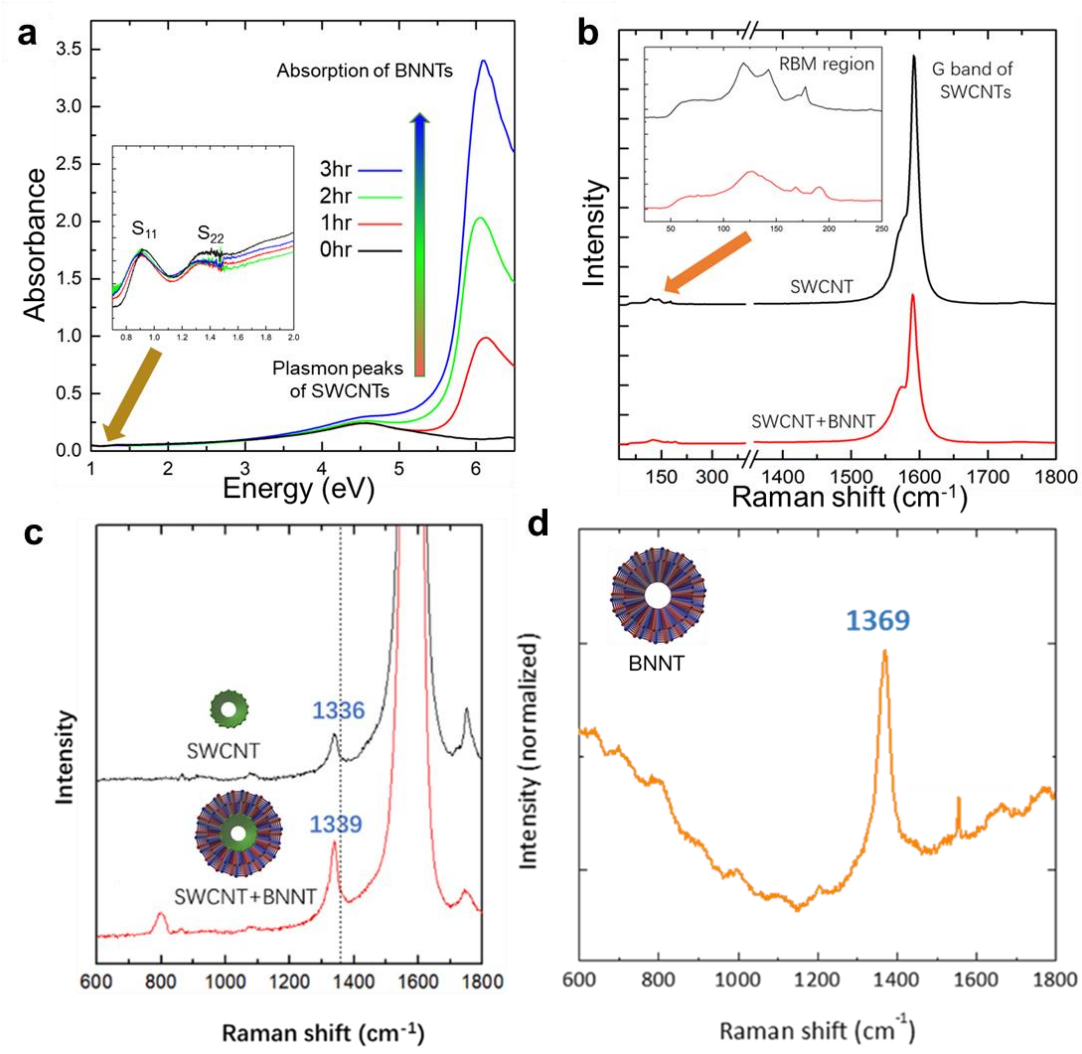

Figure 3.11 (a) Evolution of absorption spectra and (b) Raman spectra for SWCNT-BNNT samples before and after BN CVD process, and (c) its shorter range from 600 cm^{-1} to 1800 cm^{-1}. (d) Raman spectra of SWCNT-BNNT after O_2 annealing.

With this suspended film in macro scale, we can easily get its absorbance and Raman spectra. As for the Absorbance, there is a peak around 6eV representing the existence of BN, and its intensity increased with BN CVD duration. On the other hand, the S_{11}, S_{22} (inset of Fig 3.11a) and plasmon peaks were still preserved after BN CVD process.

In Raman spectra (532-nm laser), the retained RBM and G band region indicates that the structure of inner SWCNT is not noticeably affected by the BN coating process. As for normal h-BN crystal, one peak at around 1365 cm^{-1} is visible in all the Raman

spectra. For SWCNT-BNNT binary structure, a peak at 1339 cm^{-1} can be observed (Fig 3.11c, red line), which is very close to the D band peak of pure SWCNT at 1336 cm^{-1} (black line). According to previous researches [101], BNNT at 1370 cm^{-1} corresponds to the A_1 tangential mode of the nanotubes. However, we could not observe the peak at 1370 cm^{-1} from Figure 3.11c since its intensity was too weak compared to the D band peak of SWCNT, which means the BNNT peak was overlapped by D band of SWCNT.

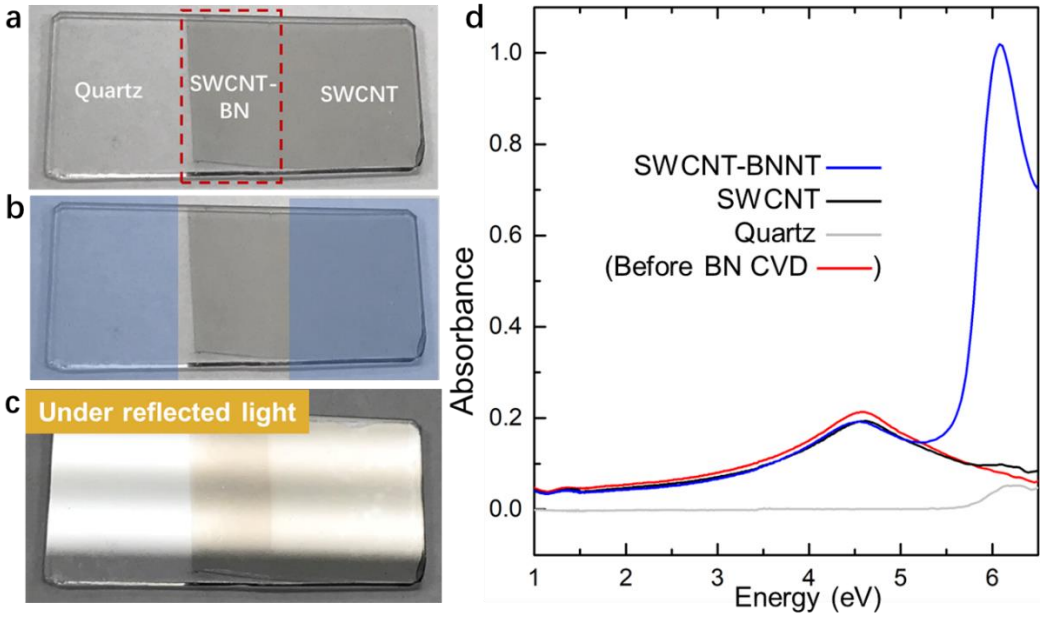

Figure 3.12 (a) Photograph of a film sample on quartz plate after BN CVD. (b) Sheltered areas are coloured blue. (c) Film sample on quartz plate under reflected light. (d) Absorption spectra of different area on the quartz plate.

To exclude the influence of SWCNT, we could anneal the sample in oxygen to burn all the SWCNT. Figure 3.11d is the Raman result after air annealing with pure BNNTs remained. We can observe the normal Raman signal of 1369 cm^{-1} by 532-nm laser, but we were not able to check its RBM region without UV-Raman spectroscopy.

Moreover, we can also control the growth area on a macro level. Fig 3.12a is a quartz plate after BN CVD. The part on the left is bare quartz, and the right part is SWCNTs. We can grow BNNT on the specific area we want. The middle area marked by dashed box is coated with BNNT already.

The main idea is to use another quartz plate to put another quartz plate on the sample surface as a shelter (blue square in Fig 3.12b). However, it seems there is no difference between BN coated area and SWCNT area from Fig 3.12a, but if we see through reflective light, each area will show different color contrast, as shown in Fig 3.12c. If we check the absorption spectrum for each area, they will show totally different curves. From Fig 3.12d, we can see that the spectrum of sheltered SWCNT after BN CVD is almost the same as pristine SWCNT, and the sheltered bare quartz plate only exhibited a small peak of BN. Only BN coated area exhibits a peak with high intensity around 6 eV. Therefore, BN coating process has been suppressed in the patterned area.

Chapter 4: CVD synthesis of MoS_2 based heterostructures

So far, we only talked about one material, BNNT, as the outer wall, but we believe the SWCNT is also possible to be coated with other kinds of materials. As we known, TMDC materials is one of the important integrant in 2D heterostructures, and MoS_2 as a member of TMDC family is the second most researched 2D material after graphene. It can be indirect or direct bandgap semiconductor depending on number of layers. In short, MoS_2 shows a lot of interesting properties and promising device applications, so we believe it can also be a good candidate for 1D heterostructures.

4.1 CVD apparatus

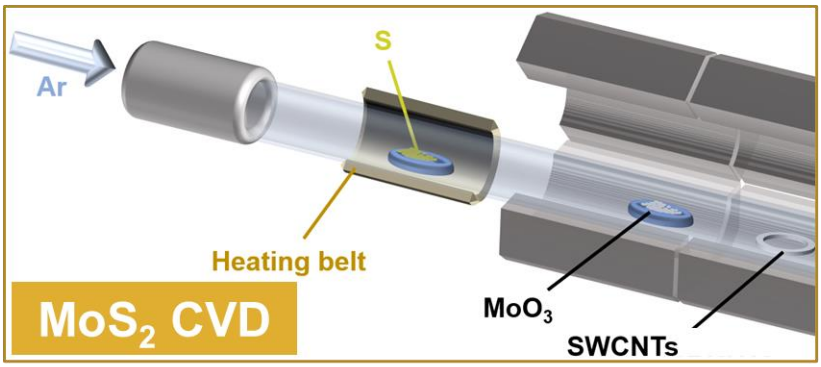

Figure 4.1 Schematic illustration of MoS_2 CVD system.

Compared to BN CVD apparatus, CVD system for MoS_2 is much more complicated. The reaction to synthesize MoS_2 can be described as:

$$2MoO_3 + 7S \rightarrow 2MoS_2 + 3SO_2$$

which means there are two precursors introduced during the CVD process. As shown in Fig 4.1, sulfur power was put in a quartz boat in the upstream side as the first precursor. This zone was heated by a rubber heater with setting temperature at 138°C as the sublimation temperature of sulfur is around 113°C. In the reaction area, we used two-zone ceramic furnace. One zone was for sublimation of MoO_3, the other zone was for the synthesis of MoS_2, in which the SWCNT film sample was placed. During the

MoS_2 synthesis process, sulfur in gas state went through reaction area, and the remaining sulfur would finally deposit at downstream side. As a result, a cold trap should be deployed between the reaction area and the scroll pump to avoid physical damage by cool-down sulfur in solid state.

4.2 Structure characterization

4.2.1 SWCNT-MoS_2

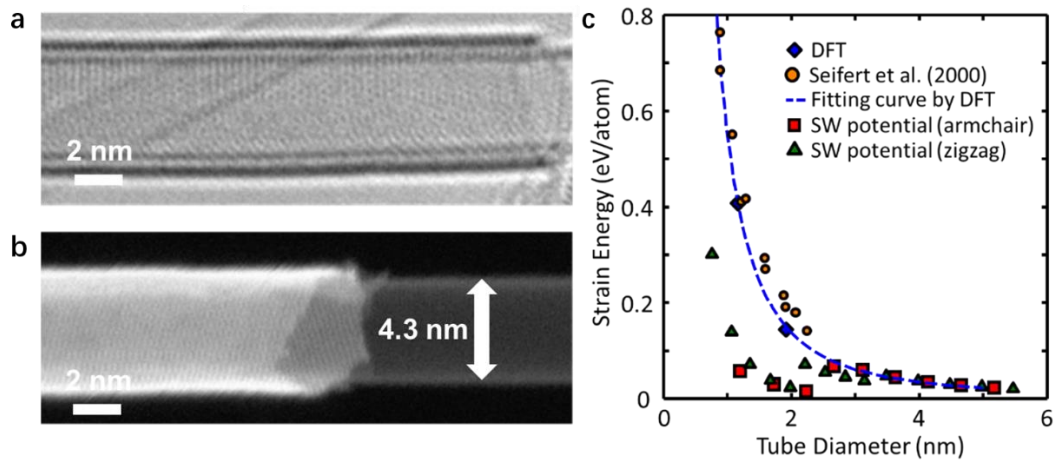

Figure 4.2 (a) HRTEM image (b) HAADF STEM image of a single-walled MoS_2 nanotube grown on a SWCNT. (c) Strain energy of a single-walled MoS_2 nanotube as a function of tube diameter.

We conducted the above MoS_2 CVD process on SWCNT film, and we did find some areas with nice coaxial structures similar to SWCNT-BNNT under TEM measurement. In Fig 4.2a, we see a nanotube with distinctly different outer layer, which should belong to MoS_2, in tube-shaped structure, so we can call it MoS_2 nanotube. Different from BNNT in TEM image, this MoS2 nanotube has a deeper grey level, a larger diameter, and a larger interlayer spacing with the inner wall. Therefore, we can easily distinguish BNNT and MoS_2 nanotube from each other by a TEM measurement.

However, the yield of MoS_2 nanotube is really low compared to BNNT. One of our collaborative members, Hisama, performed simulations of single-walled MoS_2 nanotube with different diameters, as shown in Fig 4.2c. The y axis is the strain energy. The simulation results indicate that the strain energy of MoS_2 NT was much higher compared to SWCNT and BNNT in small diameter. This is because a monolayer MoS_2 contains 3 atomic planes, so it will become unstable when it was rolled into a tubular structure.

Fig 4.2b is another example of a TEM image with clear inner SWCNT and outer MoS_2 nanotube. The diameter of inner SWCNT even reached to 4.3nm, which is rarely seen for SWCNT materials. According to the simulation result in Fig 4.2c, a MoS_2 nanotube with diameter over 4 nm results in a very low strain energy. Based on this TEM result, we proposed a coaxial structure that is composite of SWCNT inside and MoS_2 nanotube outside in one dimension, as illustrated in Fig 4.3 with the 3D models.

Cohesive energy is also another factor may need to be considered in 1D heterostructures. According to Hisama et al.'s simulation results of SWCNT-BNNT [102], the minimum of cohesive energy at 3.5 Å is around 0.01 eV/atom, while the bending energy varies from 0.8 to 0.03 eV/atom. In MoS_2 case, cohesive energy should be the same due to the van der Waals interactions. Apparently, the order of magnitude of bending energy is larger than that of cohesive energy, and the bending energy should play a leading role in deformation of layered materials. Therefore, it would be better to leave out cohesive energy in stain energy simulation especially for nanotubes with small diameter.

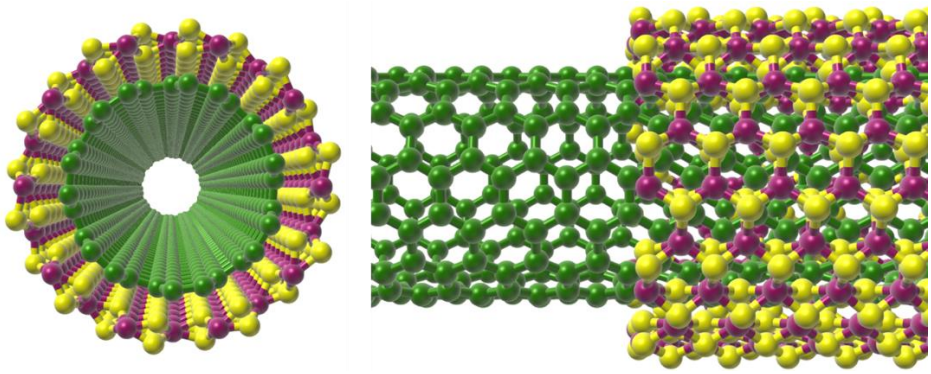

Figure 4.3 Atomic 3D model of SWCNT-MoS_2 nanotube in coaxial structure.

4.2.2 SWCNT-BNNT-MoS_2

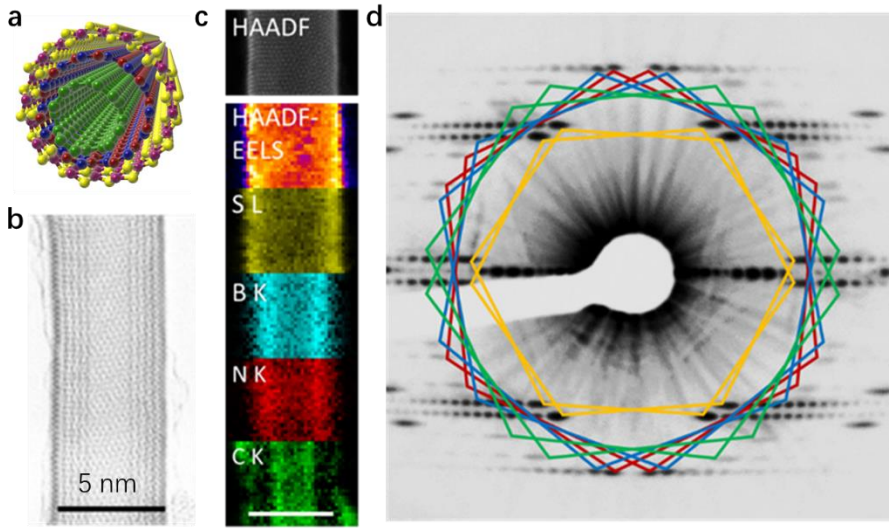

Figure 4.4 (a) Atomic 3D model, (b) TEM image, (c) EELS mapping, and (d) ED patterns of a 5nm SWCNT-BNNT-MoS_2 ternary nanotube.

Based on the previous two experiment results on BNNT and MoS_2 nanotube, we conclusively demonstrated a ternary coaxial structure with an atomic model in Fig. 4.4a. We first grow BNNT on SWCNT to form a binary 1D heterostructures. Then, with more layers of BN, the diameter of nanotube gets larger. It means that the coating of outer MoS_2 nanotube becomes much easier.

TEM image in Fig 4.4b is a 5nm coaxial nanotube, including 1 layer of SWCNTs, 3 layers of BNNTs, and 1layer of MoS_2 nanotube. Fig 4.4c exhibits its EELS mapping. Carbon, boron, nitrogen, and sulfur signal are distinct from each other. The most inner C signal represents SWCNT. The most outer sulfur signal represents MoS_2 nanotube, and the middle boron, nitrogen signal represents BNNT.

In the ED pattern, each pattern can be distinguished from each other. The yellow one is from MoS_2 NT, and the inner green, blue, and red one from SWCNT and BNNT. It clearly shows that this ternary coaxial structure is continuous and highly crystallized.

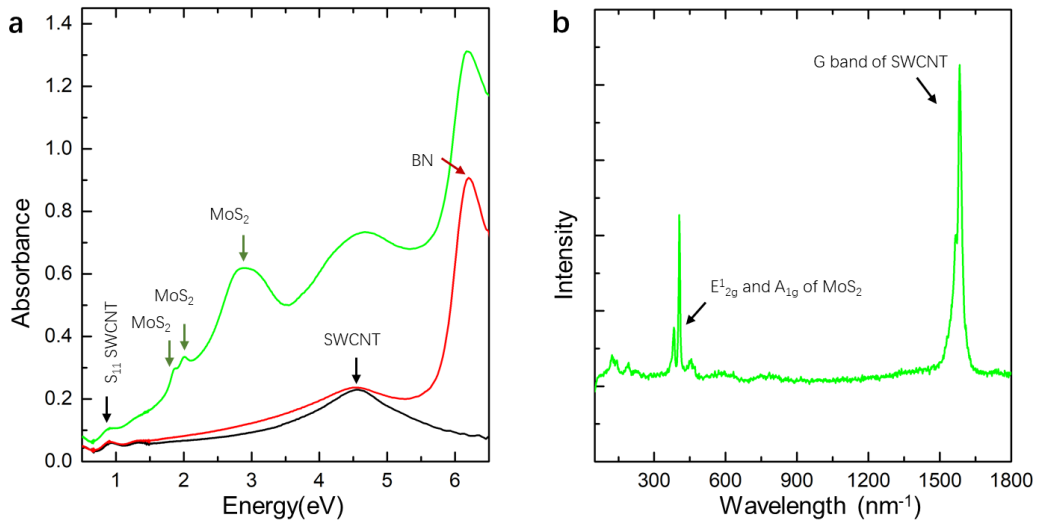

Figure 4.5 (a) Absorption spectra of pristine SWCNT, SWCNT-BNNT, and SWCNT-BNNT-MoS_2 nanotube. (b) Raman spectrum of SWCNT-BNNT-MoS_2 nanotube.

We also checked the optical spectrum for this ternary structure. In their absorbance results (Fig 4.5a), different integrant can be distinguished by their characteristic peaks. The green curve for SWCNT-BNNT-MoS_2 nanotube has three characteristic peaks for MoS_2 at ~1.9 eV and ~2.1 eV, and a broad peak at ~2.9 eV. We attribute the first two peaks to optical absorption by band-edge excitons and the third peak to absorption by excitons associated with the van Hove singularity of MoS_2 [103]. As for the Raman spectrum, E^1_{2g} and A_{1g} modes of 2D MoS_2 can be observed (Fig 4.5b).

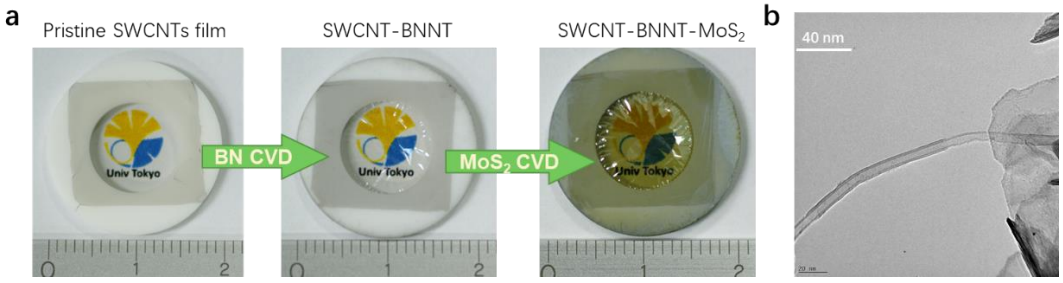

Figure 4.6 (a) Photographs of suspended SWCNT after BN CVD and MoS_2 CVD. (b) A SWCNT-BNNT-MoS_2 nanotube with MoS_2 flake together in one TEM image.

We also took some photographs for these suspended film after CVD process (Fig 4.6a). After BN CVD, the film still keeps transparent but a little reflective. After MoS_2 CVD, the film turns a little darker, but still complete and transparent. The dark film in this optical image seems to show that the yield of MoS_2 nanotube is very high, but in fact it is not case.

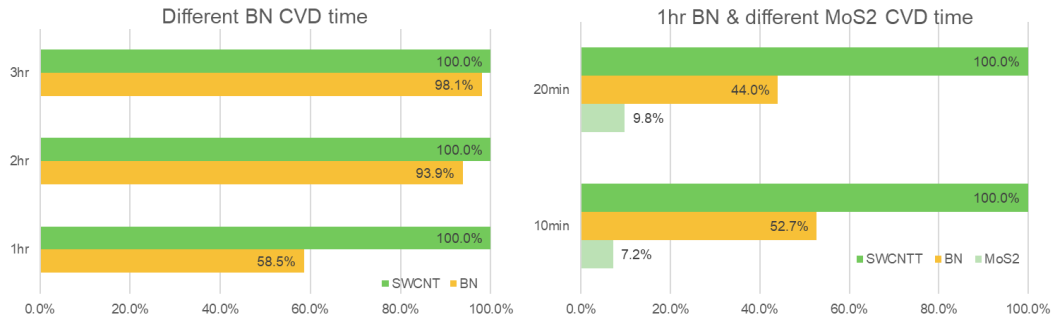

Figure 4.7 Two charts for coverage of BNNTs and MoS_2 nanotubes with different CVD duration.

We did a survey on the yield of BNNTs and MoS_2 nanotubes, respectively (see Fig 4.7). Only individual nanotubes were calculated. The left chart is the evolution of BNNT coverage depending on CVD duration. The statistical result reveals that over 50% SWCNTs were covered with BNNT by 1-hour CVD duration, and the coverage reached to over 90% when duration time increased to 2 hours. An almost fully BNNT covered SWCNT can be finally obtained by 3-hours BN CVD process.

The chart on the right is the statistical result for MoS_2 nanotubes. 1-hour BN CVD has been conducted before MoS_2 CVD was performed. The result exhibits that MoS_2 nanotube yielded no more than 10% with 20 min CVD duration, of which the coverage is much lower than that of BNNT. Fig 4.6b shows a TEM result of such ternary nanotube. We learn that some of MoS_2 were formed as flakes rather than tube-structure at the nanotube junctions. This is why the as-prepared suspended nanotube looks dark but in fact the yield of MoS_2 nanotube is still very low.

Chapter 5: Growth mechanism

Details of formation for 1D vdW heterostructures are still not fully understood so far. In this paper, an investigation into growth mechanism, structure matching will be presented in detail. In addition, we have also proved that density of nucleation sites plays a pivotal role in hetero-nanotubes synthesis, followed by two methods of patterned growth to demonstrate their relevance. This work will help us gain a much better understanding of 1D vdW heterostructures, which is important for developing a broader range of application.

5.1 Open−end growth mode

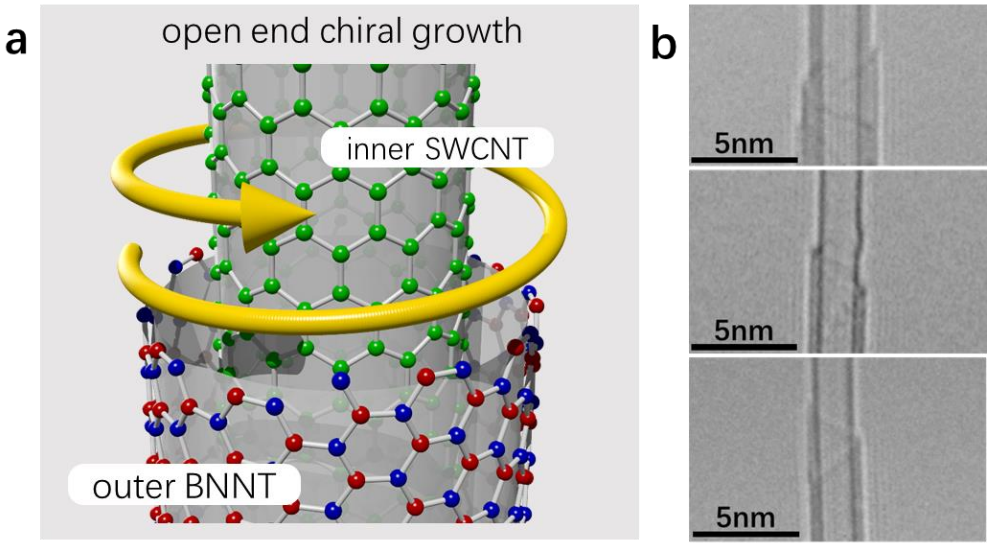

Fig. 5.1 (a) Atomic model of open-end growth mechanism. Green, blue, and red spheres represent for carbon, boron, and nitrogen atoms, respectively. (b) Three examples for tube end of SWCNT-BNNT.

To start with, growth mechanism will be discussed in this chapter first. We proposed a growth mechanism in terms of open-end growth model, which is assumed to be the main formation of SWCNT-BNNT heterostructures. Figure 5.1a gives an atomic growth model of this heterostructures with an inner SWCNT along with an outer BNNT. The SWCNT is considered as a 1D template, and BNNT is grown afterwards. As a result, BNNT extends from the open-edge with continuous feeding of BN sources,

analogous to epitaxial growth of h-BN in 2D space. The BN formation gradually goes with the yellow arrow in an upward spiral direction that ensures single crystals in good quality. It should be noted that the whole process of BN formation does not require any catalysts at all, which is quite different from the previous 1D materials studies in synthesis. Speaking of 1D materials, its growth rate is in general much faster compared to 2D materials thanks to the catalysts. This mechanism of open-end chiral growth in 1D heterostructure is, after all, a catalyst-free process, resulting in very slow growth rates at only few hundreds nm per hour. Figure 5.1b shows some examples for tube end of SWCNT-BNNT sample. We can see these tube end shows obvious spiral shape.

5.2 Effect of isolation

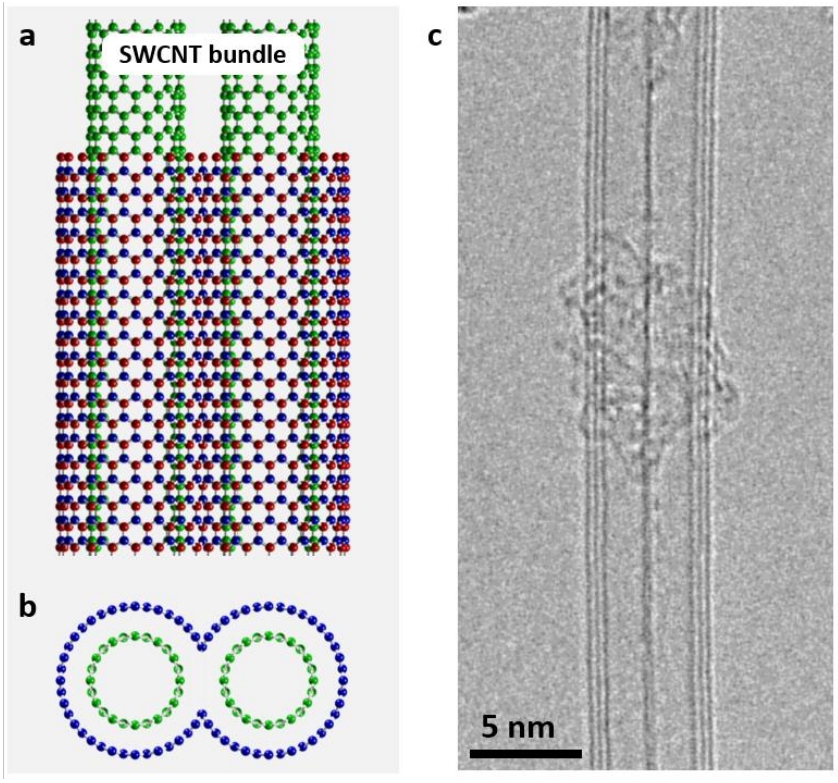

Figure 5.2 (a) Atomic model of a BN coated bundle consisting of two SWCNT, and (b) its cross-section view. (c) TEM image for this bundle situation.

To obtain a 1D vdW heterostructure with such high crystalline quality, it is necessary to figure out the factors that influences nanotube surface. The formation of 1D vdW heterostructure is a post growth process. A nicely formed hetero nanotube with good crystallinity demands for a continuous surface of inner nanotube. Here, two situations are given for a binary vdW heterostructure of SWTN and BNNT.

Figure 5.2a shows one situation with a simple atomic model, in which carbon, boron and nitrogen atoms are marked by green, blue, and red, respectively. It gives a typical situation that two SWCNTs cling to each other and form bundles. BN layers, the same as unbent h-BN, will be grown on the tube surface after we perform BN CVD. Instead of separating the bundles into two individual SWCNTs, it is quite interesting BN layers just go across the groove of the bundles and wrap around the outside surface. As a result, BN layers become a peanut-shaped structure in cross-section of the atomic model (Figure 2b). TEM image in Figure 2c shows a bundle consisting of two SWCNTs wrapped by two layers of BN. The spacing between BN layers is approximately 0.34

nm on both sides, while two SWCNTs still stick to each other all along during the whole BN CVD process, which gives no way for BN layers to get inside.

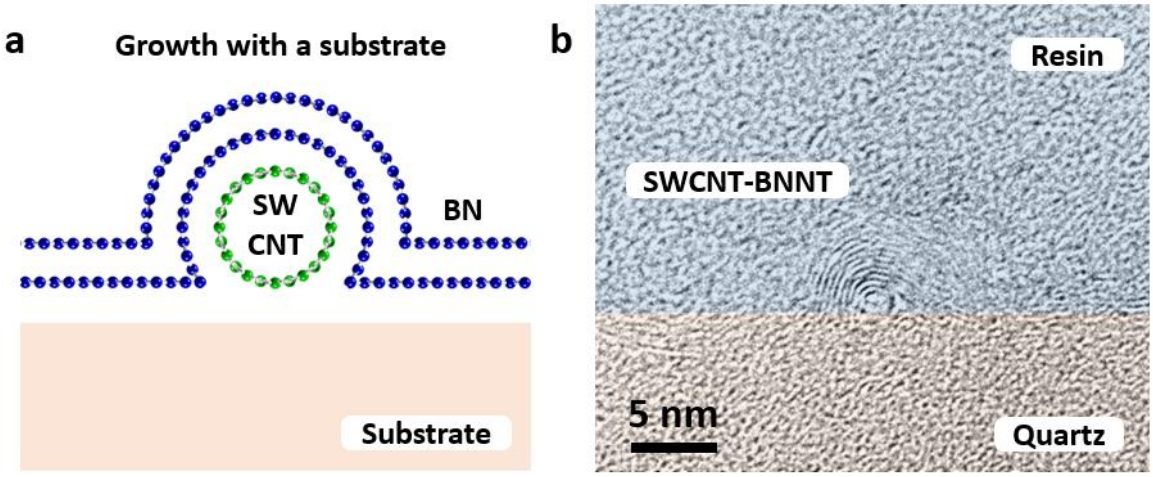

Figure 5.3 (a) Atomic model of a BN coated bundle SWCNT on a plat substrate as the second situation. (b) Specimen based on the second situation made by a Focused-ion-beam (FIB) system for TEM characterization.

Figure 5.3a shows another simple atomic model with a SWCNT fixed on a flat substrate, which is a common situation in CNT-related experiments of growth and characterization. After BN CVD is conducted, BN layers can only be formed on the upper part of the SWCNT surface, leaving the bottom part firmly fixed on the substrate without any BN layers in between. Based on this situation, we prepared a specimen using a FIB system for TEM characterization (Figure 5.3b). To start with, SWCNTs were initially grown on a quartz substrate in horizontal direction and then coated with BN layers by BN CVD process. The sample was then resin-embedded. After that, the ion milling control programs were used to generate the cross-section profile. Figure 2e shows a cross-section view of the as-prepared specimen under TEM observation. Resin and quartz substrate are coloured by blue and orange respectively with a better contrast. In the resin part, an approximate concentric circle with over 10 layers can be seen from the TEM image, which consists of one SWCNT and plenty of BN layers wrapped around. The innermost closed circle should be SWCNTs while the outer layers just partly disappeared below the boundary in quartz part. This result is similar to the former one as the BN layers are not able not form a closed circle in tubular structures. As two situations mentioned above, a better way of getting a nicely formed hetero nanotube with good crystallinity is to avoid bundles of nanotubes and no usage of flat substrate

served as support. To put it another way, a SWCNT, as an example, need to be isolated and suspended for a better hetero-nanotubes synthesis.

5.3 Effect of cleanness

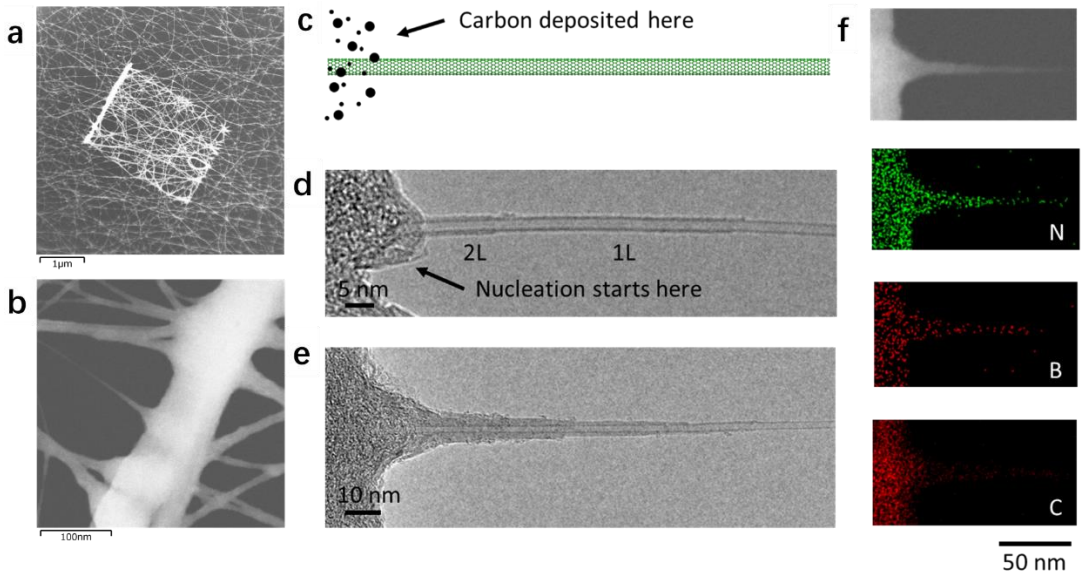

Figure 5.4 (a) SEM image of SWCNT film after E-beam exposure with an obvious rectangle-shaped area that has the same size as the observing window in SEM. (b) higher magnification of an exposed area. (c) Atomic model for nucleation sites of amorphous carbon on a SWCNT. (d) BN as outer layer was grown from a nucleation site. (e) Thicker layer of outer BN compared to other area, and its (f) EDS mapping of nitrogen, boron, and carbon.

Now that we proposed an open-end chiral growth mechanism, we have also developed a nucleation site control method: Electron pattering.

As is well known, E-beam exposure produces amorphous carbon deposited on the surface of samples [104]. Take CNTs as an example, high current density in electron microscope will result in contamination of a thin layer of amorphous carbon coating on CNTs surface during SEM characterization, as shown in Fig 5.4a&b. In our experiment, most of this amorphous carbon will be etched by hydrogen during at high temperature, but a few of them will be left on the surface as illustrated in Fig 5.4c. The remaining amorphous carbon makes an “uncleaned” surface of CNTs, acting as a great deal of nucleation sites for BNNT growth as shown in Fig 5.4d. Fig 5.4e is one of the nucleation site coated area with grown BNNT. The outer BNNT has greater thickness compared to other area in the same sample, which means the growth of outer BNNT benefits from

amorphous carbon as nucleation sites. EDS mapping in Fig 5.4f also reveals that the outer layer belongs to BN rather than amorphous carbon itself.

5.4 Three different growth models

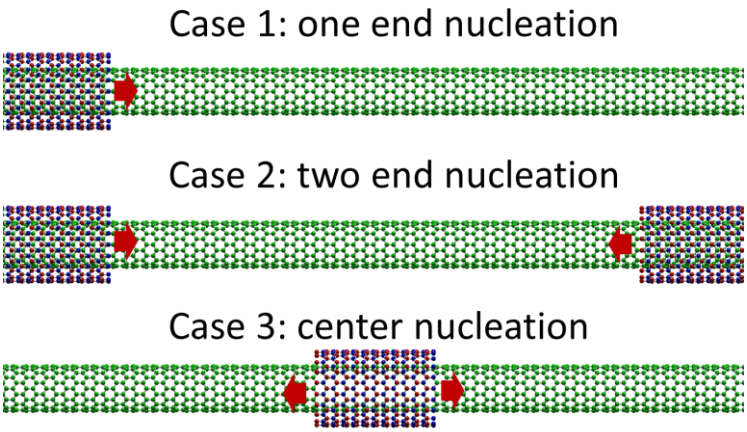

Figure 5.4 Atomic 3D model for three cases refers to open-end chiral growth

We also noted that three kinds of growth models occurred in this scenario for the open-end chiral growth. Case 1 in Figure 5.4 is an atomic model that BNNT grows from one end nucleation, while in Case 2, BNNT grows from both ends by two ends nucleation. Case 3 is a model in which center nucleation of BNNT rarely occurred in the middle. These three models can all be observed by TEM images in each area of a SWCNT-BNNT samples.

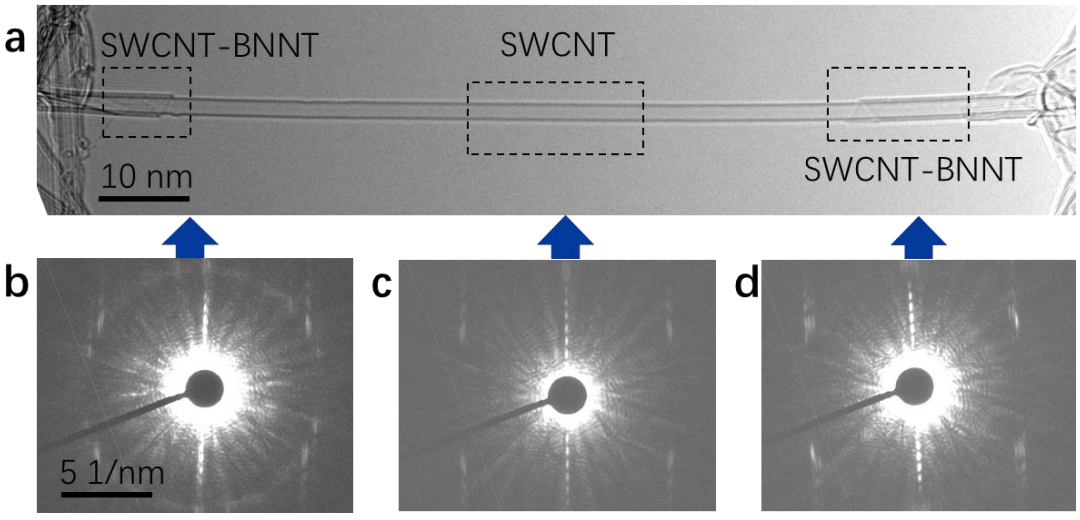

Figure 5.5 (a) TEM image as an example for case 2, in which BNNT growth starts from both ends. (b)-(d) Three ED patterns for different areas on the same nanotubes.

Fig 5.5a shows an isolated nanotube with 260 nm length under TEM observation. Three dashed rectangle areas were marked with different nanotubes. The areas on both ends marked as “SWCNT-BNNT” are obviously different from the middle area marked as “SWCNT”. This is because the nanotube in “SWCNT-BNNT” is one wall of BNNT thicker than that in “SWCNT”. Evidently, BNNT growth starts from both ends of this SWCNT for a short distance, leaving the SWCNT with a bare surface in the center part. This TEM result is in accordance with Case 2 in the scenario for the open-end chiral growth. Fig 5.5d-f show three ED patterns successively corresponding to three dashed rectangle areas in Fig 5.5a from left to right. By comparing three ED patterns with each other, it clearly reveals that one more ED pattern was appeared on both sides of the SWCNT, which means the additional patterns belong to grown BNNT as outer layer.

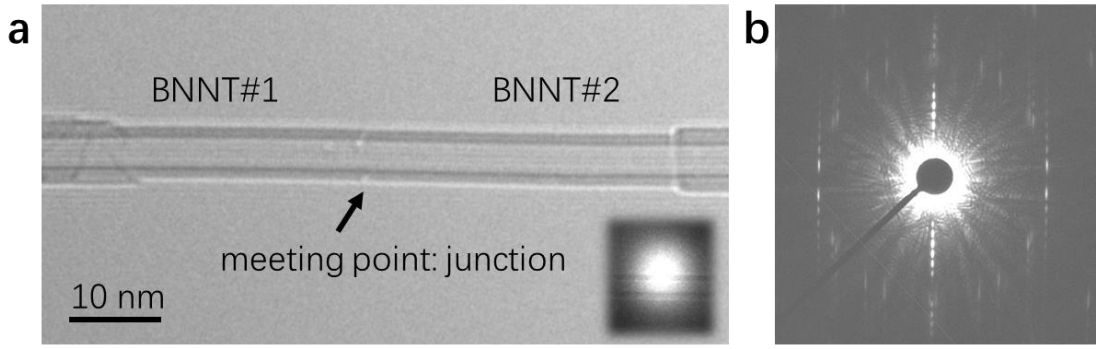

Figure 5.6 (a) Fully BNNT wrapped SWCNT refers to case 2 of open-end chiral growth. (b) ED pattern taken from the “melted” point of a SWCNT-BNNT heterostructure.

Moreover, another TEM image shown in Fig 5.6a also depicts the same model in Case 2. The SWNT is fully wrapped by BNNT, but a meeting point as junction is observed in the center this time. Meanwhile, the wall numbers are decreasing from both ends to the middle, so it is not difficult to imagine that this “complete” BNNT in outer layer was grown from two sides then finally met each other. A nano-area ED pattern was taken at the meeting point (Fig 5.6b). Besides the original one set of hexagonal patterns in SWCNT, two sets in BNNT can be observed as expected, exemplifying the property of open-end growth in Case 2. Last but not least, it is important to note that most of the edges of BNNTs ended in spirals, and equicrural triangle formed (Fig 5.5a

& Fig5.6a). This specific spiral angle as well indicates the chiral growth in our model as mentioned in section 5.1.

Chapter 6: Structure analysis

Now that we have a general characterization for 1D vdW heterostructures and some basic understanding for the growth mechanism. We also want to know if there is any structural relationship between each layer. In this chapter, discussion about epitaxial and handedness relationship will be given.

6.1 SWCNT-BNNT chiral angle analysis

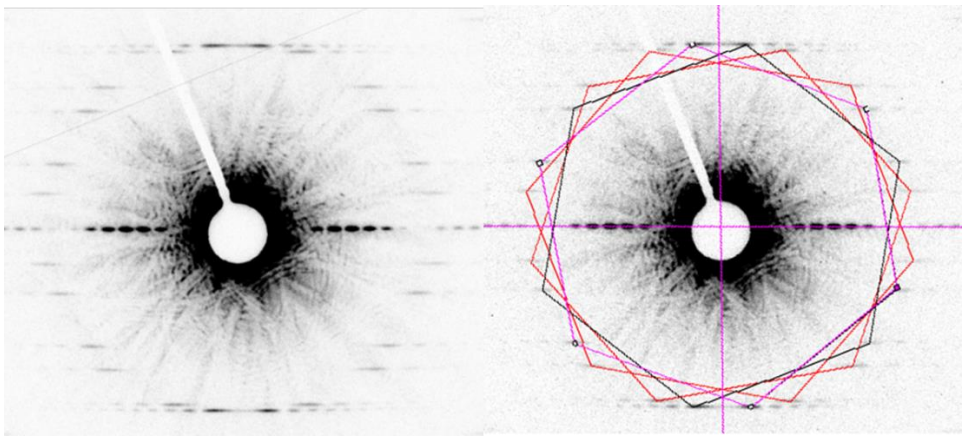

Figure 6.1 (a) Given ED pattern of SWCNT-BNNT sample, and then (b) marked with hexagonal geometry for further measurement.

For simple structure, such as SWCNTs, the structure can be determined uniquely by ED pattern. To measure chirality from the ED pattern, Figure 6.1 is considered. A given ED pattern of a multi-walled nanotubes can be denoted as numbers of hexagons in central symmetry. Each pair of two hexagons is regarded as a combination of two ED patterns of graphene. Since a SWCNT can be considered as two symmetric graphene laminated together, it always shows two sets of hexagons in ED pattern. With structural distortion as a tubular structure, each point will be stretch in horizontal direction.

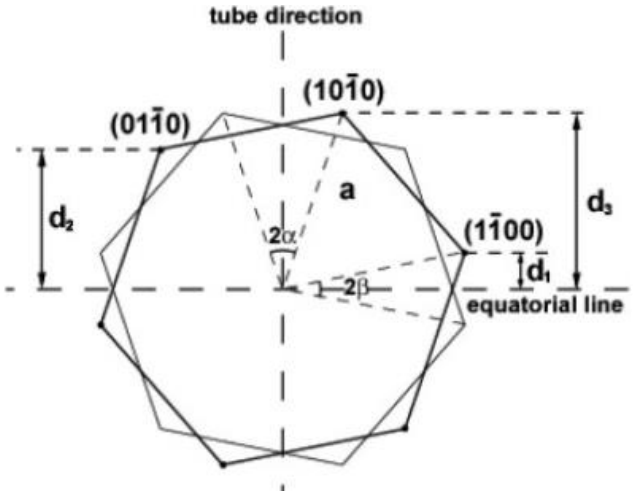

Figure 6.2 Distances denoted as d_1, d_2, and d_3, and chiral angel denoted as α. Reproduced from [105], Copyright (2004), with permission from John Wiley and Sons.

Fig 6.2 elaborates the measurement and calculation method for chirality determination. The distances can be measured precisely from the given patterns. Relationships between d_1, d_2, d_3, β, and α are described as:

$$d_1 + d_2 = d_3$$

$$\alpha = \tan^{-1}\left(\frac{1}{\sqrt{3}} \cdot \frac{d_2 - d_1}{d_3}\right) = \tan^{-1}\left(\frac{1}{\sqrt{3}} \cdot \frac{2d_2 - d_3}{d_3}\right)$$

$$\text{or } \beta = \tan^{-1}\left(\sqrt{3} \cdot \frac{d_1}{d_2 + d_3}\right) = \tan^{-1}\left(\sqrt{3} \cdot \frac{d_3 - d_2}{d_2 + d_3}\right)$$

With the as-calculated chiral angle α, the chiral indices (n, m) of nanotubes can be determined by chiral data index.

As we known in CVD-grown 2D vdW heterostructures, the growth layer is usually aligned with the base material, but the question that if 1D vdW heterostructures have such tendency remains mysterious. This aligned relationship is called epitaxial relationship. Measuring a given ED pattern is one of the effective ways to assign the chirality of a nanotube.

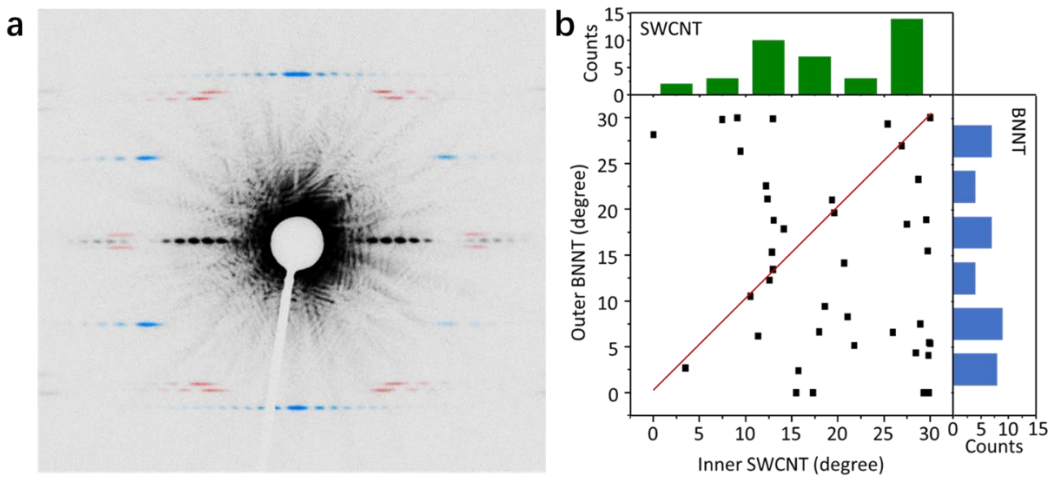

Figure 6.3 (a) ED pattern of a SWCNT-BNNT sample. Red: SWCNT. Blue: BNNT. (b) Statistical plot of chiral angle of inner SWCNT versus the outer BNNT for SWCNT-BNNT, revealing that as-grown SWCNTs were enriched in the near-armchair form but that the outer BNNT was evenly distributed [106].

Using the above calculation methods, the chirality of nanotube can be determined by given ED patterns. We did a survey on a large number of SWCNTs and binary nanotubes with SWCNT and BNNT. Fig 6.3a is one example for SWCNT-BNNT with distinct ED patterns. The lattice mismatch of graphene with hexagonal boron nitride is about 1.8%, so it is not difficult to distinguish their ED patterns from each other. Inner SWCNT is coloured by red, and Outer BNNT is coloured by blue.

Statistical result is shown in Fig 6.3b. The x axis is the chiral degree for inner SWCNT, and the y axis represents for chiral angle of outer BNNT. We found that most of SWCNTs were in near armchair form. However, the outer BNNTs were randomly distributed. No chiral angle dependence was observed. In 2D vdW heterostructures, the growth layer is usually aligned to the base materials, while in this 1D vdW, there is no such tendency.

6.2 SWCNT-BNNT handedness analysis

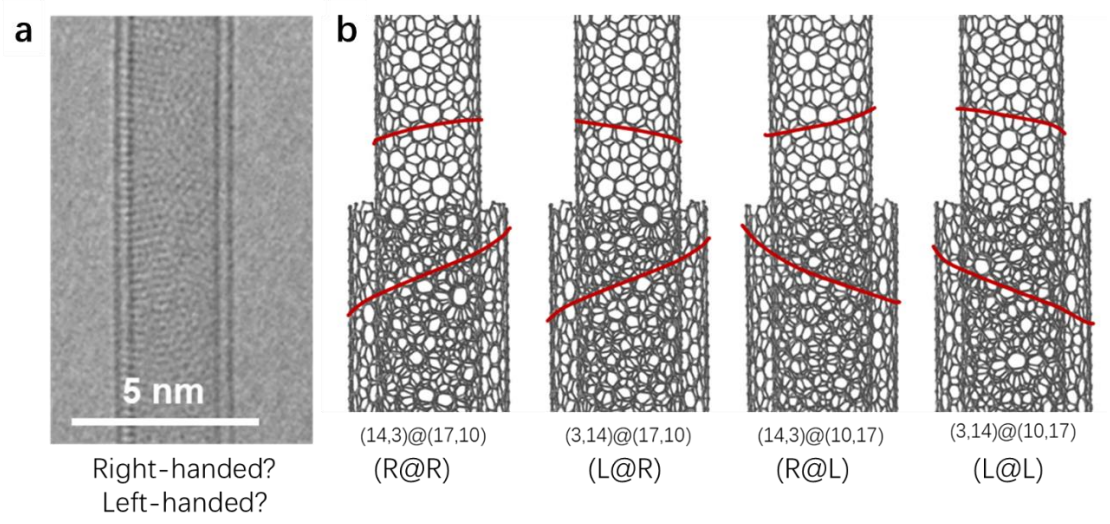

Figure 6.4 (a) Double-walled SWCNT-BNNT nanotube with known chiral indices of (26, 5) and (30, 10) but unknown handedness. (b) Atomic f four possible handedness relationship with given indices.

Now that we know there is no epitaxial relationship between each layer, but the handedness relationship between inner and outer layers remains a question. Handedness is also an important property for optical devices, which could function with a circularly polarized light. However, the handedness determination is much more difficult than chirality determination, because the ED pattern of hexagonal nanotube is a central geometry.

Fig 6.4a is a double-walled SWCNT-BNNT nanotube. By calculating ED pattern, inner SWCNT is assigned as (26, 5), and outer BNNT as (30, 10). However, its handedness can not be determined by ED pattern itself. In Fig 6.4b, a chirality given double-walled nanotube could have 4 possible handedness relationship: right-handed with right-handed, left-handed with right-handed, right-handed with left-handed, and left-handed with left-handed. All 4 possible combination own the same hexagonal geometry in ED pattern.

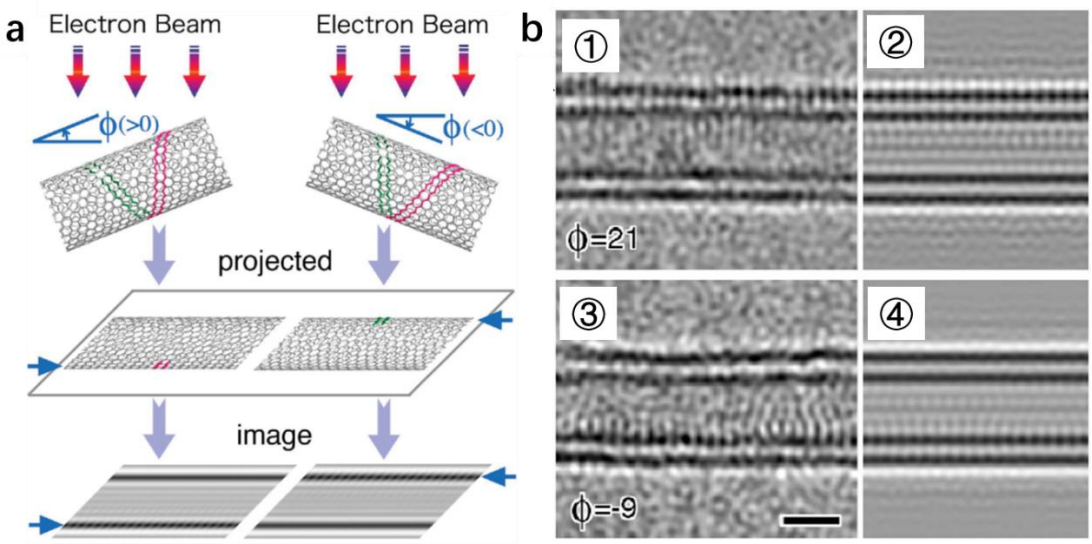

Figure 6.5 (a) Schematic sketch for the analysis method. When tilting angle Φ at a certain degree, asymmetric lattice fringes appear at either side of tube surface under incident electron beam. Two sets of zigzag chains are shown in red and green, corresponding to those on the front and back surfaces, respectively. (b) Two HREM images of a double-walled nanotube acquired with a tilting angle (①③), and two corresponding simulated images (②④). The scale bar is l nm. Reproduced from [107], Copyright (2005), with permission from APS physics.

A recent research focusing on double-walled CNTs proposed an analysis method. By tilting the sample in different angle, the nanotube will show lattice fringes on either side under incident electron beam. These fringes information can further determine their handedness, as shown in Fig 6,5a.

Fig 6.5b is an example for this analysis method at [107]. By tilting the nanotube, the lattice fringes appear on the upper wall of the outer nanotube. When nanotube at opposite tilting angle, the lattice fringes appear again on the lower wall of the inner nanotube. This means inner and outer CNT has the opposite handedness.

No.	Inner SWCNT	Outer BNNTs			
1	L	R			
2	L	L			
3	Z	L	L		
4	R	R	R		
5	Z	R	R		
6	L	R	R		
7	R	R			
8	R	R	R	R	R
9	L	L	L		
10	Z	Z			
11	R	R	R		
12	L	L			
13	L	L	L		
14	L	L	R	R	
15	Z	L	L		
16	L	L			
17	L	L	L		
18	L	L			
19	A	R	R		
20	Z	R	R	A	

Table I. A summary of the handedness measurements of the 20 binary heterostructures in SWCNT-BNNT. (R: right-handed, L: left-handed, Z: near-zigzag, A: near armchair.) Due to the technical limitation of TEM apparatus, some of the nanotubes have unidentified layer, and are excluded from this table.

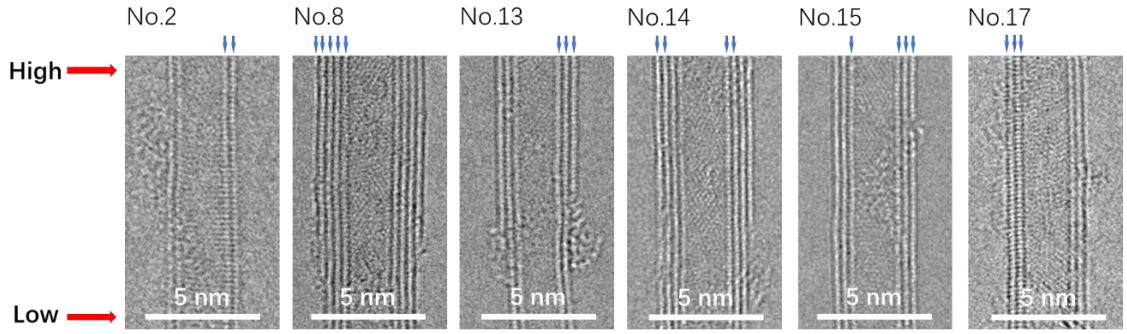

Figure 6.6 Several examples of TEM images of SWCNT-BNNT acquired with an inclination angles (top side is higher) in Table I. The layers with fringes are indicated by blue arrows.

In our experiment, the handedness relationship between inner SWCNT and outer BNNT have been investigated by TEM. Table I summarized our measurements of the handedness of 20 binary nanotubes in SWCNT-BNNT. Not all the handedness of nanotubes can be determined because of the limitation in resolution of TEM apparatus. Some of the TEM images with clear fringes are shown in Fig.6.6. As shown in Table I, the right- and left-handed nanotubes are not equally distributed for inner SWCNTs. The results prove that some formation of handedness might occur during the SWCNTs growth.

First interlayer		Following interlayers	
same	different	same	different
15	7	17	2
68.2%	31.8%	89.5%	10.5%

Table II. A summary of all interlayers with same or different handedness in Table I. "First interlayer" represents interlayer between the innermost SWCNT and the second BNNT. "Following interlayers" represents all interlayers between the following BNNTs from the third BNNT to the outermost.

Table II summarized all the interlayers in different situation. As for the innermost interlayer, which all belong to CNT-BNNT interlayer, 15 nanotubes with same handedness and 7 nanotubes with mixed handedness were found. On the other hand, 17

nanotubes with same handedness only 2 mixed interlayers were found in the following interlayers, and the ratio of the same handedness increased from 68.2% to 89.5%, which suggests that there is a relatively high tendency of the same handedness for the outer interlayers.

We have two assumptions for this result. Firstly, the outer interlayers are all homo-structure (BNNT-BNNT), no heterostructure anymore, so they are easier to align to each other. Secondly, in a previous research, the relationship between the interfacial energy and the bending energy for SWCNT-BNNT have been discussed [102]. As we know, the outer BN has smaller curvature. In large diameter range, interfacial energy has almost the same order of magnitude of bending energy due to the weaker bending effect, and the bending energy is no longer the leading factor in the formation of outer layers. When bending energy become relatively lower, the interfacial energy should be considered as well. This may result in a higher tendency of the same handedness for the outer interlayers that owns larger diameter.

Chapter 7: Properties of 1D heterostructures

The high quality of 1D heterostructures allow for the experimental exploration of properties. So far, we have already finished some preliminary experiments on properties of as-prepared 1D heterostructures. Some of the experiments were done with other collaborative groups.

7.1 Thermal property

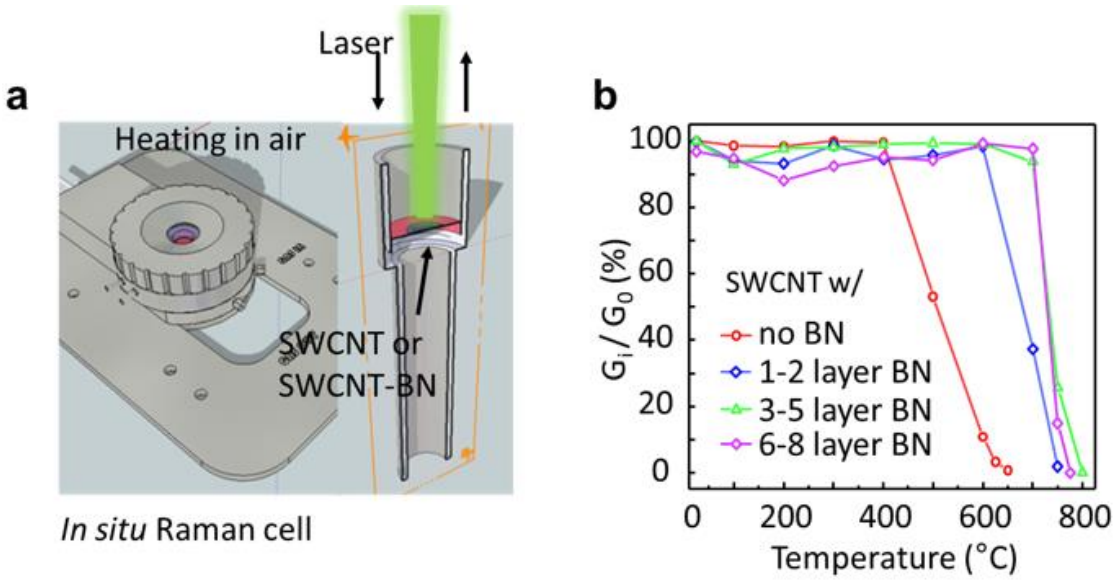

Figure 7.1 (a) Schematic illustration of an in-situ Raman cell for real-time Raman characterization. Different kinds of atmosphere can be applied as needed. (b) Evolution of thermal stability of pristine SWCNT and SWCNT-BNNT heterostructures with different number of BN layers.

As for the thermal properties, the outer BN layers can be considered as a protective layer, which can protect the inner SWCNTs against oxidation. With more BN layers outside, SWCNT can bear higher temperature in air. We collaborated with J. Guo and Y. Li from Peking University on this experiment. Fig 7.1a is a schematic illustration of an in-situ Raman cell. The sample is encapsulated in the small cell, and incident laser comes from above and get to the sample through quartz glass. Different kinds of atmosphere can be applied as needed, such as N_2, Ar, and air. In this experiment, we introduced air into the Raman cell to see how sample behaved at different temperature.

In Fig 7,1, G_o and G_i represents for G band intensity before and after high temperature, respectively. The ratio of G_i and G_o gives the relative loss of SWCNTs due to oxidation. When temperature raised up to 400°C, G_i/G_o ratio didn't change, which agrees with the original thermal property of SWCNT, but G_i/G_o ratio started to decrease for pristine SWCNTs sample when temperature was over 400°C. However, with 1-2 layers BN coated, the decreasing point G_i/G_o ratio increased to over 600°C. Furthermore, the decreasing point can reach to over 700°C when 6-8 layers of BN were coated on SWCNTs. In conclusion, the burning temperature of inner SWCNT can reach to 700°C in air, while the naked SWCNTs started to burn at only 400°C.

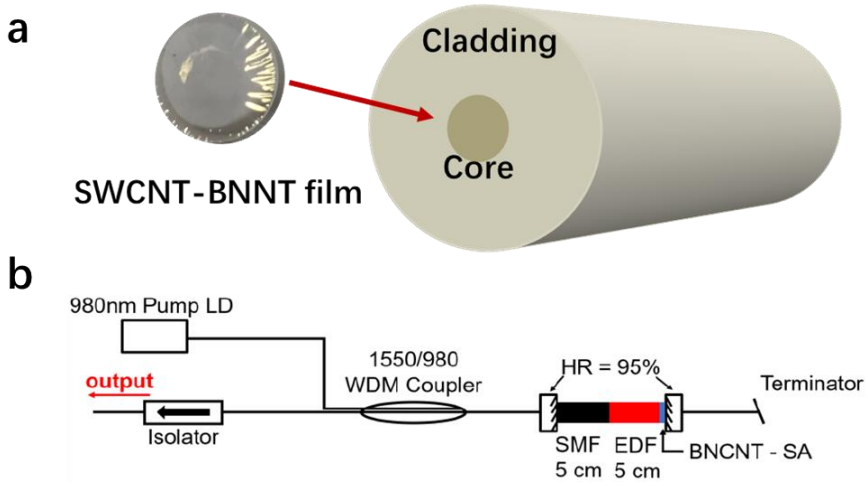

Figure 7.3 (a) Schematic illustration of transferring a SWCNT-BNNT film on an optical fiber. (b) Fiber laser experimental setup that consists of a 10-cm-long fiber and two 95% 1550-nm-HR coated fiber-ferrule mirrors. SWCNT-BNNT film is sandwiched between the fiber ferrule and mirror. [108]

Another experiment related heat resistance is collaborated with P. Yuan at Yamashita's group. SWCNT is an excellent saturable absorber and plays an crucial role in mode-locked lasers [109]. However, SWCNT have a rather low optical damage threshold about 10 mW. In our experiment, BNNT was grown to coat SWCNT by CVD as a protective layer and then transferred onto a single-mode fiber (as shown in Fig 7.3a). The experiment setup is shown in Fig 7.3b. The outer BNNT provides a significantly higher thermal stability and increases the optical damage threshold of SWCNT to 5 times. Also, there is no overall changes in optical transmission characteristics with outer BN layers.

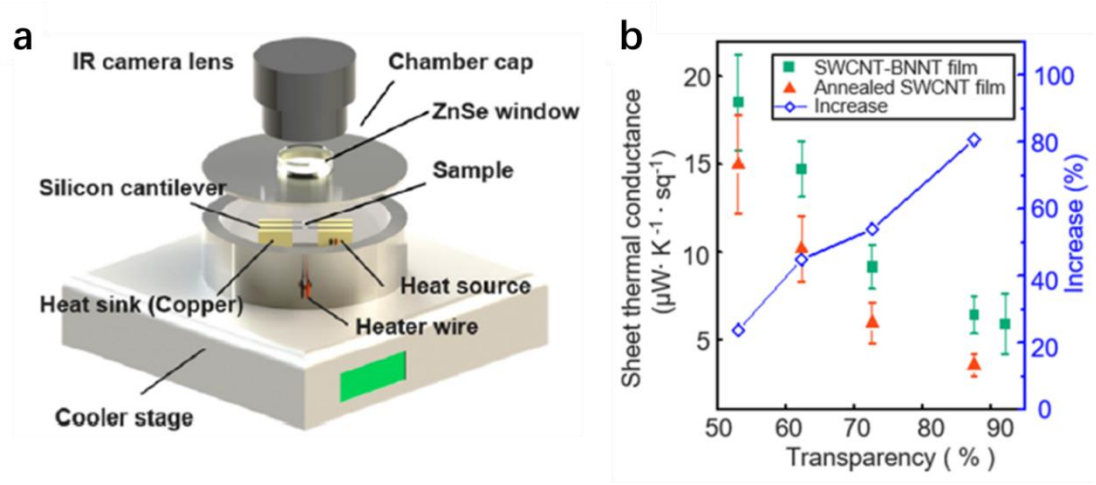

Figure 7.2 (a) Schematic illustration of the experimental setup for the thermal conductance measurement. The heat source and heat sink are deployed with resultant a temperature drop. When the heat transferred through the sample and reached a steady-state, the temperature profiles will be recorded by the IR thermal imager from the top side. (b) Evolution of sheet thermal conductance of SWCNT−BNNT films and annealed SWCNT films. The blue line with hollow rhombuses represents the increase ratio of the sheet thermal conductance after BNNT coating process. Reproduced from [110], Copyright (2020), with permission from ACS.

Besides, it is also confirmed that there is an enhancement in sheet thermal conductance with the help of outer BNNTs. This experimented was collaborated with our lab member P. Wang. Fig 7.2a is the experimental setup for the thermal conductance measurement. SWCNT-BNNT sample was fixed between heat source and heat sink. Heat transport was recorded by the IR thermal imager during the measurement. Fig 7.2b reveals the sheet thermal conductance values depending on transparency. An enhancement of thermal conductance is confirmed as the BNNT was acting as additional thermal transport channels. The degree of enhancement increase with the transparency, which is plotted in blue curve with right axis. Especially for SWCNT with 92% transparency, the increase in thermal conductance reached to 93% with the help of 3 hours BN CVD process.

Researches related to thermal properties above provide information for tailoring materials in 1D heterostructures. The effective heat resistance as well as the enhanced

thermal conductance makes them a promising building block for thermal and optoelectronic applications in the future.

7.2 Optical properties

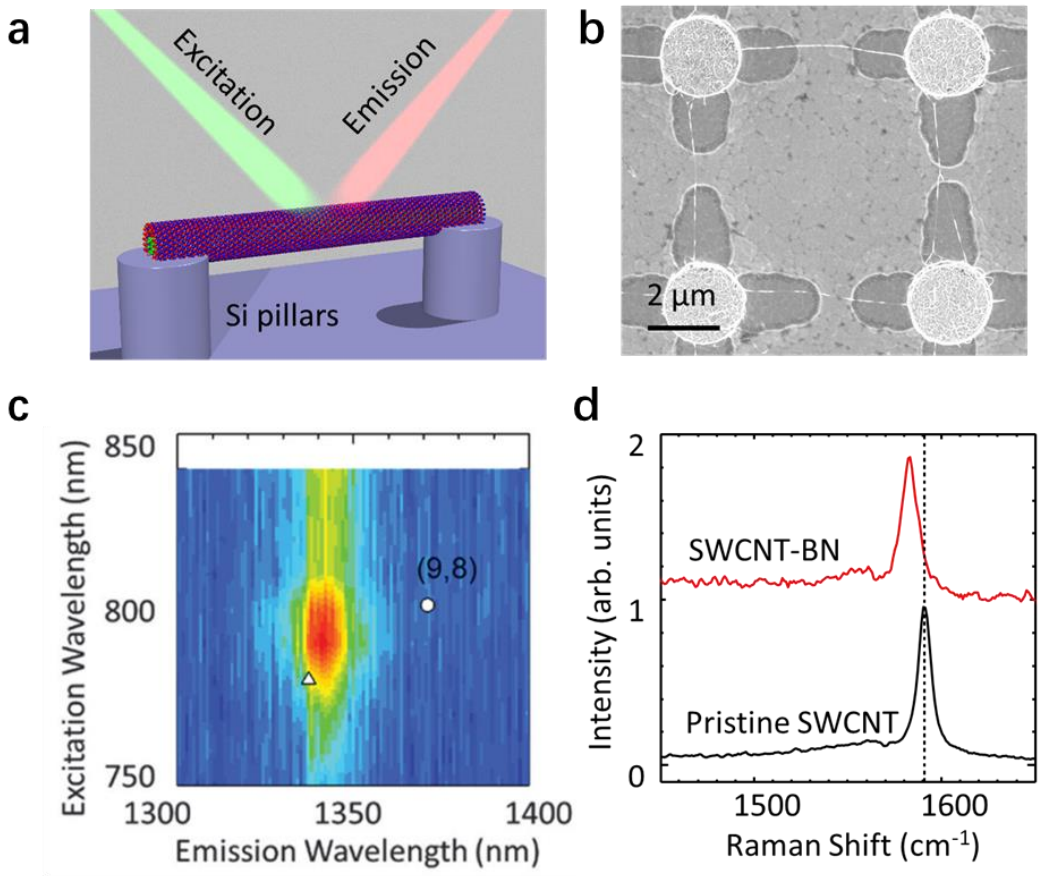

Figure 7.4 (a) Schematic illustration of a suspended SWCNT-BNNT nanotube with excitation and emission process. (b) SEM image of suspended SWCNT-BNNT nanotube on Si pillars. (c) PL excitation-emission map of suspended SWCNT-BNNT, in which circle and triangle marks represents the optical transition energy in ambient atmosphere and vacuum, respectively. (d) Raman spectra of an individual SWCNT before and after BN coating.

As for the optical properties, Raman and Photoluminescence spectra show that their structure integrity was preserved. Fig 7.4a&b are schematic illustration and SEM image of a suspended SWCNT-BNNT on Si pillars, respectively. The suspended SWCNTs were prepared by alcohol catalytic chemical vapor deposition (ACCVD) [111]. Fig 7.4&b are PL excitation-emission map and Raman spectra of suspended SWCNT-BNNT, respectively. They both showed typical peaks of pristine SWCNTs, which means the structural integrity of inner SWCNT was preserved. As for Raman

spectra, a G band downshift of 5 to 10 cm^{-1} appeared. This small downshift may result from the thermal strain between SWCNT and BNNT during high-temperature CVD. It can also be regarded as a fingerprint whether BNNT coating is successful or not.

7.3 Electronic device

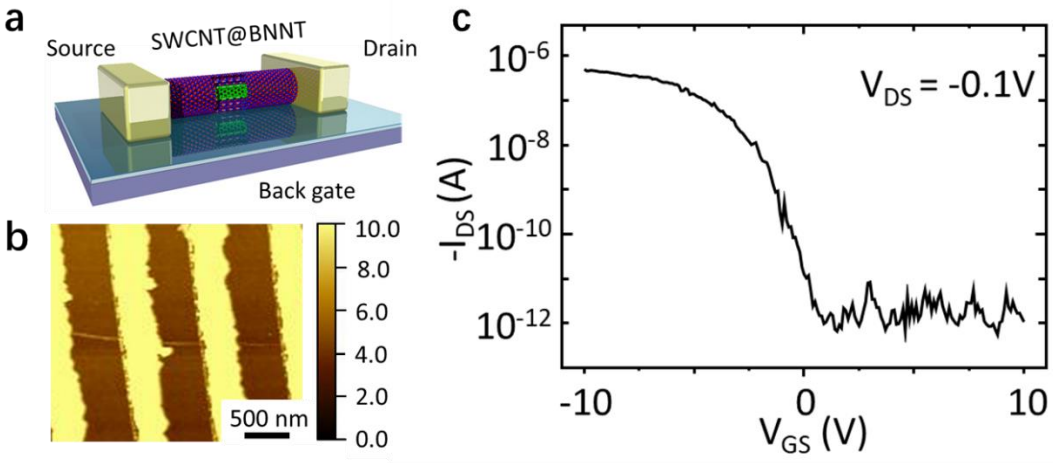

Figure 7.5 (a) Schematic, (b) AFM image, and (c) characteristic transfer curve (F) of a back-gated FET built on a SWCNT-BNNT. I_{DS}, drain current; V_{GS}, gate voltage; V_{DS}, drain voltage.

As for the electronic properties, the BN coating did not change the intrinsic electronic transport of the inner SWCNT. In this experiments, suspended SWCNT-BNNT heterostructures were first synthesized on Si array, and then transferred onto a Si substrate. Fig 7.5b is an AFM image after transfer. As most of the as-prepared SWCNTs were grown on top on Si array, the post-transfer SWCNTs displayed like paralleled lines (faint yellow). Only a few nanotubes went across from each other. Device was made based on these individual nanotubes.

Fig 7.5a is a 3D model for a back-gated FET based on SWCNT-BNNT heterostructures. Its performance is similar to a SWCNT FET and had an ON/OFF ratio of 10^{-5}, which means the high quality of SWCNT is kept (characteristic transfer curve is shown in Fig 7.5c).

7.4 In situ TEM measurement

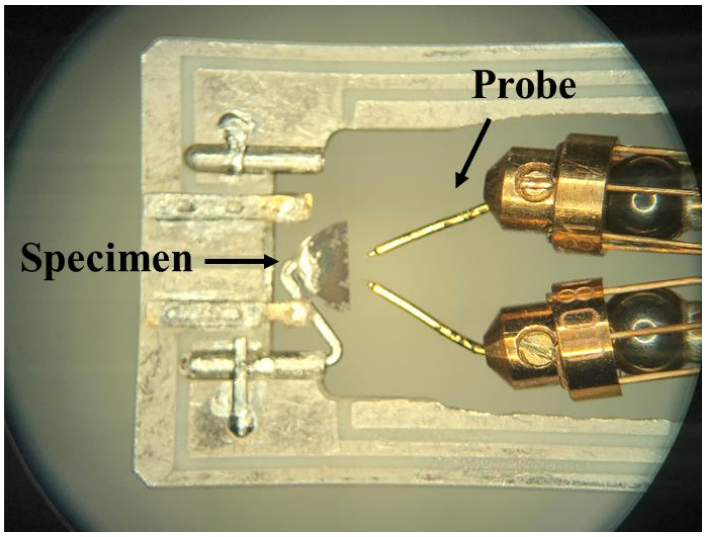

Figure 7.6 Photograph of an in-situ TEM Nano-manipulator sample holder with two piezo-controlled metallic nanoscale electrical probes.

To further investigate the tunneling effect of 1D heterostructures, we need to use an in situ TEM measurement, which I think is the most difficult part, because such experiments demand for manipulation of individual nanotube with nanoscale resolution. The device, called TEM sample holder, in Fig 7.6 composes of in-situ TEM measurement. It is used inside a TEM to do manipulation of nanomaterials and imaging at the same time. With the help of two probes, imaging and resistance measurements in a TEM can be performed simultaneously.

This kind of holder requires specimens in special shape. As shown in Fig 7.6, the TEM grid was cut into half so that two probes could directly contact to the cut edge, where heterostructured nanotubes usually located. The half-cut specimen was fixed on one side of the holder, and two special probes served as two electrodes on the other side.

Fig 7.7 is our first plan for the measurement. We tried to grow SWCNTs on the edge of Mo grid, but Fe catalysts would lose activity on metal surface. As a result, Half-cut Mo grid was first deposited a layer of SiO_2 by sputtering process. After that, Fe catalysts were then deposited and SWCNTs could be grown at the edge of TEM grid as shown in Fig 7.7b. Fig 7.7a gives more details about the tunneling measurement. The TEM grid itself acted as gate electrode, and two probes acted as source and drain.

However, we could not get reasonable data because there was large resistance between the metal part and nanotube due to the SiO_2 layer.

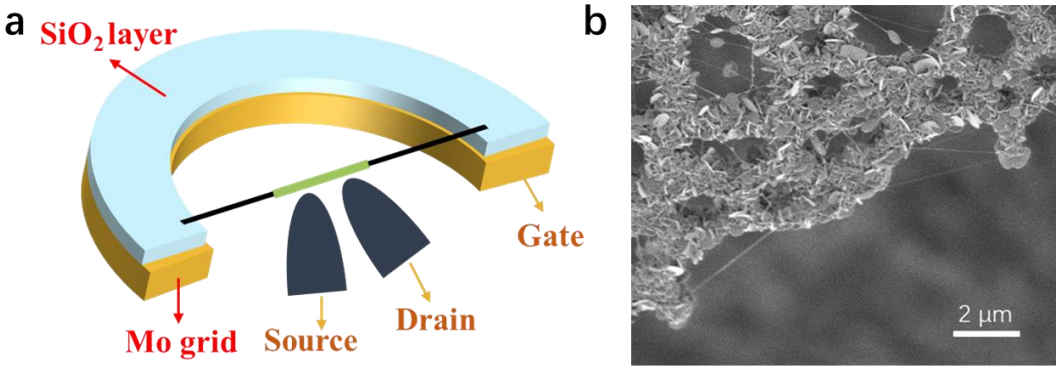

Figure 7.7 (a) Schematic illustration of in situ electronic characterization for SWCNT-BNNT sample on Mo-SiO_2 based TEM grid. (b) SEM image of SWCNT-BNNT hetero nanotube at TEM grid edge.

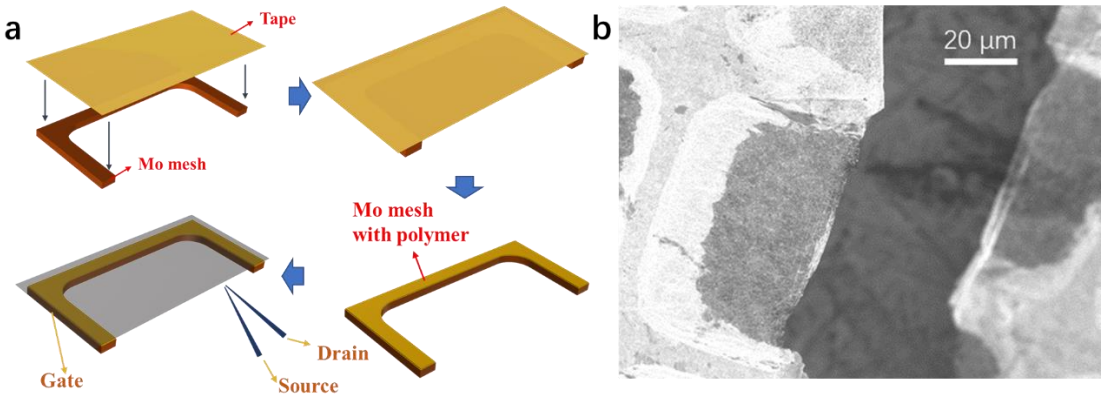

Figure 7.8 (a) Transfer process diagram of SWCNT-BNNT sample on Mo TEM grid and in situ electronic characterization. (b) SEM image of SWCNT-BNNT film at TEM grid edge.

Fig 7.8 is our second plan for the tunneling measurement. This time we used a pure Mo TEM grid to exclude the influence SiO_2 layer. Because catalysts would be no longer active on metal for SWCNTs synthesis, we decided to transfer a SWCNT (or BN coated) film onto the TEM grid, so that the nanotube sample can directly contact to the grid as gate electrode. Scotch tape was applied to increase adhesion between film and grid, as shown in Fig 7.8a. However, nanotubes aggregation could not be avoided at the

cut edge, so it is very difficult to find and manipulate individual nanotubes with two electrode probes. Also, thermal expansion of pure Mo metal was introduced during high-temperature CVD. Consequently, the film would be distorted along with the grid itself.

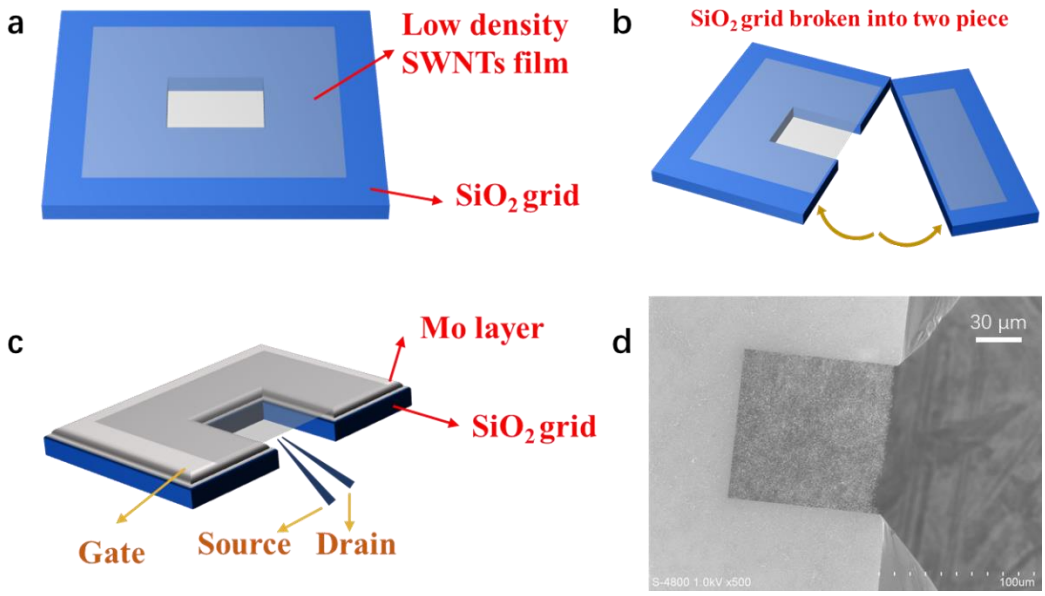

Figure 7.9 (a) Schematic illustration of Mo-deposited Si TEM grid with SWCNT-BNNT transferred on it. (b) Cracked TEM gird with nice film edge. (c) In situ electronic characterization based on cracked TEM grid. (d) SEM image of SWCNT-BNNT film at TEM grid edge.

Fig 7.9 is our final plan for the measurement. This time we used a pure Si TEM grid, which contributes only a small thermal expansion. To further increase conductivity, we deposited a layer of Mo on its surface, and film sample was transferred afterward (Fig 7.9a). After that, the most critical step is to break as-prepared TEM grid into two pieces (Fig 7.9b), so a nice film can be exposed to the edge for further probes manipulation (Fig 7.9c). SEM image of the nice film edge is shown in Fig 7.9d with no aggregation. This kind of TEM grid solved all the problems in previous two plans, but the drawback is, we could not precisely control the cracking direction due to square-shaped window on the Si grid. The success rate needs to be improved.

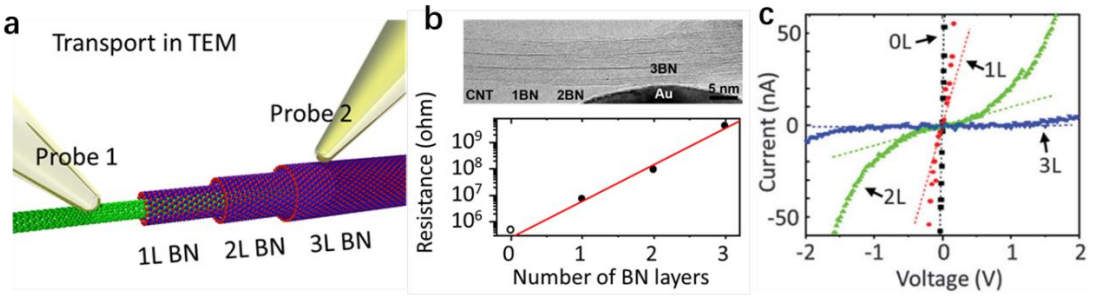

Figure 7.10 (a) Schematic illustration of the transport measurement at nano scale. (b) TEM image (upper) and resistance versus number of BN layers (lower). (c) Three typical I-V curves obtained in electronic measurement with different number of layers.

Based on the previous attempts, we finally got some reliable data for this in-situ TEM measurement. Fig 7.10a is the schematic illustration, where the current is measured through different number of layers by two probes as electrodes. One of the electrodes was fixed at bare SWCNT surface, another probe was moved gradually along the nanotube in different position with different number of BN layers. Fig 7.10b is the TEM image and the result plotted by resistance versus number of BN layers. As the number of BN layers increased, the resistance also increased exponentially. Fig 7.10c shows three typical I-V curves with 1 to 3 layers of BN. This characteristic has the same order to the 2D BN crystals [112, 113].

Chapter 8: Closing remarks

In this dissertation, we developed a true 1D vdW heterostructures by initially introduced CVD method for a controllable and high-quality synthesis. We then focused on their structure characterization, growth mechanism, and properties. Most importantly, it turned out that in practice this 1D atomic-scale Lego works exceptionally well, better than one could have imagined. How it works and why van der Waals heterostructures deserve attention is discussed in this dissertation.

In chapter 3, we first proposed a binary 1D vdW heterostructures, which can be considered as coaxial structure combined with single-crystalline SWCNT and BNNT. The thickness of BNNT is tunable by CVD duration. Patterned growth is also achievable. In chapter 4, we confirmed that MoS_2 can also be grown as the outer wall on the surface of pure SWCNT, and binary SWCNT-BNNT. Consequently, a ternary 1D vdW heterostructure is demonstrated in the form of SWCNT-BNNT-MoS_2, of which each layer is single-crystalline. The diameter of inner wall nanotube plays a key role in yield stability of MoS_2 nanotubes. In chapter 5 and 6, we discussed about the growth mechanism and analysed the structure relationship of interlayer. TEM results lent support to an open-end growth mechanism. Two key points were also confirmed for high quality 1D vdW heterostructures, including isolation effect, and cleanness effect. Then we further proposed a three growth models for outer BNNTs. As for the relationship of interlayer, no strict chiral angle dependence was found between inner and outer walls in 1D heterostructures, while handedness relationship between inner and outer walls in 1D heterostructures is not the case. There is a relatively higher tendency of the same handedness for the outer interlayers than the inner interlayers, probably because interfacial energy also becomes a leading factor when diameter becomes larger.

Chapter 7 showed the results of several preliminary experiments related to thermal, optical, electronic properties. We learned that the outer BNNTs served as protection layer for inner SWCNTs, resulting an enhanced thermal stability. Optical and electronic properties of inner SWCNTs was preserved in 1D heterostructures. Electron tunnelling effect through outer BN layers was of the same order to 2D BN crystals.

The possibility of making multilayer 1D vdW heterostructures has been demonstrated experimentally. As the variety of 2D crystals is continuously growing, and it looks like research for 1D heterostructures is only beginning. It would be instructive to review the existing library of 2D crystals, those individual components that can be used in the assembly for varied 1D heterostructures in the near future. Overall, the vast integration possibilities presented by 1D vdW heterostructures suggest considerable future growth potential for this field in both fundamental studies and applied technologies.

Bibliography

[1] J. Mao, Z. Liu, Z. Ren, "Size effect in thermoelectric materials." *npj Quantum Materials* **1**, 1 (2016).

[2] F. Giubileo, A. Di Bartolomeo, L. Iemmo, G. Luongo, F. Urban, "Field emission from carbon nanostructures." *Applied Sciences* **8**, 526 (2018).

[3] H. W. Kroto, J. R. Heath, S. C. O'Brien, R. F. Curl, R. E. Smalley, "C_{60}: Buckminsterfullerene." *Nature* **318**, 162 (1985).

[4] S. Iijima, "Helical microtubules of graphitic carbon." *Nature* **354**, 56 (1991).

[5] N. G. Chopra, R. Luyken, K. Cherrey, V. H. Crespi, M. L. Cohen, S. G. Louie, A. Zettl, "Boron nitride nanotubes." *Science* **269**, 966 (1995).

[6] M. Menon, D. Srivastava, "Structure of boron nitride nanotubes: Tube closing versus chirality." *Chemical Physics Letters* **307**, 407 (1999).

[7] X. Blase, A. Rubio, S. Louie, M. Cohen, "Stability and band gap constancy of boron nitride nanotubes." *EPL (Europhysics Letters)* **28**, 335 (1994).

[8] S. Berber, Y.-K. Kwon, D. Tománek, "Unusually high thermal conductivity of carbon nanotubes." *Physical review letters* **84**, 4613 (2000).

[9] C.-W. Chang, D. Okawa, H. Garcia, A. Majumdar, A. Zettl, "Breakdown of fourier's law in nanotube thermal conductors." *Physical review letters* **101**, 075903 (2008).

[10] Y. Xiao, X. Yan, J. Xiang, Y. Mao, Y. Zhang, J. Cao, J. Ding, "Specific heat of single-walled boron nitride nanotubes." *Applied Physics Letters* **84**, 4626 (2004).

[11] C. Chang, A. Fennimore, A. Afanasiev, D. Okawa, T. Ikuno, H. Garcia, D. Li, A. Majumdar, A. Zettl, "Isotope effect on the thermal conductivity of boron nitride nanotubes." *Physical review letters* **97**, 085901 (2006).

[12] Y. Chen, J. Zou, S. J. Campbell, G. Le Caer, "Boron nitride nanotubes: Pronounced resistance to oxidation." *Applied Physics Letters* **84**, 2430 (2004).

[13] D. Golberg, Y. Bando, K. Kurashima, T. Sato, "Synthesis and characterization of ropes made of bn multiwalled nanotubes." *Scripta Materialia* **44**, 1561 (2001).

[14] D. Yu, X. Sun, C. Lee, I. Bello, S. Lee, H. Gu, K. Leung, G. Zhou, Z. Dong, Z. Zhang, "Synthesis of boron nitride nanotubes by means of excimer laser ablation at high temperature." *Applied Physics Letters* **72**, 1966 (1998).

[15] G. W. Zhou, Z. Zhang, Z. G. Bai, "Catalyst effects on formation of boron nitride nano-tubules synthesized by laser ablation." *Solid State Communications* **109**, 555 (1999).

[16] E. Bengu, L. Marks, "Single-walled bn nanostructures." *Physical review letters* **86**, 2385 (2001).

[17] R. Lee, J. Gavillet, M. L. de La Chapelle, A. Loiseau, J.-L. Cochon, D. Pigache, J. Thibault, F. Willaime, "Catalyst-free synthesis of boron nitride single-wall nanotubes with a preferred zig-zag configuration." *Physical Review B* **64**, 121405 (2001).

[18] R. Arenal, O. Stephan, J.-L. Cochon, A. Loiseau, "Root-growth mechanism for single-walled boron nitride nanotubes in laser vaporization technique." *Journal of the American Chemical Society* **129**, 16183 (2007).

[19] T. Laude, Y. Matsui, A. Marraud, B. Jouffrey, "Long ropes of boron nitride nanotubes grown by a continuous laser heating." *Applied Physics Letters* **76**, 3239 (2000).

[20] J. Wang, V. K. Kayastha, Y. K. Yap, Z. Fan, J. G. Lu, Z. Pan, I. N. Ivanov, A. A. Puretzky, D. B. Geohegan, "Low temperature growth of boron nitride nanotubes on substrates." *Nano Lett* **5**, 2528 (2005).

[21] Y. Chen, L. T. Chadderton, J. F. Gerald, J. S. Williams, "A solid-state process for formation of boron nitride nanotubes." *Applied Physics Letters* **74**, 2960 (1999).

[22] Y. Chen, J. F. Gerald, J. Williams, S. Bulcock, "Synthesis of boron nitride nanotubes at low temperatures using reactive ball milling." *Chemical Physics Letters* **299**, 260 (1999).

[23] J. F. Gerald, Y. Chen, M. Conway, "Nanotube growth during annealing of mechanically milled boron." *Applied Physics A* **76**, 107 (2003).

[24] Y. Chen, M. Conway, J. Williams, J. Zou, "Large-quantity production of high-yield boron nitride nanotubes." *Journal of Materials Research* **17**, 1896 (2002).

[25] J. Yu, Y. Chen, R. G. Elliman, M. Petravic, "Isotopically enriched ^{10}bn nanotubes." *Advanced Materials* **18**, 2157 (2006).

[26] J. Yu, Y. Chen, R. Wuhrer, Z. Liu, S. P. Ringer, "In situ formation of bn nanotubes during nitriding reactions." *Chemistry of Materials* **17**, 5172 (2005).

[27] H. C. Choi, S. Y. Bae, W. S. Jang, J. Park, H. J. Song, H.-J. Shin, "X-ray absorption near edge structure study of bn nanotubes and nanothorns." *The Journal of Physical Chemistry B* **109**, 7007 (2005).

[28] R. Tenne, L. Margulis, M. e. Genut, G. Hodes, "Polyhedral and cylindrical structures of tungsten disulphide." *Nature* **360**, 444 (1992).

[29] L. Margulis, G. Salitra, R. Tenne, M. Talianker, "Nested fullerene-like structures." *Nature* **365**, 113 (1993).

[30] R. Tenne, M. Homyonfer, Y. Feldman, "Inorganic fullerene-like and nanotube materials: Synthesis, characterization and potential applications." *Chem. Mater* **10**, 3225 (1998).

[31] Y. Feldman, E. Wasserman, D. Srolovitz, R. Tenne, "High-rate, gas-phase growth of mos_2 nested inorganic fullerenes and nanotubes." *Science* **267**, 222 (1995).

[32] D. Mihailovic, Z. Jaglicic, D. Arcon, A. Mrzel, A. Zorko, M. Remskar, V. Kabanov, R. Dominko, M. Gaberscek, C. Gomez-Garcia, "Unusual magnetic state in lithium-doped mos_2 nanotubes." *Physical review letters* **90**, 146401 (2003).

[33] R. Dominko, D. Arčon, A. Mrzel, A. Zorko, P. Cevc, P. Venturini, M. Gaberscek, M. Remskar, D. Mihailovic, "Dichalcogenide nanotube electrodes for li - ion batteries." *Advanced Materials* **14**, 1531 (2002).

[34] K. S. Novoselov, A. K. Geim, S. V. Morozov, D. Jiang, Y. Zhang, S. V. Dubonos, I. V. Grigorieva, A. A. Firsov, "Electric field effect in atomically thin carbon films." *Science* **306**, 666 (2004).

[35] H. Y. Mao, S. Laurent, W. Chen, O. Akhavan, M. Imani, A. A. Ashkarran, M. Mahmoudi, "Graphene: Promises, facts, opportunities, and challenges in nanomedicine." *Chemical reviews* **113**, 3407 (2013).

[36] S. Morozov, K. Novoselov, M. Katsnelson, F. Schedin, D. Elias, J. A. Jaszczak, A. Geim, "Giant intrinsic carrier mobilities in graphene and its bilayer." *Physical review letters* **100**, 016602 (2008).

[37] R. R. Nair, P. Blake, A. N. Grigorenko, K. S. Novoselov, T. J. Booth, T. Stauber, N. M. Peres, A. K. Geim, "Fine structure constant defines visual transparency of graphene." *Science* **320**, 1308 (2008).

[38] H. Chen, M. B. Müller, K. J. Gilmore, G. G. Wallace, D. Li, "Mechanically strong, electrically conductive, and biocompatible graphene paper." *Advanced Materials* **20**, 3557 (2008).

[39] A. A. Balandin, S. Ghosh, W. Bao, I. Calizo, D. Teweldebrhan, F. Miao, C. N. Lau, "Superior thermal conductivity of single-layer graphene." *Nano Lett* **8**, 902 (2008).

[40] J. C. Meyer, A. K. Geim, M. I. Katsnelson, K. S. Novoselov, T. J. Booth, S. Roth, "The structure of suspended graphene sheets." *Nature* **446**, 60 (2007).

[41] X. Li, X. Wang, L. Zhang, S. Lee, H. Dai, "Chemically derived, ultrasmooth graphene nanoribbon semiconductors." *Science* **319**, 1229 (2008).

[42] Q. Xi, X. Chen, D. G. Evans, W. Yang, "Gold nanoparticle-embedded porous graphene thin films fabricated via layer-by-layer self-assembly and subsequent thermal annealing for electrochemical sensing." *Langmuir* **28**, 9885 (2012).

[43] W. Lv, Z. Li, Y. Deng, Q.-H. Yang, F. Kang, "Graphene-based materials for electrochemical energy storage devices: Opportunities and challenges." *Energy Storage Materials* **2**, 107 (2016).

[44] U. Khan, T. H. Kim, H. Ryu, W. Seung, S. W. Kim, "Graphene tribotronics for electronic skin and touch screen applications." *Advanced Materials* **29**, 1603544 (2017).

[45] F. Schwierz, "Graphene transistors." *Nature nanotechnology* **5**, 487 (2010).

[46] E. Singh, M. Meyyappan, H. S. Nalwa, "Flexible graphene-based wearable gas and chemical sensors." *ACS applied materials & interfaces* **9**, 34544 (2017).

[47] R. Ruoff, "Graphene: Calling all chemists." *Nature nanotechnology* **3**, 10 (2008).

[48] S. Stankovich, D. A. Dikin, R. D. Piner, K. A. Kohlhaas, A. Kleinhammes, Y. Jia, Y. Wu, S. T. Nguyen, R. S. Ruoff, "Synthesis of graphene-based nanosheets via chemical reduction of exfoliated graphite oxide." *Carbon* **45**, 1558 (2007).

[49] X. Yang, X. Dou, A. Rouhanipour, L. Zhi, H. J. Räder, K. Müllen, "Two-dimensional graphene nanoribbons." *Journal of the American Chemical Society* **130**, 4216 (2008).

[50] C. Berger, Z. Song, T. Li, X. Li, A. Y. Ogbazghi, R. Feng, Z. Dai, A. N. Marchenkov, E. H. Conrad, P. N. First, "Ultrathin epitaxial graphite: 2d electron gas properties and a route toward graphene-based nanoelectronics." *The Journal of Physical Chemistry B* **108**, 19912 (2004).

[51] M. Gao, M. Adachi, A. Lyalin, T. Taketsugu, "Long range functionalization of h-bn monolayer by carbon doping." *The Journal of Physical Chemistry C* **120**, 15993 (2016).

[52] D. Pacile, J. Meyer, Ç. Girit, A. Zettl, "The two-dimensional phase of boron nitride: Few-atomic-layer sheets and suspended membranes." *Applied Physics Letters* **92**, 133107 (2008).

[53] C. Zhi, Y. Bando, C. Tang, H. Kuwahara, D. Golberg, "Large‐scale fabrication of boron nitride nanosheets and their utilization in polymeric composites with improved thermal and mechanical properties." *Advanced Materials* **21**, 2889 (2009).

[54] J.-H. Park, S. H. Choi, J. Zhao, S. Song, W. Yang, S. M. Kim, K. K. Kim, Y. H. Lee, "Thickness-controlled multilayer hexagonal boron nitride film prepared by plasma-enhanced chemical vapor deposition." *Current Applied Physics* **16**, 1229 (2016).

[55] A.-R. Jang, S. Hong, C. Hyun, S. I. Yoon, G. Kim, H. Y. Jeong, T. J. Shin, S. O. Park, K. Wong, S. K. Kwak, "Wafer-scale and wrinkle-free epitaxial growth of single-orientated multilayer hexagonal boron nitride on sapphire." *Nano Lett* **16**, 3360 (2016).

[56] C. R. Dean, A. F. Young, I. Meric, C. Lee, L. Wang, S. Sorgenfrei, K. Watanabe, T. Taniguchi, P. Kim, K. L. Shepard, "Boron nitride substrates for high-quality graphene electronics." *Nature nanotechnology* **5**, 722 (2010).

[57] H. Wang, T. Taychatanapat, A. Hsu, K. Watanabe, T. Taniguchi, P. Jarillo-Herrero, T. Palacios, "Bn/graphene/bn transistors for rf applications." *IEEE Electron Device Letters* **32**, 1209 (2011).

[58] A. S. Mayorov, R. V. Gorbachev, S. V. Morozov, L. Britnell, R. Jalil, L. A. Ponomarenko, P. Blake, K. S. Novoselov, K. Watanabe, T. Taniguchi,

"Micrometer-scale ballistic transport in encapsulated graphene at room temperature." *Nano Lett* **11**, 2396 (2011).

[59] G.-H. Lee, X. Cui, Y. D. Kim, G. Arefe, X. Zhang, C.-H. Lee, F. Ye, K. Watanabe, T. Taniguchi, P. Kim, "Highly stable, dual-gated mos_2 transistors encapsulated by hexagonal boron nitride with gate-controllable contact, resistance, and threshold voltage." *ACS nano* **9**, 7019 (2015).

[60] J. I.-J. Wang, Y. Yang, Y.-A. Chen, K. Watanabe, T. Taniguchi, H. O. Churchill, P. Jarillo-Herrero, "Electronic transport of encapsulated graphene and wse_2 devices fabricated by pick-up of prepatterned hbn." *Nano Lett* **15**, 1898 (2015).

[61] J. Golden, M. McMillan, R. T. Downs, G. Hystad, I. Goldstein, H. J. Stein, A. Zimmerman, D. A. Sverjensky, J. T. Armstrong, R. M. Hazen, "Rhenium variations in molybdenite (mos_2): Evidence for progressive subsurface oxidation." *Earth and Planetary Science Letters* **366**, 1 (2013).

[62] A. Laturia, M. L. Van de Put, W. G. Vandenberghe, "Dielectric properties of hexagonal boron nitride and transition metal dichalcogenides: From monolayer to bulk." *npj 2D Materials and Applications* **2**, 1 (2018).

[63] Q. H. Wang, K. Kalantar-Zadeh, A. Kis, J. N. Coleman, M. S. Strano, "Electronics and optoelectronics of two-dimensional transition metal dichalcogenides." *Nature nanotechnology* **7**, 699 (2012).

[64] K. F. Mak, C. Lee, J. Hone, J. Shan, T. F. Heinz, "Atomically thin mos_2: A new direct-gap semiconductor." *Physical review letters* **105**, 136805 (2010).

[65] M. Dragoman, D. Dragoman, *2d nanoelectronics: Physics and devices of atomically thin materials*. (Springer, 2016).

[66] B. Radisavljevic, A. Radenovic, J. Brivio, V. Giacometti, A. Kis, "Single-layer mos_2 transistors." *Nature nanotechnology* **6**, 147 (2011).

[67] A. Splendiani, L. Sun, Y. Zhang, T. Li, J. Kim, C.-Y. Chim, G. Galli, F. Wang, "Emerging photoluminescence in monolayer mos_2." *Nano Lett* **10**, 1271 (2010).

[68] A. Koma, K. Sunouchi, T. Miyajima, "Fabrication and characterization of heterostructures with subnanometer thickness." *Microelectronic Engineering* **2**, 129 (1984).

[69] A. Koma, "Van der waals epitaxy—a new epitaxial growth method for a highly lattice-mismatched system." *Thin Solid Films* **216**, 72 (1992).

[70] L. Britnell, R. Gorbachev, R. Jalil, B. Belle, F. Schedin, A. Mishchenko, T. Georgiou, M. Katsnelson, L. Eaves, S. Morozov, "Field-effect tunneling transistor based on vertical graphene heterostructures." *Science* **335**, 947 (2012).

[71] L. Britnell, R. Ribeiro, A. Eckmann, R. Jalil, B. Belle, A. Mishchenko, Y.-J. Kim, R. Gorbachev, T. Georgiou, S. Morozov, "Strong light-matter interactions in heterostructures of atomically thin films." *Science* **340**, 1311 (2013).

[72] T. Georgiou, R. Jalil, B. D. Belle, L. Britnell, R. V. Gorbachev, S. V. Morozov, Y.-J. Kim, A. Gholinia, S. J. Haigh, O. Makarovsky, "Vertical field-effect transistor based on graphene–ws_2 heterostructures for flexible and transparent electronics." *Nature nanotechnology* **8**, 100 (2013).

[73] W. Yang, G. Chen, Z. Shi, C.-C. Liu, L. Zhang, G. Xie, M. Cheng, D. Wang, R. Yang, D. Shi, "Epitaxial growth of single-domain graphene on hexagonal boron nitride." *Nature materials* **12**, 792 (2013).

[74] H. Fang, C. Battaglia, C. Carraro, S. Nemsak, B. Ozdol, J. S. Kang, H. A. Bechtel, S. B. Desai, F. Kronast, A. A. Unal, "Strong interlayer coupling in van der waals heterostructures built from single-layer chalcogenides." *Proceedings of the National Academy of Sciences* **111**, 6198 (2014).

[75] P. Rivera, J. R. Schaibley, A. M. Jones, J. S. Ross, S. Wu, G. Aivazian, P. Klement, K. Seyler, G. Clark, N. J. Ghimire, "Observation of long-lived interlayer excitons in monolayer $mose_2$–wse_2 heterostructures." *Nature communications* **6**, 1 (2015).

[76] F. Withers, O. Del Pozo-Zamudio, A. Mishchenko, A. Rooney, A. Gholinia, K. Watanabe, T. Taniguchi, S. Haigh, A. Geim, A. Tartakovskii, "Light-emitting diodes by band-structure engineering in van der waals heterostructures." *Nature materials* **14**, 301 (2015).

[77] F. Withers, O. Del Pozo-Zamudio, S. Schwarz, S. Dufferwiel, P. Walker, T. Godde, A. Rooney, A. Gholinia, C. Woods, P. Blake, "Wse_2 light-emitting tunneling transistors with enhanced brightness at room temperature." *Nano Lett* **15**, 8223 (2015).

[78] G. Konstantatos, M. Badioli, L. Gaudreau, J. Osmond, M. Bernechea, F. P. G. De Arquer, F. Gatti, F. H. Koppens, "Hybrid graphene–quantum dot phototransistors with ultrahigh gain." *Nature nanotechnology* **7**, 363 (2012).

[79] D. Jariwala, V. K. Sangwan, C.-C. Wu, P. L. Prabhumirashi, M. L. Geier, T. J. Marks, L. J. Lauhon, M. C. Hersam, "Gate-tunable carbon nanotube–mos_2 heterojunction pn diode." *Proceedings of the National Academy of Sciences* **110**, 18076 (2013).

[80] D. Ruzmetov, K. Zhang, G. Stan, B. Kalanyan, G. R. Bhimanapati, S. M. Eichfeld, R. A. Burke, P. B. Shah, T. P. O'Regan, F. J. Crowne, "Vertical 2d/3d semiconductor heterostructures based on epitaxial molybdenum disulfide and gallium nitride." *ACS nano* **10**, 3580 (2016).

[81] D. Jariwala, T. J. Marks, M. C. Hersam, "Mixed-dimensional van der waals heterostructures." *Nature materials* **16**, 170 (2017).

[82] L. Chen, H. Ye, Y. Gogotsi, "Synthesis of boron nitride coating on carbon nanotubes." *Journal of the American Ceramic Society* **87**, 147 (2004).

[83] W. Hsu, Y. Zhu, H. Kroto, D. Walton, R. Kamalakaran, M. Terrones, "C-mos_2 and c-ws_2 nanocomposites." *Applied Physics Letters* **77**, 4130 (2000).

[84] K. Suenaga, C. Colliex, N. Demoncy, A. Loiseau, H. Pascard, F. Willaime, "Synthesis of nanoparticles and nanotubes with well-separated layers of boron nitride and carbon." *Science* **278**, 653 (1997).

[85] R. Nakanishi, R. Kitaura, J. H. Warner, Y. Yamamoto, S. Arai, Y. Miyata, H. Shinohara, "Thin single-wall bn-nanotubes formed inside carbon nanotubes." *Sci Rep* **3**, 1385 (2013).

[86] R. Arenal, A. Lopez-Bezanilla, "In situ formation of carbon nanotubes encapsulated within boron nitride nanotubes via electron irradiation." *ACS nano* **8**, 8419 (2014).

[87] A. Sengupta, "Atomistic study of electrostatics and carrier transport properties of cnt@ ms_2 (m= mo, w) and cnt@ bn core–shell nanotubes." *Journal of Materials Science* **52**, 8119 (2017).

[88] C. Hu, V. Michaud-Rioux, W. Yao, H. Guo, "Theoretical design of topological heteronanotubes." *Nano Lett* **19**, 4146 (2019).

[89] Z. Liu, L. Song, S. Zhao, J. Huang, L. Ma, J. Zhang, J. Lou, P. M. Ajayan, "Direct growth of graphene/hexagonal boron nitride stacked layers." *Nano Lett* **11**, 2032 (2011).

[90] T. Uwanno, T. Taniguchi, K. Watanabe, K. Nagashio, "Electrically inert h-bn/bilayer graphene interface in all-two-dimensional heterostructure field effect transistors." *ACS applied materials & interfaces* **10**, 28780 (2018).

[91] Y. Shi, W. Zhou, A.-Y. Lu, W. Fang, Y.-H. Lee, A. L. Hsu, S. M. Kim, K. K. Kim, H. Y. Yang, L.-J. Li, "Van der waals epitaxy of mos_2 layers using graphene as growth templates." *Nano Lett* **12**, 2784 (2012).

[92] Y.-C. Lin, N. Lu, N. Perea-Lopez, J. Li, Z. Lin, X. Peng, C. H. Lee, C. Sun, L. Calderin, P. N. Browning, "Direct synthesis of van der waals solids." *ACS nano* **8**, 3715 (2014).

[93] X. Li, L. Basile, B. Huang, C. Ma, J. Lee, I. V. Vlassiouk, A. A. Puretzky, M.-W. Lin, M. Yoon, M. Chi, "Van der waals epitaxial growth of two-dimensional single-crystalline gase domains on graphene." *ACS nano* **9**, 8078 (2015).

[94] A. Yan, J. Velasco Jr, S. Kahn, K. Watanabe, T. Taniguchi, F. Wang, M. F. Crommie, A. Zettl, "Direct growth of single-and few-layer mos_2 on h-bn with preferred relative rotation angles." *Nano Lett* **15**, 6324 (2015).

[95] S. Wang, X. Wang, J. H. Warner, "All chemical vapor deposition growth of mos_2: H-bn vertical van der waals heterostructures." *ACS nano* **9**, 5246 (2015).

[96] Y.-C. Lin, R. K. Ghosh, R. Addou, N. Lu, S. M. Eichfeld, H. Zhu, M.-Y. Li, X. Peng, M. J. Kim, L.-J. Li, "Atomically thin resonant tunnel diodes built from synthetic van der waals heterostructures." *Nature communications* **6**, 1 (2015).

[97] P. T. Araujo, S. K. Doorn, S. Kilina, S. Tretiak, E. Einarsson, S. Maruyama, H. Chacham, M. A. Pimenta, A. Jorio, "Third and fourth optical transitions in semiconducting carbon nanotubes." *Physical review letters* **98**, 067401 (2007).

[98] H. Kataura, Y. Kumazawa, Y. Maniwa, I. Umezu, S. Suzuki, Y. Ohtsuka, Y. Achiba, "Optical properties of single-wall carbon nanotubes." *Synthetic metals* **103**, 2555 (1999).

[99] A. Kaskela, A. G. Nasibulin, M. Y. Timmermans, B. Aitchison, A. Papadimitratos, Y. Tian, Z. Zhu, H. Jiang, D. P. Brown, A. Zakhidov, E. I. Kauppinen, "Aerosol-synthesized swcnt networks with tunable conductivity and transparency by a dry transfer technique." *Nano Lett* **10**, 4349 (2010).

[100] A. Rubio, J. L. Corkill, M. L. Cohen, "Theory of graphitic boron nitride nanotubes." *Physical Review B* **49**, 5081 (1994).

[101] R. Arenal, X. Blase, A. Loiseau, "Boron-nitride and boron-carbonitride nanotubes: Synthesis, characterization and theory." *Advances in Physics* **59**, 101 (2010).

[102] K. Hisama, S. Chiashi, S. Maruyama, S. Okada, "Energetics and electronic structures of single walled carbon nanotubes encapsulated in boron nitride nanotubes." *Applied Physics Express* **13**, 015004 (2019).

[103] A. Klots, A. Newaz, B. Wang, D. Prasai, H. Krzyzanowska, J. Lin, D. Caudel, N. Ghimire, J. Yan, B. Ivanov, "Probing excitonic states in suspended two-dimensional semiconductors by photocurrent spectroscopy." *Sci Rep* **4**, 6608 (2014).

[104] L. Reimer, *Scanning electron microscopy: Physics of image formation and microanalysis*. (Springer, 2013), vol. 45.

[105] J.-M. Zuo, M. Gao, J. Tao, B. Q. Li, R. Twesten, I. Petrov, "Coherent nano‐area electron diffraction." *Microscopy research and technique* **64**, 347 (2004).

[106] R. Xiang, T. Inoue, Y. Zheng, A. Kumamoto, Y. Qian, Y. Sato, M. Liu, D. Tang, D. Gokhale, J. Guo, K. Hisama, S. Yotsumoto, T. Ogamoto, H. Arai, Y. Kobayashi, H. Zhang, B. Hou, A. Anisimov, M. Maruyama, Y. Miyata, S. Okada, S. Chiashi, Y. Li, J. Kong, E. I. Kauppinen, Y. Ikuhara, K. Suenaga, S. Maruyama, "One-dimensional van der waals heterostructures." *Science* **367**, 537 (2020).

[107] Z. Liu, K. Suenaga, H. Yoshida, T. Sugai, H. Shinohara, S. Iijima, "Determination of optical isomers for left-handed or right-handed chiral double-wall carbon nanotubes." *Physical review letters* **95**, 187406 (2005).

[108] P. Yuan, Z. Zhang, S. Yokokawa, Y. Zheng, L. Jin, S. Y. Set, S. Maruyama, S. Yamashita, in *2019 Conference on Lasers and Electro-Optics (CLEO)*. (IEEE, 2019), pp. 1.

[109] S. Y. Set, H. Yaguchi, Y. Tanaka, M. Jablonski, "Laser mode locking using a saturable absorber incorporating carbon nanotubes." *Journal of lightwave Technology* **22**, 51 (2004).

[110] P. Wang, Y. Zheng, T. Inoue, R. Xiang, A. Shawky, M. Watanabe, A. Anisimov, E. I. Kauppinen, S. Chiashi, S. Maruyama, "Enhanced in-plane thermal conductance of thin films composed of coaxially combined single-walled carbon nanotubes and boron nitride nanotubes." *ACS nano* **14**, 4298 (2020). doi:10.1021/acsnano.9b09754

[111] S. Maruyama, R. Kojima, Y. Miyauchi, S. Chiashi, M. Kohno, "Low-temperature synthesis of high-purity single-walled carbon nanotubes from alcohol." *Chemical Physics Letters* **360**, 229 (2002).

[112] G.-H. Lee, Y.-J. Yu, C. Lee, C. Dean, K. L. Shepard, P. Kim, J. Hone, "Electron tunneling through atomically flat and ultrathin hexagonal boron nitride." *Applied Physics Letters* **99**, 243114 (2011).

[113] L. Britnell, R. V. Gorbachev, R. Jalil, B. D. Belle, F. Schedin, M. I. Katsnelson, L. Eaves, S. V. Morozov, A. S. Mayorov, N. M. Peres, "Electron tunneling through ultrathin boron nitride crystalline barriers." *Nano Lett* **12**, 1707 (2012).

Appendices

Transfer method for suspended film

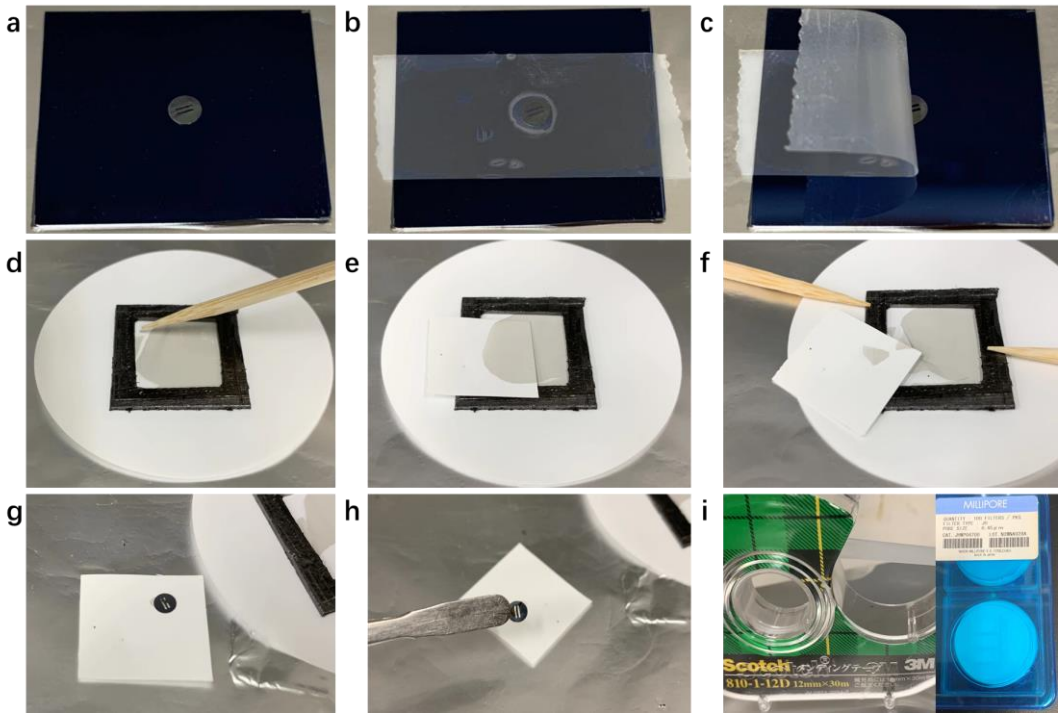

Figure 8 A practical transfer method for suspended film from a washer to a TEM grid.

In some circumstances, we need to transfer the macro sample on washer back to TEM grids for micro micro-and nanoscale characterization. It is known that the SWCNT film easily rolls up, but it is hard to recover to the original state as the contacting surfaces adhere to each other due to its high surface energy [110]. After coated with BNNTs, the SWCNTs film can retains its flexibility and can easily recover to the original morphology immediately when released. However, the reduced surface adhesion makes SWCNT-BNNT difficult to transfer onto another TEM grid. Here, we proposed a practical transfer method for this situation, of which the main idea is to use scotch tape to increase the adhesion between SWCNT-BNNT film and TEM grid. In step one, we put scotch tape on the TEM grid and tear it down so that some polymer materials with high adhesion will remain on the TEM grid (Fig. 8a-c). Then, we place the sample on a filter paper, then break the SWCNT-BNNT film by a toothpick or

some needle-like tools (Fig, 8d-f). Metal tweezer is not recommended because the film tends to stick to metal tweezer. After that, we tear off a small piece of film and try to let it stay on another filter paper. It is also necessary to avoid any airflow during this process, such as wearing a mask to keep away your breath of air. Finally, TEM grid was put upside down onto the film, and the film will stick on the TEM grid with the help of remaining polymer materials on grid surface (Fig 8g and h). Fig. i is the scotch tape and filter paper we used in this transfer method.

Publication List

- Xiang, R. †, Inoue, T. †, **Zheng, Y.** †, Kumamoto, A., Qian, Y., Sato, Y., Liu, M., Tang, D., Gokhale, D., Guo, J., Hisama, K., Yotsumoto, S., Ogamoto, T., Arai, H., Kobayashi, Y., Zhang, H., Hou, B., Anisimov, A., Maruyama, M., Miyata, Y., Okada, S., Chiashi, S., Li, Y., Kong, J., Kauppinen, E., Ikuhara, Y., Suenaga, K., Maruyama, S., (2020). One-dimensional van der Waals heterostructures. *Science*, *367*(6477), 537-542.
- Wang, P., **Zheng, Y.**, Inoue, T., Xiang, R., Shawky, A., Watanabe, M., Anisimov, A., Kauppinen, E., Maruyama, S., (2020). Enhanced In-Plane Thermal Conductance of Thin Films Composed of Coaxially Combined Single-Walled Carbon Nanotubes and Boron Nitride Nanotubes. *ACS nano*., 14(4), 4298.
- Burdanova, M., Kashtiban, R.; **Zheng, Y.**, Xiang, R., Chiashi, S., Woolley, J., Staniforth, M., Sakamoto-Rablah, E., Xia, X., Broome, M., Sloan, J., Anisimov, A., Kauppinen, E., Maruyama, S., Lloyd-Hughes, J., (2020). Ultrafast optoelectronic processes in 1D radial van der Waals heterostructures: carbon, boron nitride and MoS_2 nanotubes with coexisting excitons and highly mobile charges. *Nano Lett.*, 20(5), 3560-3567.
- Qian, Y., Seo, S., Jeon, I., Lin, H., Okawa, S., **Zheng, Y**., Shawky, A., Anisimov, A., Kauppinen, E., Kong, J., Xiang, R., Matsuo, Y., Maruyama, S., (2020). MoS_2-carbon nanotube heterostructure as efficient hole transporters and conductors in perovskite solar cells. *Appl. Phys. Lett.*, submitted.
- Yuan, P., Zhang, Z., Yokokawa, S., **Zheng, Y.**, Jin, L., Set, S. Y., Maruyama, S., Yamashita, S. (2019, May). High Power Tolerant SWCNT-BNNT Saturable Absorber for Laser Mode-Locking. In *2019 Conference on Lasers and Electro-Optics (CLEO)* (pp. 1-2). IEEE.
- **Zheng, Y.**, et al. Growth mechanism and structure correlation in 1D van der Waals heterostructures, in preparation.
- **Zheng, Y**., Lin, Z., Chen, W., Liang, B., Du, H., Yang, R., He, X., Tang, Z., Gui, X., (2017). Flexible, sandwich-like CNTs/$NiCo_2O_4$ hybrid paper

electrodes for all-solid-state supercapacitors. *Journal of Materials Chemistry A*, *5*(12), 5886-5894.

- Cheng, X., Gui, X., Lin, Z., **Zheng, Y**., Liu, M., Zhan, R., Zhu, Y., Tang, Z., (2015). Three-dimensional α-Fe_2O_3/carbon nanotube sponges as flexible supercapacitor electrodes. *Journal of Materials Chemistry A*, *3*(42), 20927-20934.
- Shen, F., Zhang, F., **Zheng, Y**., Fan, Z., Li, Z., Sun, Z., Xuan, Y., Zhao, B., Lin, Z., Gui, X., Han, X., Cheng, Y., Niu, C., (2018). Direct growth of 3D host on Cu foil for stable lithium metal anode. *Energy Storage Materials*, 13, 323-328.
- Chen, W., Gui, X., Liang, B., Yang, R., **Zheng, Y**., Zhao, C., Li, X., Zhu, H., Tang, Z., (2017). Structural engineering for high sensitivity, ultrathin pressure sensors based on wrinkled graphene and anodic aluminum oxide membrane. *ACS applied materials & interfaces*, *9*(28), 24111-24117.
- Zhong, J., Zhang, X., **Zheng, Y**., Zheng, M., Wen, M., Wu, S., Gao, J., Gao, X., Liu, J., Zhao, H., (2013). High efficiency solar cells as fabricated by Sb_2S_3-modified TiO_2 nanofibrous networks. *ACS applied materials & interfaces*, *5*(17), 8345-8350.
- Chen, W., Gui, X., **Zheng, Y**., Liang, B., Lin, Z., Zhao, C., Chen, H., Chen, Z., Li, X., Tang, Z. (2017). Synergistic Effects of Wrinkled Graphene and Plasmonics in Stretchable Hybrid Platform for Surface-Enhanced Raman Spectroscopy. *Advanced Optical Materials*, *5*(6), 1600715.
- Du, H., Gui, X., Yang, R., Lin, Z., Liang, B., Chen, W., **Zheng, Y**., Zhu, H., Chen, J. (2018). In situ sulfur loading in graphene-like nano-cell by template-free method for Li–S batteries. *Nanoscale*, *10*(8), 3877-3883.

Conference Contributions

- FNTG 54-56, Tokyo, Sendai (The 54th - 56th Fullerenes-Nanotubes-Graphene General Symposium), **Poster**.
- ChinaNANO 2019, Beijing (The 8th International Conference on Nanoscience and Technology 2019), **Poster**.
- LDMO 2019, Shenzhen (Low Dimensional Materials for Optoelectronics 2019), **Oral.**
- ICONN 2019, Brisbane, Australia (The 8th International Conference on Nanoscience and Nanotechnology 2020), **Oral**.

Acknowledgments

Foremost, I would like to express my sincere gratitude to my supervisor Prof. Maruyama for the continuous support of my doctoral study and motivation for research study. Besides, I would like to thank Prof. Xiang Rong, who have helped me in all the time of research and writing of this this dissertation. Especially in the new area “one-dimensional heterostructures”, he has been leading me working on diverse exciting topics all the way and taught me many things. Also, I need to thank Prof. Inoue and Prof. Chiashi for their guidance and suggestion with my experiments.

My special gratitude goes to P. Wang and H. Lin as my colleagues in the same year. We always share ideas and stories with our research study, and back up each other.

I also thank my fellow lab members Y. Qian, M. Liu, Y. Feng, T. Ogamoto, S. Yotsumoto, K. Hisama, B. Koyano, H. Arai, K. Otsuka, H. Zhang, S. Yamamoto, and D. Gokhale for the experimental discussions and collaboration.

Overall, I need to thank all my friends in Japan. This is my first time living abroad far away from family, but I am not alone with all the happiness and memories we made in these three years.

Last but not the least, I would like to thank my family for supporting me spiritually throughout my doctoral program and motivating me to pursue further study in a foreign country.